

# COULOMB EXCITATION OF NEUTRON-DEFICIENT $^{140}\text{Sm}$

by

Trond Wiggo Johansen

THESIS  
for the degree of  
MASTER OF SCIENCE



Faculty of Mathematics and Natural Sciences  
University of Oslo

September 2019



# Abstract

In the present work, data from a Coulomb excitation experiment of  $^{140}\text{Sm}$  was analyzed. The experiment was carried out at the ISOLDE facility at CERN in 2017 to investigate the nuclear structure of  $^{140}\text{Sm}$ . This isotope is of great importance to explain nuclear shape transitions, as it lies in between a spherical and deformed shape.

In the experiment, a radioactive ion beam of  $^{140}\text{Sm}$  was accelerated into a  $^{208}\text{Pb}$  target. Silicon detectors were utilized to determine the energies and angles of the scattered particles, and germanium detectors to measure the  $\gamma$ -rays of excited states in  $^{140}\text{Sm}$ . MiniballCoulexSort, a code which is under development at ISOLDE, was applied to sort the data. A fully calibrated data set was obtained, in addition to Doppler corrected  $\gamma$  spectra for  $^{140}\text{Sm}$  with good resolution.

As expected, a number of previously known  $\gamma$  transitions were observed. Excited states up to and including the  $8^+$  state at 2970 keV were populated in  $^{140}\text{Sm}$ . Two peaks in the  $\gamma$ -ray spectrum do not correspond to any of the known transitions in the level scheme. One peak is observed at approximately 844 keV, and the other at approximately 1860 keV. The results suggests that these peaks are previously unknown transitions.

In particular, the peak at 844 keV may be a member of the  $\gamma$ -vibrational band, which is theoretically predicted to be built on the observed  $2_2^+$  state at 990 keV. The intensity of the new 844 keV transition is relatively strong and it is observed to arrive in coincidence with the 990 keV ( $2_2^+$ ) state, making it a good candidate for the theoretically predicted  $3_1^+$  state. Further analysis is needed to determine if the 844 keV transition identifies as the  $3_1^+$  state. If verified, the new  $3_1^+$  state will certainly clarify the role of triaxial deformation of  $^{140}\text{Sm}$ .



To my family, for all their love, support and encouragement!



# Acknowledgements

I would like to thank my supervisors Professor Andreas Görzen and Dr. Katarzyna Hadyńska-Klek for giving me the amazing opportunity to do an experiment at CERN-ISOLDE. It has been a great experience. A special thanks to Andreas for being available for weekly meetings to answer all my questions about the experiment and the physics behind it. Thanks for the good advises, help and enriching ideas you provided.

In addition, I would like to thank the participants of the experiment, listed in [Table G.1](#), I hope everyone are included (if not, please let me know!). Also, thank you to the CERN-ISOLDE staff who made this experiment possible. A special thanks to Dr. Liam Gaffney for answering all my e-mails regarding the MiniballCoulexSort. Thank you Ville Virtanen for helping me getting started on the scripts for my thesis.

I would like to thank the Computational Physics Group for giving me a great working environment, and Professor Morten Hjorth-Jensen for introducing me to the fantastic C++ programming language.

I am grateful to the Nuclear Physics Group, for gathering students and employees together at meetings and conferences around the world. Thank you for letting me go to the summer school in South Africa and to the physics conference in Svalbard. Thanks to this, I have many adventures to look back to.

Thank you Lillefy, Fysisk Fagutvalg and Fysikkforeningen for making my physics bachelor a great experience.

A big thanks to my family for all the help, financial and moral support. I would not have been able to do this without you.

I would like to thank my close friends Morten, Alexander and Astrid for enriching my life outside physics and keeping me sane.

Finally, Ina my sweetheart, thank you for pushing me towards excellence. I love you.

*Trond Wiggo Johansen*

September, 2019



# Contents

<b>1</b>	<b>Introduction</b>	<b>11</b>
<b>2</b>	<b>Theory</b>	<b>17</b>
2.1	Nuclear deformation . . . . .	17
2.2	Coulomb excitation method . . . . .	21
2.2.1	Safe COULEX . . . . .	24
2.2.2	Cross sections . . . . .	25
2.2.3	Transition probabilities . . . . .	27
2.2.4	Electric quadrupole moments . . . . .	29
<b>3</b>	<b>Coulomb excitation experiment</b>	<b>33</b>
3.1	ISOLDE at CERN . . . . .	33
3.2	Experimental setup . . . . .	35
3.2.1	Beam production . . . . .	35
3.2.2	Sources of beam contaminants . . . . .	38
3.2.3	The secondary target . . . . .	38
3.2.4	Miniball spectrometer . . . . .	39
3.3	Data acquisition system . . . . .	43
3.4	Time structure . . . . .	45
<b>4</b>	<b>Data analysis</b>	<b>49</b>
4.1	Data handling . . . . .	49
4.1.1	Counting and naming convention for particle detector calibration . . . . .	51
4.2	Data conversion . . . . .	51
4.3	Detector calibration . . . . .	53
4.3.1	Kinematic simulation . . . . .	54
4.3.2	Online calibration of the particle detector . . . . .	56
4.3.3	User calibration of the particle detector . . . . .	57
4.3.4	The double peak structure . . . . .	62
4.3.5	CD threshold . . . . .	64
4.3.6	Time calibration . . . . .	65
4.3.7	Calibration of the $\gamma$ detectors . . . . .	66
4.3.8	$\gamma$ sorting . . . . .	68
4.3.9	Doppler correction . . . . .	71
4.3.10	Broken detector segments . . . . .	72
<b>5</b>	<b>Experimental results and discussion</b>	<b>75</b>
<b>6</b>	<b>Summary and outlook</b>	<b>85</b>

<b>Appendices</b>	<b>87</b>
<b>Appendix A Acronyms and abbreviations</b>	<b>89</b>
<b>Appendix B Computer setup and environment</b>	<b>91</b>
<b>Appendix C MiniballCoulexSort and ROOT</b>	<b>95</b>
C.1 Connecting MiniballCoulexSort with ROOT . . . . .	95
C.2 Running ROOT and MiniballCoulexSort from anywhere in the terminal . . . . .	96
C.3 CLXAna . . . . .	96
C.3.1 Input parameters . . . . .	96
C.3.2 Graphical cuts . . . . .	98
<b>Appendix D Two-particle elastic collision</b>	<b>99</b>
D.1 Laboratory (LAB) frame of reference . . . . .	99
D.2 Center of mass (CM) frame of reference . . . . .	102
D.3 Connection between the LAB frame and the CM frame . . . . .	104
<b>Appendix E Signal cable wiring of the CD and naming of histograms</b>	<b>109</b>
<b>Appendix F kinsim3</b>	<b>113</b>
F.1 The main function . . . . .	113
F.2 CD simulation . . . . .	113
<b>Appendix G Participants of the experiment</b>	<b>117</b>
<b>Bibliography</b>	<b>119</b>

# Chapter 1

## Introduction

*"If you are not confused by quantum physics then you haven't really understood it."*

– Niels Bohr

The atom was long believed to be the smallest unit of matter, but presently we know that this is false. In fact, the atom consists of both protons and neutrons, which again consists of a multitude of subatomic particles. In the early 1800s, the first evidence-based theories started to be developed around the atom. Still, it would take almost a 100 years before a model of the atom resembling our current theories was proposed and the nucleus was discovered.

In 1911, the famous so-called Rutherford experiment took place. At the suggestion of Ernest Rutherford, Hans Geiger and Ernest Marsden bombarded  $\alpha$ -particles into a thin gold (metal) foil, and observed the scattering of the particles. Rutherford, Geiger and Marsden expected the  $\alpha$ -particles to pass straight through the foil, with little deflection. They were surprised when this did not happen, the  $\alpha$ -particles were observed to have a large spread in scattering angles, sometimes over  $90^\circ$ ! To explain the astonishing results, the existence of a positively charged nucleus<sup>1</sup> at the center of the atom was proposed.

Shortly after, in 1913, Niels Bohr proposed his famous model of the atom, laying the basis of atomic theory. Simply put, the atomic shell model consist of negatively charged electrons in orbits around a positively charged nucleus at the center. The distance from the center to an orbit, or shell, indicate the energy of the electron in the shell. Every electronic shell can maximum contain a specific number of electrons. By studying the ionization energy of electrons, the number of electrons in the innermost orbits were found, yielding the well known sequence of numbers: 2, 8, 10, 18, 36, 54 and 86 [1]. This way, the atomic shell model can explain complicated details of atomic structure and chemistry. For instance the

---

<sup>1</sup>The the first constituent of the nucleus, the proton, was named by Ernest Rutherford in 1920. *Proton* is Greek for "first". It was discovered as  $H^+$ , as early as 1886 by Eugen Goldstein.

least reactive elements we know, the noble gases in the periodic table, are known to fill all their atomic shells to maximum capacity.

At the time when Bohr developed the shell model of the atom, the second constituent of the nucleus, the neutron, was unknown. In 1932, 46 years after the discovery of the proton, the neutron was identified by James Chadwick. The neutron is electrically neutral, and together with the positively charged proton they form the nucleus at the center of the atom.

In nuclear physics, an analogous model to the atomic shell model can be used to explain nuclear structure. In the nuclear shell model, nucleons (protons or neutrons) are filled into nuclear shells in order of increasing energy. The shells of protons and neutrons are independent of each other, i.e. the protons have their own set of shells, separate from the neutron shells. Similar to the atomic shell model, there is a maximum number of protons or neutrons that may fit into each shell. The so-called magic numbers in the nuclear shell model are for the protons ( $Z$ ) and neutrons ( $N$ ) individually

$$\begin{aligned} Z &= \{2, 8, 20, 28, 50, 82\} \\ N &= \{2, 8, 20, 28, 50, 82, 126\} \end{aligned}$$

These series of numbers are one of the main features that shell structure is built upon. A single closed shell nucleus is a nucleus where either  $Z$  or  $N$  are a magic number, while for a doubly closed shell nucleus both  $Z$  and  $N$  are magic numbers.

Maria Goeppert Mayer discovered the magic numbers around 1945 from observation of periodicity in binding energy. At every magic number of neutrons or protons, the binding energy of a nucleus would increase. She noticed that the nuclei with magic numbers had an extra binding energy compared to the predictions of the present model, the semi-empirical mass formula [2]. The nuclear shell model could explain why nuclei with a magic number of protons or neutrons were unusually stable compared to the neighboring non-magic nuclei [3]. She gave Walter Maurice Elsasser credits for being the first to remark that such numbers exists, from an article he wrote in 1933. The scientific community was not instantly convinced by the nuclear shell model. For example, the physicist Eugene Wigner believed in a different theoretical framework called the liquid drop model, and did not trust the new theory. He was the one to coin the term "magic numbers", in what is understood to be an attempt to discredit the nuclear shell model [3, 4].

In addition to the nuclear shell model, there exists a multitude of different microscopic and macroscopic models to describe the nucleus. They all share the common goal of describing the various properties of nuclei, e.g. radius, mass, binding energy, spin, parity, electromagnetic moments and excited states. One of the main objectives of the present experiment is to study such nuclear properties, in particular the nuclear shape of  $^{140}\text{Sm}$ .

A nucleus may have many different shapes, some of which are sketched in [Figure 1.1](#). Nuclei with filled proton or neutron shells, i.e. magic nuclei, generally have a spherical shape, while nuclei with open shells gain energy by taking on a deformed shape.

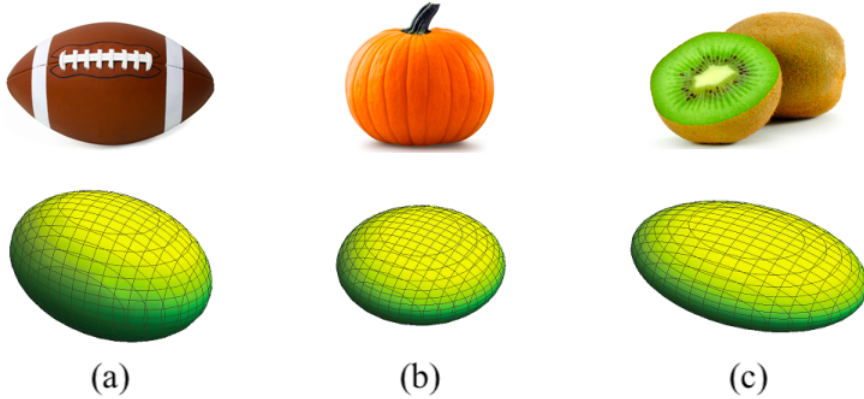


**Figure 1.1:** Nuclear shapes, adapted from [5]. (a) The shape of a elongated (prolate) deformed nucleus looks like an American football, while the shape of (b) a flattened (oblate) deformed nucleus looks like a pumpkin and (c) a triaxial deformed nucleus looks like a kiwi fruit.

The shape of the nucleus can change drastically by adding or removing protons or neutrons. For instance, a neutron deficient isotope may have a different shape than, for example, an isotope with one less neutron or proton. [Figure 1.2a](#) displays the chart of nuclides and their deformation. The red lines corresponds to the magic numbers, i.e. the filling of nuclear shells. At the neutron and proton numbers corresponding to the magic numbers, the isotopes have no deformation, that is, they are spherical, as illustrated by the gray color. In between the red lines, where the nuclear shells are unfilled, we observe regions of deformed nuclei, marked by the colors.

Nuclei in the rare-earth region, especially the samarium (Sm) isotopes, exhibits a variety of shapes. In [Figure 1.2b](#), the theoretically predicted shapes of the Sm isotopes are displayed. The Sm isotope  $^{144}_{62}\text{Sm}_{82}$  has a closed neutron shell, and a spherical shape. By adding neutrons to  $^{144}\text{Sm}$ , the deformation changes very rapidly to an prolate deformed shape at neutron number  $N = 90$  ( $^{152}\text{Sm}$ ). The transition from a spherical to a prolate shape at  $N = 90$  can be interpreted as a shape-phase transition, with the neutron number as control parameter. In this picture,  $^{152}\text{Sm}$  lie at the critical point of the shape-phase transition [6]. At the neutron deficient side, below the  $N = 82$  shell closure,  $^{138}\text{Sm}$  and  $^{140}\text{Sm}$  are expected to have an oblate shape, while the even more neutron deficient Sm isotope  $^{132}\text{Sm}$  is predicted to have a prolate shape.

Some nuclei exhibit what is called shape coexistence, i.e. the coexistence of quantum states corresponding to different shapes. Shape coexistence is often

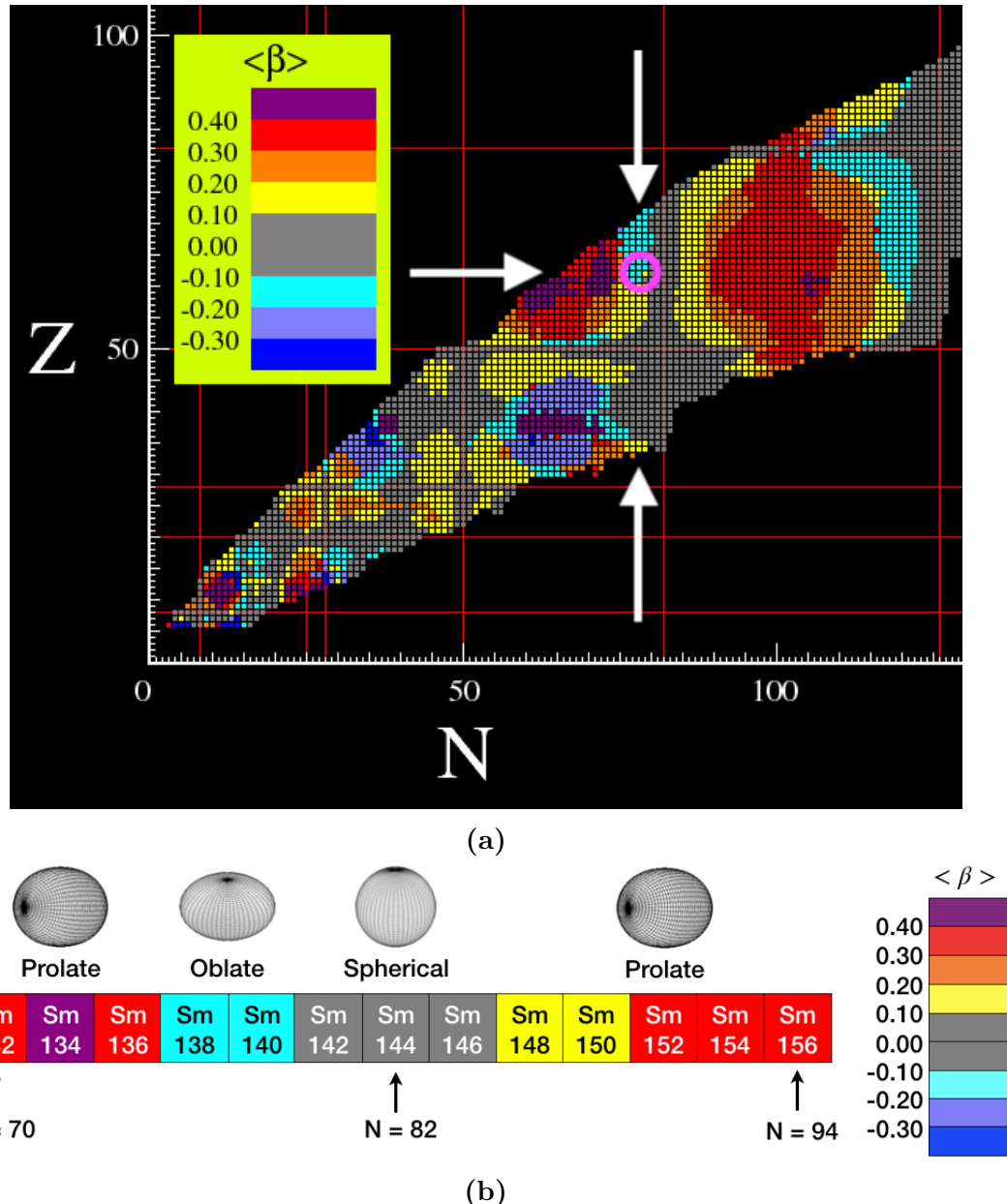


**Figure 1.2:** (a) Chart of nuclides and their deformation, adapted from [7, 8].  $^{140}\text{Sm}$  is visible inside the pink ring, to the left of the yellow square. (b) Sm shape transitions of even-even nuclei based on [7, 8].  $\langle \beta \rangle > 0$  corresponds to a prolate shape,  $\langle \beta \rangle = 0$  corresponds to a spherical shape and  $\langle \beta \rangle < 0$  corresponds to an oblate shape.

found near closed shells, and a typical indication for shape coexistence is  $0^+$  states at low energy. One of the best examples for shape coexistence is the mercury (Hg) isotopes around the isotope  $^{186}_{80}\text{Hg}_{106}$  at neutron mid shell. With a proton

number of  $Z = 80$ , the Hg isotopes are just below the shell closure at  $Z = 82$ . In the same way,  $^{140}\text{Sm}$  is two neutrons below the  $N = 82$  neutron shell closure, and in the middle of the proton shell, see [Figure 1.2b](#). In  $^{140}\text{Sm}$ , two  $0^+$  states are observed at around 1.6 MeV (see [Chapter 5](#)), indicating a possible shape coexistence. One of the objectives of the present work is to clarify the structure of these  $0^+$  states.

In 2012, another Coulomb excitation experiment of  $^{140}\text{Sm}$ , IS495, was conducted at CERN-ISOLDE. The experimental setup at the time was limited to a lower beam energy, which gave a lower Coulomb excitation cross section and a lower probability for multi-step excitations, compared to the present experiment. The results of the IS495 experiment indicated a weak quadrupole deformation with a strong triaxiality or  $\gamma$ -softness in  $^{140}\text{Sm}$ .  $^{140}\text{Sm}$  has therefore a transitional character between spherical and deformed shape. Theoretical models make predictions for nuclei with such symmetries [9], and the present experiment is aiming to test these predictions. The current experiment is an extension to the previous experiment.

In 2017, there was an upgrade of the ISOLDE facility, which lead to the possibility of delivering beam energies up to 7.5 MeV/u. This allowed for Coulomb excitation of  $^{140}\text{Sm}$  at higher energies than the previous experiment. In turn, this implied that it was possible to choose a high- $Z$  target ( $^{208}\text{Pb}$ ) to give a high Coulomb excitation cross section, especially for multi-step excitations. Transition probabilities and quadrupole moments between several excited states in  $^{140}\text{Sm}$  are still unknown. With the present experiment we want to measure  $B(E2)$  values and quadrupole moments for higher-lying states. This will give a greater understanding of the nuclear structure in  $^{140}\text{Sm}$ . Especially transitions from excited  $0^+$  states will give information about possible shape coexistence or critical-point symmetry.

Another goal is to make the procedure of a data analysis code named *MiniballCoulexSort* more transparent. All scripts and programs developed in this work are available in the authors GitHub repository [10].

The present thesis is structured in the following way. [Chapter 2](#) outlines the theory of nuclear deformation and the Coulomb excitation method. The ISOLDE facility and the experimental setup utilized to extract particle gamma coincidences will be presented in [Chapter 3](#). By means of the analysis code named *MiniballCoulexSort*, the data was sorted and calibrated, as explained in [Chapter 4](#). In [Chapter 5](#), the resulting Doppler corrected  $\gamma$  spectrum is presented. [Chapter 6](#) summarizes of the thesis and outlines the future work of the Coulomb excitation analysis of  $^{140}\text{Sm}$ . [Appendix A](#) lists acronyms and abbreviations applied in the thesis. The remainder of the appendix is referenced when required in the text.



# Chapter 2

## Theory

*"I think I can safely say that nobody understands quantum mechanics."*

– Richard Feynman

### 2.1 Nuclear deformation

It is natural to imagine nuclei as tiny spheres. Although the nucleus is a fuzzy quantum object, we can still associate a macroscopic shape with it. Thus, we can define shape parameters that quantify the degree of deformation in the intrinsic system of the nucleus. These shapes can fluctuate (vibrations), and a deformed nucleus can also rotate in space<sup>1</sup>. In the case of a rotation, the intrinsic shape does not change, but the description in the laboratory frame becomes time dependent. Although we can associate a deformation to a nucleus, the constituent nucleons does not necessarily form a rigid system. The nuclear moment of inertia is typically smaller than for a rigid system of the same deformation, and may, in fact, vary depending on the state of the nuclear system in question. Consider a raw and a boiled egg as an example. The two systems have the same shape, but the system of a boiled egg is closer to a rigid body than a system of a raw egg, and their moment of inertia are not identical.

Figure 2.1 displays a sketch of a deformed vibrating nucleus. The figure illustrates how the shape oscillates between the outer and inner extreme shapes (solid lines) by transitioning through the equilibrium shape of a sphere (dotted lines). One way to parameterize the instantaneous surface of the nucleus is to describe it by a vector  $\mathbf{R}$  pointing from the origin to a surface point given by the angles  $\theta$  and  $\phi$  [11]. This is called the multipole expansion, and is given by the

---

<sup>1</sup>The rotation of a spherical nucleus is trivial, since the shape remains identical after any rotation in space. Therefore, a deformation is required to discuss a rotating nucleus.

following equation

$$\mathbf{R}(\theta, \phi) = R_0 \left( 1 + a_{00} + \sum_{\lambda=1}^{\infty} \sum_{\mu=-\lambda}^{+\lambda} a_{\lambda\mu} Y_{\lambda\mu}(\theta, \phi) \right) \quad (2.1)$$

where  $R_0$  is the radius of the sphere,  $a_{00}$  describes volume changes, and  $a_{\lambda\mu}$  are the expansion coefficients, or the deformation parameters. The parametrization involves the spherical harmonics  $Y_{\lambda\mu}$ , where  $\lambda$  is the multipole order,  $\mu$  is the projection of  $\lambda$  and  $\theta$  and  $\phi$  are the intrinsic angles [11–13]. Figure 2.2 displays examples of fluctuations in dipole, quadrupole and octupole parameters ( $\lambda$ ). By assuming incompressibility of the nucleus, the volume is kept constant, given by

$$V = \frac{4}{3}\pi R_0^3$$

and the nuclear radius can be approximated by

$$R_0 = r_0 A^{1/3} \quad (2.2)$$

where the proportionality constant is given by  $r_0 \approx 1.25$  fm and  $A$  is the mass number of the nucleus.

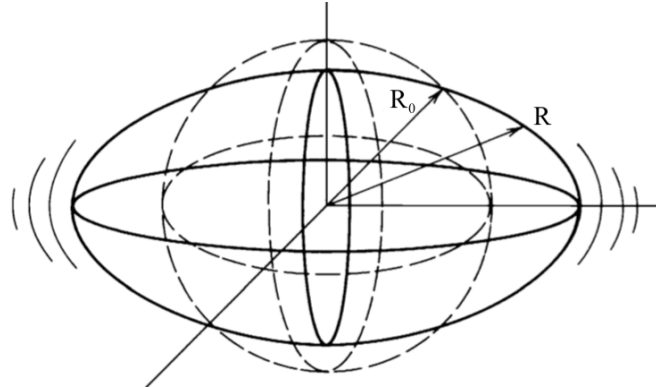


**Figure 2.1:** A deformed vibrating nucleus, adapted from [11]. In the drawing, the dotted lines represent the spherical equilibrium shape. The drawing is exaggerated to visualize the deformation. See the text for more information.

The expansion coefficients,  $a_{\lambda\mu}$ , can be time dependent and can thus describe a vibration or rotation in space of the nucleus. Up to second order, the expansion coefficients are given as

$$a_{00} = -\frac{1}{4\pi} \sum_{\lambda>1,\mu} |a_{\lambda\mu}|^2 \quad (2.3)$$

The dipole term,  $\lambda = 1$ , describes a translation, i.e. the movement, of the

whole system, which is uninteresting in itself. A large majority of nuclei can be described by quadrupole ( $\lambda = 2$ ) shapes. Higher-order deformations only play a role in a few selected regions of the nuclear chart. By putting the origin of the coordinate system in the center of mass, it is possible to fix and exclude the  $a_{1\mu}$  parameters, and thus also  $a_{00}$  [12]. If we restrict the system to small deformations, we achieve  $a_{1\mu} = 0$  and thus  $a_{00} = 0$ . Then, [Equation \(2.1\)](#) can be reduced to

$$\mathbf{R}(\theta, \phi) = R_0 \left( 1 + \sum_{\lambda=2}^{\infty} \sum_{\mu=-\lambda}^{+\lambda} a_{\lambda\mu} Y_{\lambda\mu}(\theta, \phi) \right) \quad (2.4)$$

The quadrupole deformation,  $\lambda = 2$ , is the most important mode. It describes the shape of the nucleus and is the dominant feature in most of the deformed nuclei. In nuclei with spherical shape, the quadrupole vibrations are the lowest mode of collective excitations. A quadrupole phonon excitation generates a  $2^+$  state. Two-phonon excitations can couple to spins ( $0^+, 2^+, 4^+$ ). Deformed nuclei, on the other hand, have low lying rotational states, which are characterized by  $E \propto I(I+1)$ .

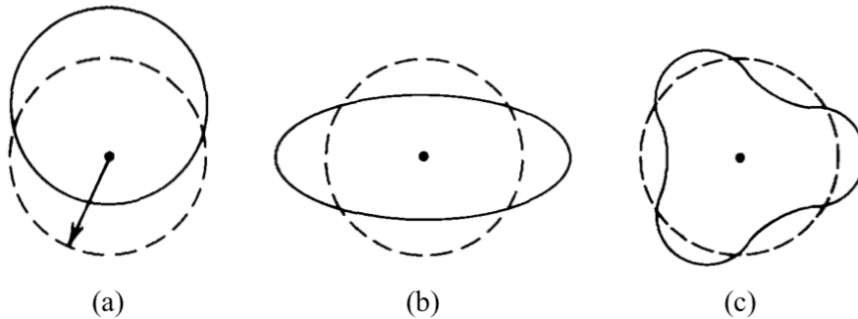


**Figure 2.2:** Vibrational modes, adapted from [11]. The dotted lines represent the spherical equilibrium shape. (a) Dipole,  $\lambda = 1$ . (b) Quadrupole,  $\lambda = 2$ . (c) Octupole,  $\lambda = 3$ .

For  $\lambda = 2$ , there are five parameters of  $a_{2\mu}$  ( $\mu \in \{-2, -1, 0, 1, 2\}$ ). Two parameters describe the shape, and in addition there are three parameters describing the orientation in space. It is possible to align the deformed shape in a coordinate system such that only two parameters are needed to describe the shape of the nucleus. With a suitable rotation, we can achieve

$$\begin{aligned} a_{21} &= a_{2,-1} = 0 \\ a_{22} &= a_{2,-2} \end{aligned}$$

leaving two independent parameters,  $a_{20}$  and  $a_{22}$ . With Hill-Wheeler [14] coor-

dinates  $(\beta, \gamma)$  they become

$$a_{20} = \beta \cos \gamma \quad (2.5)$$

$$a_{22} = \frac{1}{\sqrt{2}} \beta \sin \gamma \quad (2.6)$$

where  $\beta$  is the axial deformation (deformation magnitude) and  $\gamma$  is the triaxial deformation (shape parameter). If axial symmetry is assumed,  $\beta > 0$  and  $\gamma = 0$  corresponds to the prolate deformed shape, while  $\beta > 0$  and  $\gamma = 60^\circ$  corresponds to the oblate shape. The triaxial shape is obtained when  $0 < \gamma < \frac{\pi}{3}$ . Further we have

$$\sum_{\mu} |a_{2\mu}|^2 = a_{20}^2 + 2a_{22}^2 = \beta^2 \quad (2.7)$$

In the special case of  $\lambda = 2$ , Equation (2.4) becomes

$$\mathbf{R}(\theta, \phi) = R_0 \left( 1 + \beta \sqrt{\frac{5}{16\pi}} (\cos \gamma (3 \cos^2 \theta - 1) + \sqrt{3} \sin \gamma \sin^2 \theta \cos 2\phi) \right) \quad (2.8)$$

by using the spherical harmonics  $Y_{20}$  and  $Y_{2,\pm 2}$  [12].

The equilibrium shape of a nucleus can be characterized by a potential energy surface (PES) in the  $\beta$ - $\gamma$  plane if we restrict the deformation to quadrupole shapes ( $\lambda = 2$ ). Figure 2.3 displays sketches of three extreme cases of PES; a spherical vibrator, a deformed rotor and a  $\gamma$ -soft rotor. In the PES, an increasingly steep minimum implies a more rigid deformation. Accordingly, a more shallow potential suggest that the shape is softer against vibrations. Two competing shapes, i.e. shape coexistence, would show up as two minima in the PES. Figure 2.4 shows the PES of  $^{140}\text{Sm}$ . It is essentially flat in both  $\beta$  and  $\gamma$  direction. That is consistent with an interpretation of  $^{140}\text{Sm}$  as a transitional nucleus in between spherical and deformed, and in between prolate and oblate shape.

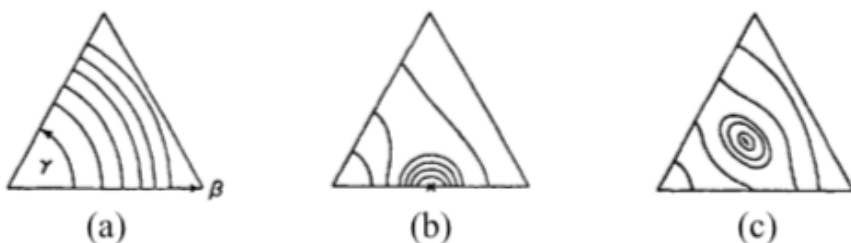


**Figure 2.3:** Potential energy surface, adapted from [1]. (a) Spherical vibrator. (b) Deformed rotor. (c)  $\gamma$ -soft rotor. See the text for more information.

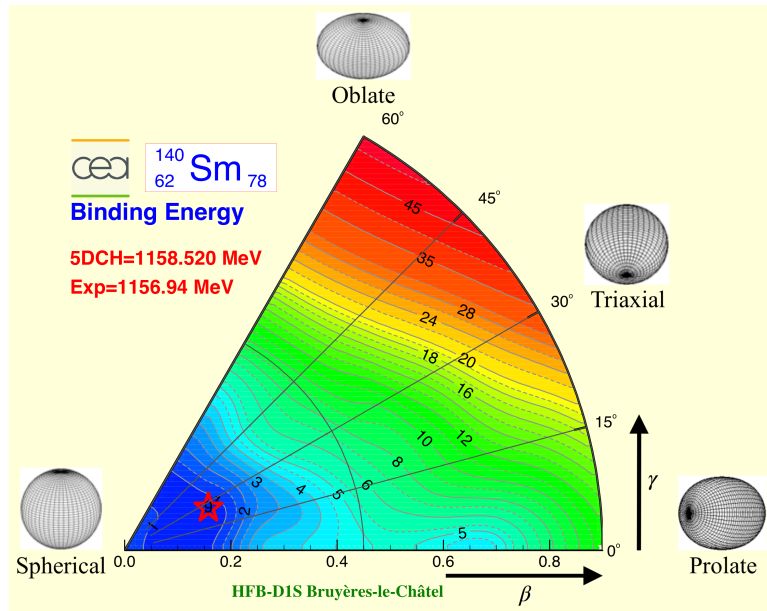


**Figure 2.4:** Potential energy surface for  $^{140}\text{Sm}$ , adapted from [7, 8]. See the text for more information.

Octupole vibration,  $\lambda = 3$ , with  $J^\pi = 3^-$  state can be observed in many nuclei in certain regions of the nuclear chart, where orbitals with a spin difference of 3 are available near the Fermi surface. In nuclei where the shell structure causes the quadrupole modes to occur at very high energies, such as in doubly magic nuclei, the octupole state is often the lowest excited state. The octupole deformation can be described to have the shape of a pear.

## 2.2 Coulomb excitation method

COULomb EXcitation (COULEX) is an experimental method to excite a nucleus by an inelastic scattering with another nucleus by means of the electromagnetic interaction. This method is very useful for studying collective excitations and shapes of nuclei, as they are often connected by electric quadrupole (E2) transitions. Transition energies and intensities can be used to determine new excited levels and study deformation. An extensive description of Coulomb excitation can be found in [15–17].

Figure 2.5 present two sketches of the scattering process, one in the LABoratory (LAB) frame of reference and one in the Center of Mass (CM) frame of reference. In the LAB frame, a beam particle approaches the target with a velocity  $\mathbf{u}$ . The beam particle gets excited by the electromagnetic interaction with the target particle. It is of course also possible that the target nucleus gets excited, or that there is no excitation, i.e. elastic scattering. It is even possible, although

not very likely, that the both target and the projectile get excited simultaneously. Here, we are only considering the case where the projectile gets excited. As the newly excited energy state is unstable, it will rapidly de-excite after its formation, sending out a  $\gamma$ -ray. Both the beam and target particles are scattered with a velocity  $\mathbf{v}_b$  and  $\mathbf{v}_t$ , respectively. The distance,  $b$ , is called the impact parameter and is the vertical distance between the beam and target particle, as indicated by the arrows in [Figure 2.5](#).  $V_{cm}$  is the center of mass velocity. The angles  $\theta_b$  and  $\theta_t$  are the scattering angles of the beam and target particle, respectively. A small angle  $\theta_b$  means forward scattering of the beam, a larger distance between the beam particle and the target particle, a weaker electromagnetic (EM) field and a decreased excitation probability. A large angle  $\theta_b$  means backward scattering of the beam, a closer distance between the beam particle and the target particle, a stronger EM field and a higher excitation probability. In the CM frame, the center of mass velocity is zero, and the velocities and angles are marked by an apostrophe to separate between the two frames of reference.

The Coulomb scattering kinematics can be approximated by an elastic collision. In [Appendix D](#), a calculation of the two-particle elastic collision is performed.

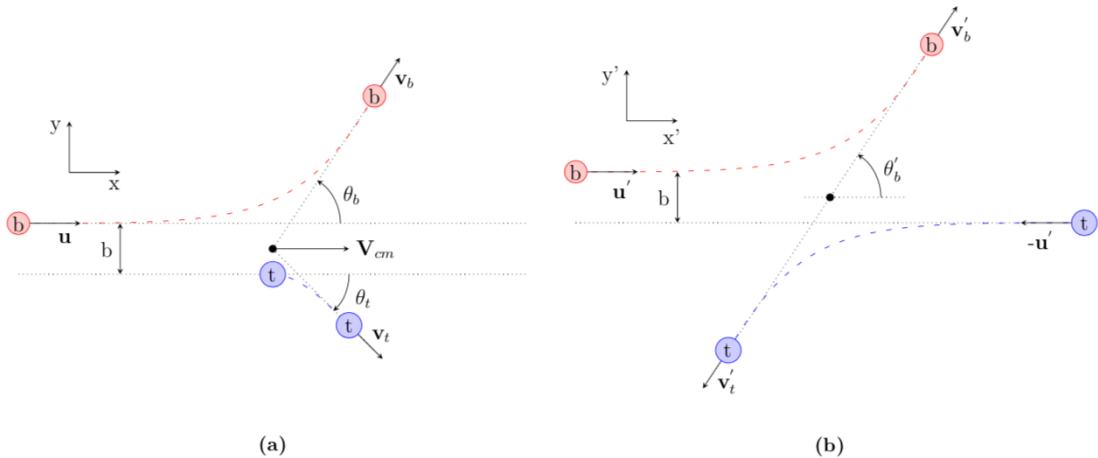


**Figure 2.5:** A visualisation of the separate frames of reference for the scattering reaction relevant to the COULEX. **(a)** Scattering in the LABoratory (LAB) frame. **(b)** Scattering in the Center of Mass (CM) frame. See the text for more information.

In the semi-classical approach of Coulomb excitation theory, the projectile (beam) and target is assumed to move on hyperbolic paths. This approach does not take into account the energy loss during the excitation process. When the beam particle approaches the target particle, the beam particle reaches a minimum separation distance,  $d$ , which is dependent on the impact parameter  $b$ . The distance of closest approach,  $d$ , is the distance between the center of both

nuclei. In a head-on collision,  $b = 0$  and the particles reach the distance of closest approach  $d$ , which is given by

$$d(\theta'_b) = a \left( 1 + \csc\left(\frac{\theta'_b}{2}\right) \right) = a \left( 1 + \frac{1}{\sin\left(\frac{\theta'_b}{2}\right)} \right) \text{ [fm]} \quad (2.9)$$

The scattering angle of the beam in the CM frame is  $\theta'_b$ . Half the distance of closest approach,  $a$ , in a head-on collision ( $\theta'_b = 180^\circ$ ) is given by

$$a = \frac{1}{2}d = \frac{Z_b Z_t e^2}{m_r v_i^2} \text{ [fm]} \quad (2.10)$$

where  $Z_b$  and  $Z_t$  is the proton number of the beam and target, respectively. The elementary charge is  $e$ , the initial velocity of the beam is  $v_i$ , and  $m_r$  is the reduced mass of the beam and target given by

$$m_r = m_b \frac{A_b A_t}{A_b + A_t} = m_b A_r \left[ \frac{\text{MeV}}{c^2} \right], \quad A_r = \frac{A_b A_t}{A_b + A_t} \quad (2.11)$$

Here,  $m_b$  is the mass of the beam particle, and  $A_r$  is the reduced mass number of the beam and target [16, 18]. Then, the impact parameter can be expressed as

$$b = a \cot\left(\frac{\theta'_b}{2}\right) \quad (2.12)$$

One requirement in the semi-classical approach is that the asymptotic wavelength of relative motion of the beam, i.e. the de Broglie wavelength  $\lambda = \hbar/m_r v_i$ , must be small compared to the distance of closest approach,  $d$  [16, 18]. The ratio of half the distance of closest approach and the de Broglie wavelength defines the Sommerfeld parameter,  $\eta$ , which measures the strength of the Coulomb interaction [19]. It is given by

$$\eta = \frac{d}{2\lambda} = \frac{a}{\lambda} = \frac{Z_b Z_t e^2}{m_r v_i^2} = \frac{Z_b Z_t e^2}{\hbar v_i} \approx 0.72 \frac{Z_b Z_t}{A_r E_b} \quad (2.13)$$

where  $E_b = \frac{1}{2}m_b v_i^2$  is the initial kinetic energy of the beam given in MeV/u [18]. A requirement for describing the relative motion of the particles in the CM frame by hyperbolic paths is that  $\eta \gg 1$ . This condition is generally fulfilled for Coulomb excitation with heavy ions. The factor 0.72 is derived from

$$\frac{e^2}{2} = \frac{(\sqrt{1.4399764 \text{ [MeV} \cdot \text{fm}]})^2}{2} \approx 0.72 \text{ [MeV} \cdot \text{fm}] \quad (2.14)$$

The probability of exciting the nucleus from a initial state  $|i\rangle$  to a final state

$|f\rangle$  with excitation energy difference  $\Delta E = E_f - E_i$  is dependent on the adiabaticity parameter [18, 20, 21], given by

$$\xi = \frac{\tau_c}{\tau_{ex}} = \frac{a}{\hbar v_i} \Delta E = \frac{Z_b Z_t e^2}{\hbar v_i} \cdot \frac{\Delta E}{2E_b} = \eta \cdot \frac{\Delta E}{2E_b} \quad (2.15)$$

Here,  $\tau_c = \frac{a}{v_i}$  is the collision time, and  $\tau_{ex} = \frac{\hbar}{\Delta E}$  is the excitation time. If  $\xi \ll 1$  the reaction process is sudden and the excitation probability is largest, while if  $\xi \gg 1$  the reaction becomes adiabatic, which means that the reaction process is hindered. The excitation probability decreases exponentially with increasing  $\xi$ . A semi-classical approach of the Coulomb excitation is a good approximation if the conditions  $\eta \gg 1$  and  $\xi \ll 1$  are fulfilled. This means that the energy transfer has negligible influence of the motion and thus

$$\frac{\Delta E}{E_b} \ll 1 \quad (2.16)$$

which holds only for low-lying states and limits the excitation energy that can be reached [16, 18].

### 2.2.1 Safe COULEX

In order to ensure that the interaction is purely electromagnetic in nature, and not nuclear, a so-called safe energy is chosen for the reaction. The energy is supposed to be below the Coulomb barrier. Safe COULEX is when the distance of closest approach between the particles is large enough to exclude nuclear interactions. The safety distance,  $d_{safe}$ , in safe COULEX is chosen by the condition

$$\begin{aligned} d_{safe} &\geq d_{min} = d_C + d_s \\ &= R_b + R_t + d_s \\ &= r_0(A_b^{1/3} + A_t^{1/3}) + d_s \\ &= 1.25(A_b^{1/3} + A_t^{1/3}) + 5 \text{ [fm]} \end{aligned} \quad (2.17)$$

where  $d_{min}$  is an approximation of the distance of closest approach by the Coulomb interaction distance,  $d_C$ , and an additional safety distance,  $d_s = 5$  fm.  $R_b$  and  $R_t$  is the radii of the beam and target nuclei, respectively, and  $A_b$  and  $A_t$  is the mass number of the beam and target nuclei, respectively [18, 22].

The maximum beam energy in the LAB frame,  $E_{b,max}$ , is chosen from the

special case when  $\theta'_b = 180^\circ$  [13, 18]

$$E_{b,max}(\theta'_b) = \frac{Z_b Z_t e^2}{A_r d_{min}} \frac{2}{1 + \csc\left(\frac{\theta'_b}{2}\right)} \quad (2.18)$$

$$\approx \frac{Z_b Z_t}{A_r} \frac{1.44}{1.25(A_b^{1/3} + A_t^{1/3}) + 5} \left[ \frac{\text{MeV}}{\text{u}} \right] \quad (2.19)$$

In the CM frame, the kinetic energy is given by

$$E' = E_b - E_t = \frac{A_t}{A_b + A_t} E_b \quad (2.20)$$

where  $A_b$  and  $A_t$  is the mass number of the beam and target nuclei and  $E_b$  is the kinetic energy of the beam particle in the LAB frame [20, 21]. The recoil energy,  $E_t$ , of the total system can be expressed as

$$E_t = \frac{A_b}{A_b + A_t} E_b \quad (2.21)$$

For the Coulomb reaction, only the energy,  $E'$ , and relative momentum in the CM frame is available for the excitation process.

### 2.2.2 Cross sections

For point-like charges, the differential scattering cross section,  $d\sigma_R$ , is given by the the classical Rutherford formula

$$\begin{aligned} \frac{d\sigma_R}{d\Omega} &= \frac{a^2}{4 \sin\left(\frac{\theta'_b}{2}\right)} \\ &= \left(\frac{Z_b Z_t e^2}{4\pi\varepsilon_0}\right)^2 \left(\frac{1}{4E_b}\right)^2 \frac{1}{\sin^4\left(\frac{\theta'_b}{2}\right)} \\ &= \left(\frac{Z_b Z_t e^2}{8\pi\varepsilon_0 m_b v_0'^2}\right)^2 \frac{1}{\sin^4\left(\frac{\theta'_b}{2}\right)} \end{aligned} \quad (2.22)$$

Here,  $d\Omega$  is the solid angle,  $Z_b$  and  $Z_t$  is the proton number of the beam and target nuclei, respectively.  $e$  is the elementary charge,  $\varepsilon_0$  is the electric permittivity in vacuum,  $m_b$  is the mass of the beam particle.  $v_0'$  is the initial velocity of the beam particle in the CM frame and  $\theta'_b$  is the beam particle scattering angle in the CM frame [11, 13, 16].

Under the condition  $\xi \ll 1$ , the differential cross section,  $d\sigma_{i \rightarrow f}$ , for inelastic

scattering of point-like objects from the initial state  $|i\rangle$  to the final state  $|f\rangle$  is given by

$$\frac{d\sigma_{i \rightarrow f}}{d\Omega} = \frac{d\sigma_R}{d\Omega} \cdot P_{i \rightarrow f} \quad (2.23)$$

The excitation probability,  $P_{i \rightarrow f}$ , can be expressed as

$$P_{i \rightarrow f} = \frac{1}{2I_i + 1} \sum_{M_i, M_f} |a_{if}|^2 \quad (2.24)$$

where  $I_i$  is the spin of the state  $|i\rangle$ , and  $M_i$  and  $M_f$  is the angular momentum projections of initial and final states, respectively [16, 21].  $a_{if}$  is the excitation amplitudes summed over all magnetic substates, which can be expressed by

$$a_{if} = \frac{1}{i\hbar} \int_{-\infty}^{\infty} e^{i\frac{\Delta E}{\hbar}t} \langle f | H(t) | i \rangle dt \quad (2.25)$$

where  $\Delta E = E_f - E_i$  is the energy difference of the final and initial state, respectively.  $H(t)$  is the time-dependent electromagnetic interaction between the beam and the target [13, 20, 21].

The total electric excitation cross section from a state  $|i\rangle$  to a state  $|f\rangle$  is given by

$$\sigma_E = \sum_{\lambda} \sigma_{E\lambda} \quad (2.26)$$

with

$$\sigma_{E\lambda} = \left( \frac{Z_b e}{\hbar v_i} \right)^2 a^{-2\lambda+2} B(E\lambda; I_i \rightarrow I_f) f_{E\lambda}(\xi) \quad (2.27)$$

The reduced transition probability,  $B(E\lambda)$ , is related to the matrix elements of the electric multipole order by

$$B(E\lambda; I_i \rightarrow I_f) = \frac{1}{2I_i + 1} |\langle f | \mathcal{M}(E\lambda) | i \rangle|^2 \quad (2.28)$$

and the Coulomb excitation function,  $f_{E\lambda}(\xi)$  is given by

$$f_{E\lambda}(\xi) = \int_{\Omega} df_{E\lambda}(\theta'_b, \xi) \quad (2.29)$$

where the integration is performed over all scattering angles of the solid angle  $\Omega$  in the CM frame [16, 20]. The Coulomb excitation function is dependent on  $\xi$  and the multipolarity. In the special case of  $E2$  transitions and  $\xi \ll 1$ , we have

$f_{E\lambda}(\xi) \approx 1$ . Setting  $\lambda = 2$  and applying  $B(E2)$  in [Equation \(2.27\)](#), it can be shown that the electric excitation probability [\[21\]](#) can be approximated by:

$$\sigma_{E2} \approx \left( \frac{Z_b e}{\hbar v_i} \right)^2 a^{-2} = \left( \frac{mv_i}{Z_t e \hbar} \right)^2 \quad (2.30)$$

Similar to the total electric cross section, the total magnetic cross section can be expressed as [\[16\]](#)

$$\sigma_M = \sum_{\lambda} \sigma_{M\lambda} = \left( \frac{Z_b e}{\hbar c} \right)^2 \sum_{\lambda} a^{-2\lambda+2} B(M\lambda; I_i \rightarrow I_f) f_{M\lambda}(\xi) \quad (2.31)$$

Notice that  $E$  has been replaced by  $M$ , and the  $1/c$  factor in the first fraction. This means that magnetic excitations are suppressed by a factor  $(v/c)^2$ , which implies that, in practice, magnetic excitations do not play a significant role. The excitation process is purely electric, but the decay of the excited states can be both electric and magnetic.

### 2.2.3 Transition probabilities

The transition probability of going from a state  $|i\rangle$  to a state  $|f\rangle$  is

$$T_{i \rightarrow f}(\sigma\lambda) = \frac{8\pi(\lambda+1)}{\lambda\hbar[(2\lambda+1)!!]^2} \left( \frac{E_\gamma}{\hbar c} \right)^{2\lambda+1} B(\sigma\lambda; I_i \rightarrow I_f) \quad (2.32)$$

where  $\sigma\lambda$  is the multipolarity with  $\sigma \in \{E, M\}$ . Transition with the lowest multipolarity, i.e. small  $\lambda$ , are most likely, while transitions of high multipolarity are relatively unlikely. Electric transitions are generally more probable than magnetic transitions of the same multipolarity. The reduced transition probability is

$$\begin{aligned} B(\sigma\lambda; I_i \rightarrow I_f) &= \sum_{M_i, M_f} |\langle I_f M_f | \hat{O}_{\lambda\mu} | I_i M_i \rangle|^2 \\ &= \frac{1}{2I_i + 1} |\langle I_f | \hat{O}_{\lambda\mu} | I_i \rangle|^2 \end{aligned} \quad (2.33)$$

and  $\hat{O}_{\lambda\mu} \in \{\hat{E}_{\lambda\mu}, \hat{M}_{\lambda\mu}\}$  is the electric or magnetic multipole operator. By measuring transition probabilities it is possible to measure  $B(E2)$  values (or other multipolarities). These quantities are closely related to the nuclear shape, and can be compared to theoretical calculations.

The reduced transition probabilities are not identical if the spin states are

interchanged

$$B(\sigma\lambda; I_f \rightarrow I_i) \neq B(\sigma\lambda; I_i \rightarrow I_f) \quad (2.34)$$

while an interchange of the reduced matrix elements yields an equal result

$$|\langle I_f | \hat{O}_{\lambda\mu} | I_i \rangle|^2 = |\langle I_i | \hat{O}_{\lambda\mu} | I_f \rangle|^2 \quad (2.35)$$

The relation of the reduced transition probability between the excitation  $B(E2 \uparrow)$  and the decay  $B(E2 \downarrow)$  of a state, can be expressed as

$$B(E2; I_f \rightarrow I_i) = \frac{2I_i + 1}{2I_f + 1} B(E2; I_i \rightarrow I_f) \quad (2.36)$$

For an  $E2$  transition from the ground state  $0_1^+$  and the first excited state  $2_1^+$ , we have the relation

$$B(E2; 0_1^+ \rightarrow 2_1^+) = 5 \cdot B(E2; 2_1^+ \rightarrow 0_1^+) \quad (2.37)$$

For the excitation from a  $0_1^+$  to a  $2_1^+$  state, there are five times as many final substates available compared to the corresponding de-excitation process, as illustrated by [Figure 2.6](#).

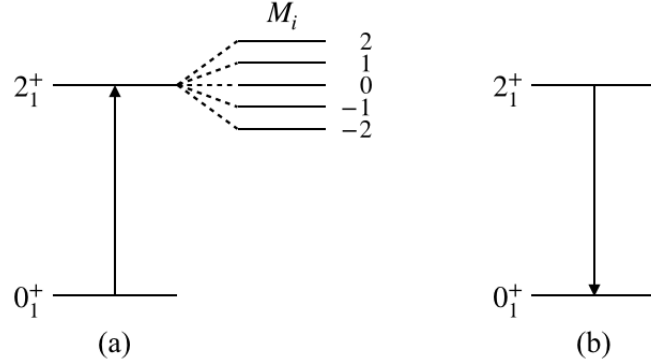


**Figure 2.6:** (a) Excitation probability. (b) Decay probability.

[Table 2.1](#) displays the selection rules for  $\gamma$  transitions, where the parity [11] is decided by

$$\pi(\sigma\lambda) = \begin{cases} (-1)^\lambda, & \text{for } \sigma\lambda = E\lambda \\ (-1)^{\lambda+1}, & \text{for } \sigma\lambda = M\lambda \end{cases} \quad (2.38)$$

and angular momentum conservation gives

$$|I_i - I_f| \leq \lambda \leq I_i + I_f \quad (2.39)$$

**Table 2.1:**  $\gamma$  transition selection rules. Electric transitions are more likely than magnetic transitions of the same multipole  $\lambda$ . There are no  $\gamma$  transitions with  $\lambda = 0$ , i.e.  $I_i = 0 \rightarrow I_f = 0$  is not allowed. The  $0 \rightarrow 0$  transitions must proceed via internal conversion or internal pair creation.

$ \Delta I $	0	1	2	3	4
$\Delta\pi = \text{yes}$	E1	E1	M2	E3	M4
	(M2)	(M2)	E3	(M4)	E5
$\Delta\pi = \text{no}$	M1	M1	E2	M3	E4
	E2	E2	(M3)	E4	(M5)

## 2.2.4 Electric quadrupole moments

The electric quadrupole moment is a parameter that describes the charge distribution of a nucleus and thus its shape. In the classical definition it is given by

$$Q_{ij} = \int \rho(\mathbf{r})(3r_i r_j - r^2 \delta_{ij}) d^3 \mathbf{r} \quad (2.40)$$

where  $\rho$  is the charge density distribution,  $\mathbf{r} = (r_1, r_2, r_3) = (x, y, z)$  are the Cartesian coordinates,  $i, j \in \{1, 2, 3\}$  and

$$\delta_{ij} = \begin{cases} 0, & \text{if } i \neq j \\ 1, & \text{if } i = j \end{cases} \quad (2.41)$$

is the Kronecker delta. It is possible to rotate the frame such that the  $z$ -axis coincides with the symmetry axis. With axial symmetry [20, 23], we choose the  $z$ -axis along the symmetry axis, yielding

$$\begin{aligned} Q_z &= \int \rho(\mathbf{r})(3z^2 - r^2) d\mathbf{r} \\ &= \int \rho(\mathbf{r})(3\cos^2 \theta - 1) d\mathbf{r} \\ &= \sqrt{\frac{16\pi}{5}} \int \rho(\mathbf{r})r^2 Y_{20}(\theta, \phi) d\mathbf{r} \\ &= Q_{20} \end{aligned} \quad (2.42)$$

Due to the symmetry of the system, we have  $Q_x = Q_y$ , implying that the charge distribution is fully characterized by  $Q_z$ . In this case,  $Q_z = 0$  corresponds to a spherical shape, while  $Q_z > 0$  corresponds to a prolate shape and  $Q_z < 0$

corresponds to an oblate shape. In the same way as  $Q_{20}$ , it is possible to define

$$Q_{22} = \sqrt{\frac{16\pi}{5}} \int \rho(\mathbf{r}) r^2 Y_{22}(\theta, \phi) d\mathbf{r} \quad (2.43)$$

Using the definitions of  $Q_{20}$  and  $Q_{22}$ , we can now describe all quadrupole shapes in a similar manner to the  $\beta$  and  $\gamma$  parameters described in [Section 2.1](#). The electric quadrupole moments  $Q_{20}$  and  $Q_{22}$  are defined in the intrinsic frame of the nucleus. For a state with spin  $I$  we can observe the spectroscopic quadrupole moment

$$Q_s(I) = \langle I, m = I | \hat{Q}_{20} | I, m = I \rangle \quad (2.44)$$

$$= \sqrt{\frac{I(2I-1)}{(2I+1)(2I+3)(I+1)}} \langle I | \hat{Q}_2 | I \rangle \quad (2.45)$$

where  $\hat{Q}_2$  is the electric multipole operator [12] from

$$\hat{Q}_{\lambda\mu} = \int \rho(\mathbf{r}) r^\lambda Y_{\lambda\mu}(\theta, \phi) d^3\mathbf{r} \quad (2.46)$$

The spectroscopic quadrupole moment is what we can observe in the LAB frame. Here we see that  $I = 0$  or  $\frac{1}{2}$  gives  $Q_s = 0$ , which means that a nucleus with these spins may have intrinsic an deformation, but it cannot be measured via the spectroscopic quadrupole moment [23].

The intrinsic quadrupole moment,  $Q_0$ , is defined in the body-fixed frame. It is related to the spectroscopic quadrupole moment via

$$Q_s = \frac{3K^2 - I(I+1)}{(I+1)(2I+3)} Q_0 \quad (2.47)$$

where  $K$  is the projection of total angular momentum onto the body-fixed symmetry axis.  $K$  is only defined if there is a symmetry axis, i.e. if the nucleus has rotational symmetry. If the total angular momentum is perpendicular to the symmetry axis, then  $K = 0$ . The intrinsic quadrupole moment,  $Q_0$ , reflects the nuclear deformation,  $\beta$ , and is related via [13, 24]

$$\begin{aligned} Q_0 &= \int \rho(\mathbf{r})(3z^2 - r^2) d\mathbf{r} \\ &\approx \frac{3}{\sqrt{5\pi}} Z R^2 (\beta + 0.16\beta^2) \end{aligned} \quad (2.48)$$

If the intrinsic shape is prolate,  $Q_0 > 0$ , the measured spectroscopic quadrupole moment shows an oblate shape in the laboratory frame,  $Q_s < 0$ . Correspondingly, a prolate deformed nucleus rotating rapidly about the perpendicular axis appears

to be oblate. It is possible to directly distinguish between a prolate or an oblate shape if we obtain information about  $Q_s$  and the relative signs of the matrix elements. Nuclei with spin  $I = 0$  or  $I = \frac{1}{2}$  can have an intrinsic deformation, but the shape cannot be measured because  $Q_s = 0$ .



# Chapter 3

## Coulomb excitation experiment

*"If I could remember the names of all those particles, I'd be a botanist."*

– Enrico Fermi

The present experiment, IS558, was conducted at the CERN-ISOLDE facility between 8th and 14th of August in 2017. A beam of  $^{140}\text{Sm}$  ions was accelerated into a target of  $^{208}\text{Pb}$  at 4.65 MeV/u with the objective of studying the transitions and deformation of  $^{140}\text{Sm}$ . In the following chapter, the details of the experimental setup utilized in the present work will be outlined.

### 3.1 ISOLDE at CERN

ISOLDE is a Radioactive Ion Beam (RIB) facility at CERN in Meyrin, Switzerland. Figure 3.1 shows the CERN accelerator complex, where ISOLDE is located beside the Proton Synchrotron Booster (PSB), in the lower right marked by a green box. The acronym ISOLDE stands for Isotope Separator On Line DDevice. The facility can produce over 1000 different radionuclides to be used in a wide variety of experiments in nuclear physics, atomic physics, solid state physics, life sciences and fundamental interactions. Experiments have been performed at ISOLDE since 1967 and since 2001 experiments with post-accelerated RIBs have been conducted [25–27]. The High Intensity and Energy upgrade (HIE-ISOLDE) made it possible to deliver beam energies up to 7.5 MeV/u in July 2017 [28]. The present experiment was one of the first Miniball experiments with the upgraded superconducting LINear ACcelerator (LINAC), the HIE-ISOLDE LINAC. Further upgrades, after the present experiment, have made it possible to deliver beam energies up to 10 MeV/u in 2018 [25].

In general, it is very challenging to study radioactive, short lived nuclei. The newest edition of the Karlsruhe Nuclide Chart have nuclear data of over 4000 nuclides, and most of these are radioactive [30]. In many cases it is not possible

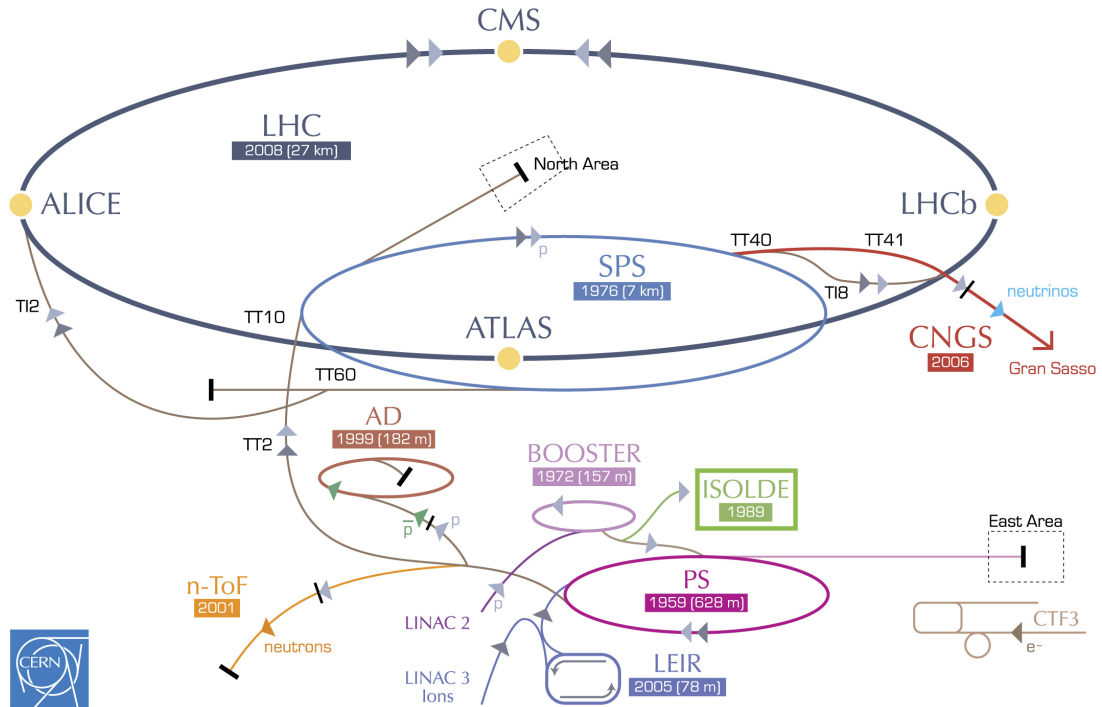


**Figure 3.1:** The CERN accelerator complex, adapted from [29]. ISOLDE, marked with a green box, receives accelerated protons from LINAC 2 and the PS Booster.

produce a target of a radioactive nuclei and to perform experiments due to the short half-life of the involved nucleus<sup>1</sup>. To study these radioactive nuclei, RIBs are accelerated at stable targets.

The beam at the RIB facilities consists of, as the name implies, radioactive isotopes. In contrast to conventional facilities where the target is made out of the isotope of interest, the investigated isotope is the beam accelerated into a target. The velocity of the beam is significant, with  $v/c$  values of a few percent.

One way of obtaining a RIB is to use the Isotope Separator On Line (ISOL) method. There are three main reactions for producing radioactive atoms with the ISOL method; spallation, fragmentation and fission. Nuclear spallation is the process in which light fragments of the target are ejected due to the high-energy impact of the incoming beam. Fragmentation is the splitting of a target compound into smaller particles or unstable ions. In fission, a nucleus is split into two or more nuclei. When applying the ISOL method, two accelerator systems are required. The first accelerator is used to produce the radioactive atoms by spallation, fragmentation or fission of the primary target nuclei. Then, the second accelerator is used to accelerate the RIB atoms into a secondary target [26, 31, 32].

<sup>1</sup>The radioactive isotope  $^{140}\text{Sm}$  has a ground state half-life ( $T_{1/2}$ ) of 14.82 min.

In RIB facilities, the intensity is generally a bit lower compared to stable beam facilities, which is a big challenge. In terms of energy, ISOL facilities operate around the Coulomb barrier, making them suitable for Coulomb excitation and particle transfer reactions.

In the electromagnetic (EM) interaction with the target, the beam gets excited into a higher energy state. When the beam isotopes de-excite, they emit  $\gamma$ -rays, which can be observed to have large Doppler shifts depending on the velocity and angle. Due to the finite solid angle of the detectors, a sizable Doppler broadening can be observed in the  $\gamma$ -rays. When the detection system has high granularity, i.e. that the system consists of many segmented detectors, the Doppler shifts and broadening can be corrected for. If the angle between the recoiling nucleus and the  $\gamma$ -ray can be determined accurately, a Doppler correction can be applied [33], as described in [Section 4.3.9](#).

## 3.2 Experimental setup

### 3.2.1 Beam production

[Figure 3.2](#) shows a sketch of the experimental setup of the  $^{140}\text{Sm}$  Coulomb excitation experiment. Accelerated proton beam bunches from the PSB comes into the ISOLDE facility and collide with a thick production target, the primary target. Two proton beam bunches are separated by 1.2 s. The proton beam has an energy of 1.4 GeV and an intensity up to 2  $\mu\text{A}$  [34, 35]. ISOLDE typically takes 50% [33] of all proton bunches form the PSB, the rest goes to the Large Hadron Collider (LHC) and the other experiments shown in [Figure 3.1](#).

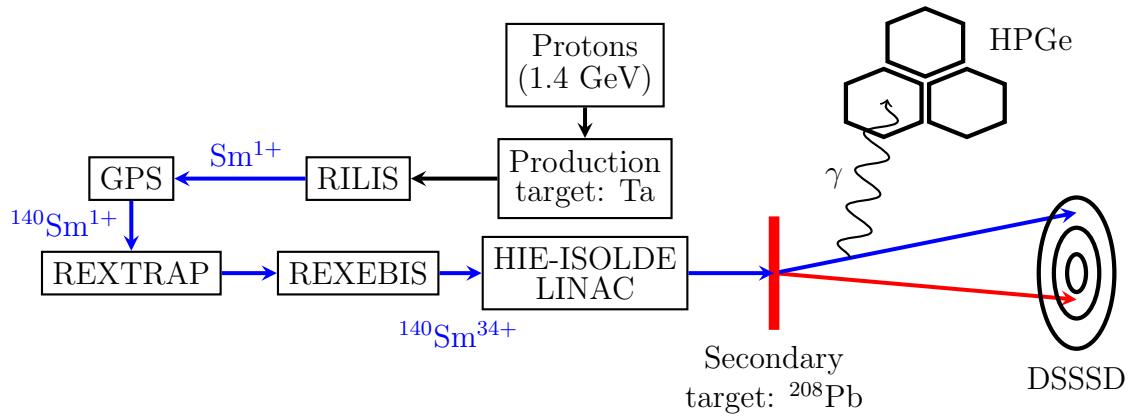


**Figure 3.2:** The Coulomb excitation setup at ISOLDE for the present experiment. Adapted from [13]. See the text for more information.

The production target material is chosen depending on the RIB of interest. If

the requested RIB is neutron-rich, a primary target of uranium ( $^{238}\text{U}$ ) is chosen, and the beam will be produced by fission of the target nuclei. In this experiment, a neutron-deficient RIB was requested, and a primary target of tantalum (Ta,  $Z = 73$ ) was chosen. The production target is selected from a region in the chart of nuclides containing stable nuclei that are heavier than the nucleus of interest. When the proton beam collides with the primary target, the target is smashed into pieces, and radioactive isotopes with proton number up to Ta are produced. In this way, a large range of isotopes are produced.

The remaining challenge is to extract the isotope of interest in order to create a RIB. Before the desired isotope can be obtained, a method of selecting the chemical element of interest have to be used. One approach is to use a method of selective ionization and then a high voltage electrostatic field to extract the ions. Electronic transitions are characteristic for each chemical element. A laser with a precisely tuned wavelength can obtain the photon energy that matches the electronic transition energies in the atom perfectly [36, 37]. Thus we can use one laser to excite an electron to a specific excited electron-state in the atom, a second laser to excite electrons further to another excited electron-state and a third laser to remove the electron entirely. In this way, we only ionize the element required to produce the beam.

The Resonance Ionization Laser Ion Source (RILIS) is based on the method of step-wise (2-3 step) excitation and ionization of an atom. It is an element-selective process which is used to produce ion beams of the desired element [38]. In this experiment, RILIS was used to select samarium (Sm) with atomic number  $Z = 62$ . After RILIS has selected Sm, we have a continuous beam of  $\text{Sm}^{+1}$  ions at an energy of 60 keV [26, 34].

After the ionization of the beam, the next step in the process is to perform a mass separation. The goal of the mass separation is to obtain a beam only containing the isotopes with the desired mass number, and to exclude the contaminants that exits RILIS. By using a set of magnets, the separator purifies the RIB, but in principle, isobaric contaminants may still be present in the beam after the separation. Luckily, the neighboring elements of Sm produces very little surface ionization. Therefore, few contaminants are expected to be present in the beam after the separator. Different sources of beam contaminants are discussed in [Section 3.2.2](#).

At ISOLDE, the beam may hit one of two target stations after RILIS; either the General Purpose Separator (GPS) or the High Resolution Separator (HRS). Both separators feed the beam lines in the experimental hall, but only one separator is active during an experiment. The HRS combine two bending magnets with high mass resolving power, delivering the beam into the main beam line. Even though the HRS have a high mass resolving power,  $M/\Delta M > 5000$ , it is not sufficient resolving power to separate the isobars, which is why RILIS and the GPS was used in the current experiment. The GPS has one bending magnet

and can deliver beams containing isotopes of different mass numbers simultaneously into three beam lines. The two extra beam lines that the GPS can feed, can have an isotope mass difference of  $\pm 13\%$  compared to the main beam line isotope mass [34, 39]. In this experiment the GPS was used to select the isotope of Sm with mass number  $A = 140$ .

Following the GPS, a continuous beam of  $^{140}\text{Sm}$  is obtained. The post-accelerator cannot accept an incoming continuous beam, it can only accelerate bunches. In the Radioactive beam EXperiment TRAP (REXTRAP), the  $^{140}\text{Sm}$  ions are collected in order to release them in bunches that are matched to the time structure of the HIE-ISOLDE LINAC. REXTRAP is a penning trap which tasks are accumulation, bunching and cooling of the RIB [25, 40, 41]. The ions are released in bunches and transferred to the REX Electron Beam Ion Source (REXEgis), see Figure 3.2.

REXEgis is a charge breeder where the RIB obtains a high charge state [42], with a mass-to-charge ( $A/q$ ) ratio typically between 2.5 and 4.5 [43]. In REXEgis, even more electrons of the RIB atoms are removed through the interaction with a high-intensity electron beam. The longer the ions stay in REXEgis, the higher the charge state becomes. The EBIS blasts off more electrons from Sm, which leaves the nucleus in a high charge state, going from  $^{140}\text{Sm}^{+1}$  to  $^{140}\text{Sm}^{+34}$  with  $A/q \approx 4.1$ .

To accelerate the charged ions, i.e. the beam, to high energy, the beam must consist of highly charged ions. Inside REXEgis a distribution of charge states are obtained, but the HIE-ISOLDE LINAC can only accept one charge state. Therefore, only the parts of the RIB containing the correct charge state is accelerated, the remainder of the beam is lost [44–47]. REXEgis releases the beam with a specific energy through another mass separator before guiding the RIB into the HIE-ISOLDE LINAC. The purpose of the second mass separator is to remove residual gas (beam contaminants) from the beam exiting REXEgis [25].

The HIE-ISOLDE LINAC accelerates the beam of  $^{140}\text{Sm}$  with excellent purity to 4.65 MeV/u, or a total energy of 651 MeV, through the beam line. Several magnets bend the beam into the Miniball spectrometer, where the beam hits the secondary target of  $^{208}\text{Pb}$ . The beam particles get excited due to the electromagnetic interaction with the target. As the  $^{140}\text{Sm}$  particles from the beam fly towards the particle detector, they de-excite by emitting  $\gamma$ -rays, which are then detected by the  $\gamma$  detectors. The detector system records information about the angles and energy with a good time resolution. In this way, particle- $\gamma$  coincidences can be reconstructed to obtain Doppler-corrected  $\gamma$ -spectra in order to analyze the Coulomb excitation of  $^{140}\text{Sm}$ .

### 3.2.2 Sources of beam contaminants

To have a successful experiment, the purity of the beam is of great importance. Contaminants in the beam can come from several different sources. A common experimental challenge are contaminants from surface ionization, i.e. atoms that collide with the walls of the ion source. This can be significant, even dominant in some cases. However, surface ionization was not an issue in the present experiment due to the fact that Sm has the lowest ionization potential of the rare earth elements. In any case, the beam contaminants are monitored by periodically switching the laser on and off. Arising from the primary target we may have [33]:

- isobaric contaminants which are inseparable by the mass separator because of the same mass number
- isotopes with an integer multiple of both mass and charge

and from stable isotopes the contaminants can come from:

- buffer gas in REXTRAP (e.g. Ne, Ar)
- residual gas in REXEBIS (e.g. C, O)
- components of REXEBIS (e.g. La from the cathode)

More information on contaminants can be found in [25, 33, 38].

### 3.2.3 The secondary target

For the current experiment, a target consisting of  $^{208}\text{Pb}$  with a thickness of 1.4 mg/cm<sup>2</sup> was chosen. Unfortunately, there was a finger print on the target, implying a contamination (probably carbon and/or oxygen from grease).

It is quite difficult to excite  $^{208}_{82}\text{Pb}_{126}$  as it is a doubly magic nuclei, and it is therefore well suited for the experiment. In that way, transitions from the target will not complicate the  $\gamma$ -ray spectrum. With a target consisting of the highest possible  $Z$  of a stable isotope ( $Z = 82$ ), the excitation probability of  $^{140}\text{Sm}$  is maximized.

$^{208}\text{Pb}$  has no quadrupole deformation. The first excited state is an octupole vibration with an energy of 2615 keV, a half-life of  $T_{1/2} = 16.7$  ps and a spin and parity of  $J^\pi = 3^-$ . Therefore, there is a small probability of observing the first excited state of  $^{208}\text{Pb}$  in the  $\gamma$ -spectrum. The excitation probability for  $^{208}\text{Pb}$  is maximal if the EM interaction is approximately head on, and the ejected target nucleus hits one of the inner particle detector rings.

### 3.2.4 Miniball spectrometer

The Miniball spectrometer consists of a particle detector and a  $\gamma$  detector array. In the Coulomb excitation experiment, a silicon detector was used to determine the energies and angles of scattered particles, and germanium detectors were utilized to measure  $\gamma$ -rays related to the excited states of  $^{140}\text{Sm}$ . The target chamber, containing the  $^{208}\text{Pb}$  target, resembles a small ball, hence the name Miniball. See [Figure 3.3](#) for an overview picture of the Miniball spectrometer.

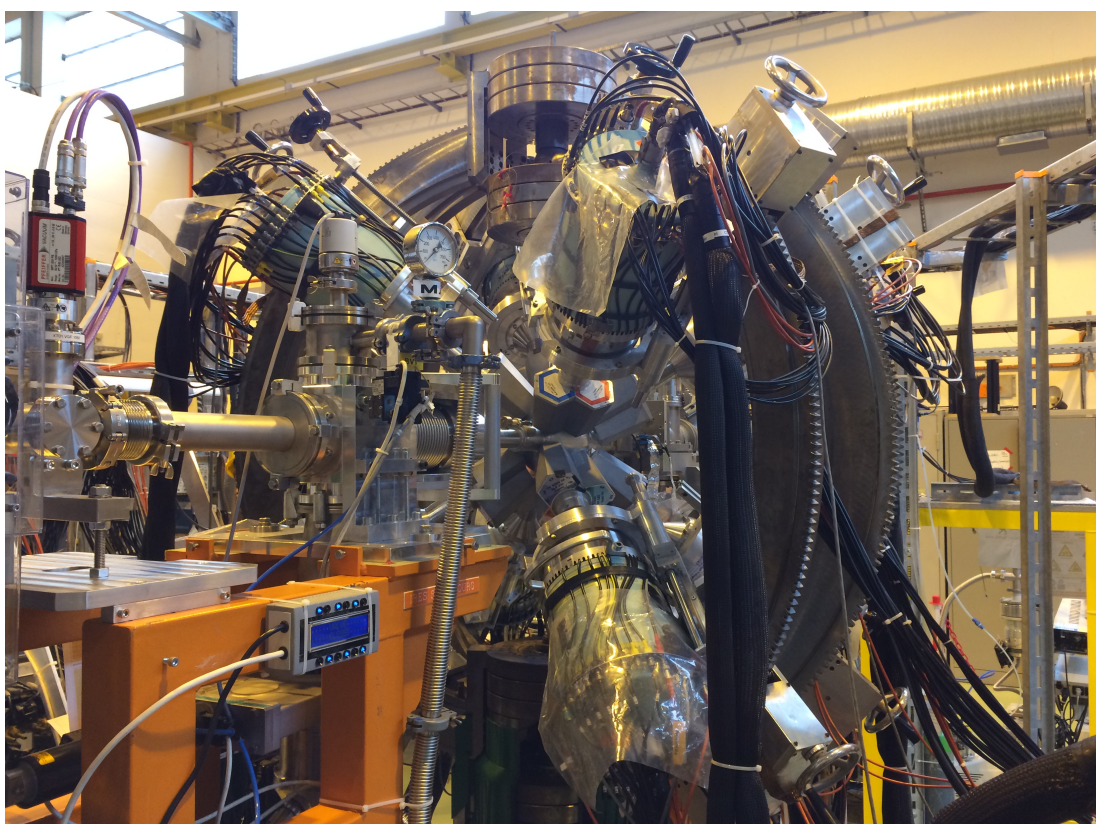


**Figure 3.3:** An overview picture of the Miniball spectrometer. The target chamber is in the middle of the picture, surrounded by the  $\gamma$  detector array.  
Photo by: Trond Wiggo Johansen.

### Target chamber

The target chamber is a hollow sphere made out of a machined out, single piece of aluminium alloy ( $\text{AlMg}_3$ ), with a thin wall and an inner radius of approximately 80 mm. Inside the chamber we find a target wheel and a particle detector. As shown in [Figure 3.4](#), the target wheel can hold up to six different targets. The particle detector can be positioned 25 - 31 mm from the target wheel, limited by the space inside the chamber. Outside of the target chamber, the average distance from each  $\gamma$  detector cluster to the center of the target chamber is approximately 10 cm. The forward and the backward  $\gamma$  detector clusters are placed in a  $45^\circ$  and  $135^\circ$  angle  $\theta$ , respectively, compared to the beam line. In the vertical plane, perpendicular to the beam line, the four  $\gamma$  detector clusters in forward and backward position are placed roughly on a circle with a separation of  $\phi = 90^\circ$  [33].

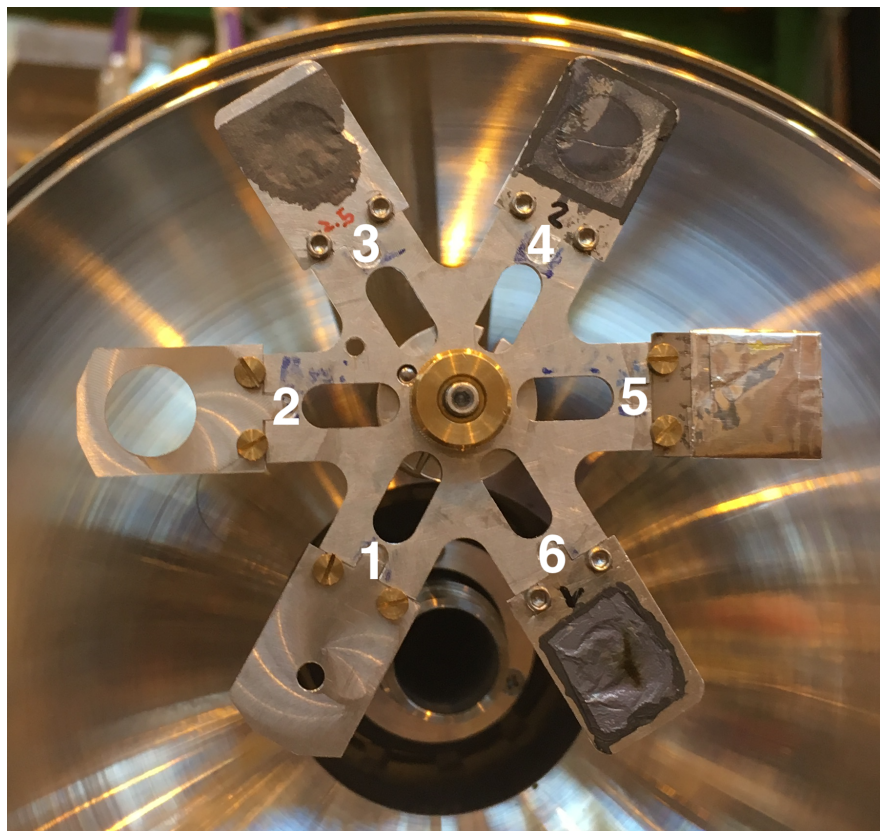


**Figure 3.4:** The target wheel can hold up to six different targets. Position 1 and 2 are holes with a diameter of 3 and 12 mm respectively. They are used for beam tuning. Position 3 and 4 has  $^{208}\text{Pb}$  targets with thickness 2.5 and 0.7 mg/cm<sup>2</sup> respectively. Position 5 has 13 layers of  $^{27}\text{Al}$  foil. Position 6 has the target  $^{208}\text{Pb}$  with thickness 1.4 mg/cm<sup>2</sup>, which was the secondary target used in the present experiment. Photo by: Dr. Liam Gaffney, date: 07.08.2017.

### Particle detector, DSSSD (CD)

To detect the scattered beam and target nuclei, a segmented Double Sided Silicon Strip Detector (DSSSD) composed of four quadrants was used. [Figure 3.5](#) shows a sketch of the front and back of the detector. The DSSSD resembles an audio Compact Disc (CD), and hence it is called the CD. In the front of the CD, one quadrant consists of 16 annular strips (rings) with a pitch of 2 mm, while the back consists of 24 sector (radial) strips with a pitch of 3.5°. The innermost strip has an inner radius of the active area of 9 mm, while the outermost strip has an outer radius of the active area of 40.9 mm. The active area of the detector is the area in which a particle can be detected, the detectable surface.

In total, there are 160 discrete detector elements for all four quadrants, 64 in front and 96 in back. Each quadrant of the CD is independently connected to a Analog to Digital Converter (ADC) and a Time to Digital Converter (TDC). The TDC keeps track of the time of registered particle- $\gamma$  and particle- $\gamma$ - $\gamma$  coincidences. As a result of too few available channels in the ADC, the sector strips in the back are paired up. In consequence, it is effectively 12 strips on the back side of the CD. [Table E.1](#) lists the signal cable wiring of the CD into the ADC.

The whole CD detector has a total area of 5000 mm<sup>2</sup>, where approximately 93% of the detector consists of a detectable surface. In Coulomb excitation experiments the silicon wafer thickness is usually 500  $\mu\text{m}$ . The silicon wafer is the thin slice of semiconductor which can detect the incoming particles. For simplicity the dead layer thickness is usually assumed to be 0.7  $\mu\text{m}$  [33, 48]. [Table 3.1](#) shows some of the specifications of the CD. The distance from the target to the CD was  $27 \pm 1$  mm. In the laboratory (LAB) reference frame the CD covers an angle range between 18.4° and 56.6°. The angles are divided up in rings corresponding to the scattering angles in [Table 3.2](#). An extensive description of the CD can be found in [49].

**Table 3.1:** CD specifications.

	Annular strips (CD Front)	Secular strips (CD Back)
Number of strips	16	24
Inner radius of active area	9.000 mm	-
Outer radius of active area	40.900 mm	-
Strip pitch	2.000 mm	3.5°
Strip width	1.900 mm	3.4°
Strip length	-	31.900 mm
Active angle coverage	81.6°	81.6°
Inner strip distance	-	0.100 mm

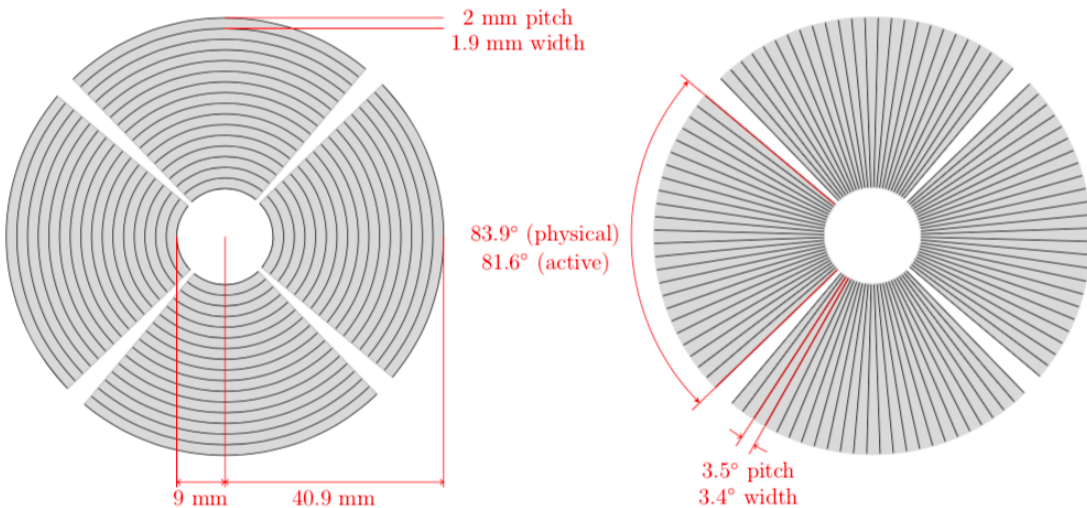


**Figure 3.5:** CD sketch, adapted from [48]. On the left is the front side of the CD. The beam goes into the paper from the perspective of the left drawing. Front (annular) strips are numbered from 0 (outermost) to 15 (innermost). Quadrants are numbered in clockwise direction with respect to the beam direction, which corresponds to: left is 1, up is 2, right is 3 and down is 4. On the right is the back side of the CD. The beam comes out of the paper from the perspective of the right drawing. Back (radial) strips are numbered from 0 to 23 in counter-clockwise direction. Viewed from this perspective, the quadrants are numbered as: right is 1, up is 2, left is 3 and down is 4.

### The high-purity germanium (HPGe) $\gamma$ detectors

In Coulomb excitation experiments, the target chamber is surrounded by the  $\gamma$  detectors as displayed in Figure 3.6. The  $\gamma$ -ray spectrometer consists of a total of 24 six-fold segmented High-Purity Germanium (HPGe) crystals, which are divided into 8 clusters of 3 crystals each. Each crystal is encapsulated and segmented into 6 parts, making a total of 144 segments. Compared to using the whole crystal, a better Doppler correction can be performed when the  $\gamma$  detectors are segmented.

For maximum efficiency, the detectors are placed in a compact geometry around the target chamber [33, 51]. The detector-array can cover a solid angle of about 60% of  $4\pi$ , when the optimum distance between the target chamber and the HPGe clusters is achieved. The average energy resolution at  $E_\gamma = 1.3$  MeV is 2.3 keV [52]. During operation the HPGe clusters needs to be cooled down by liquid nitrogen which is provided by the automated filling system.

Figure 3.7 shows a sketch of one triple-cluster of the HPGe  $\gamma$  detector array, with the corresponding table of all of the clusters positions. From each detector we get seven signals in total for each event, one from the core and six from each segment. This requires 168 channels for data acquisition. The shapes of these

**Table 3.2:** Scattering of  $^{140}\text{Sm}$  on  $^{208}\text{Pb}$  with beam energy 4.65 MeV/u. Calculations are done with the LISE++ [50] kinematics calculator with a reaction from the middle of the target. The LAB and CM frame angles are based on the LAB input angles from  $\theta_b$  and  $\theta_t$ . In (b) there are angles marked with red color. These are overlapping with the CM angles in (a), making a total of 24 unique angles in the CM frame marked in black.

(a) $\theta_b \in [22.0^\circ, 56.7^\circ]$ .			(b) $\theta_t \in [22.0^\circ, 56.7^\circ]$ .		
LAB		CM	LAB		CM
$\theta_b$ [°]	$\theta_t$ [°]	$\theta'_b$ [°]	$\theta_b$ [°]	$\theta_t$ [°]	$\theta'_b$ [°]
22.0	71.7	36.6	40.6	56.7	66.6
26.0	68.4	43.2	42.3	55.3	69.4
29.1	65.9	48.2	44.2	53.9	72.2
32.2	63.4	53.3	46.1	52.4	75.2
35.2	60.9	58.1	48.3	50.7	78.6
37.9	58.8	62.4	50.6	49.0	82.0
40.4	56.8	66.3	53.1	47.1	85.8
42.8	54.9	70.1	56.0	45.0	90.0
45.0	53.2	73.5	59.1	42.8	94.4
47.1	51.6	76.7	62.5	40.4	99.2
49.0	50.2	79.6	66.1	37.9	104.2
50.7	48.9	82.1	70.2	35.2	109.6
52.4	47.6	84.7	75.0	32.2	115.6
53.9	46.5	86.9	80.2	29.1	121.8
55.3	45.5	88.9	85.8	26.0	128.0
56.7	44.5	91.0	93.8	22.0	136.0

signals are analyzed to provide information about the energy and time of the  $\gamma$ -ray, in addition to the detection position within the detector cluster [51].

### 3.3 Data acquisition system

Signals from the CD and the HPGe clusters are read out by the ADC, TDC and Digital Gamma Finder (DGF) modules and sent to a Personal Computer (PC) in the Data AcQuisition (DAQ) room at ISOLDE. The data is then stored in a PC. The ADCs and DGFs record an energy and a time-stamp with 25 ns ticks. It is the multiplicity of the output of the DGFs that is used to generate the  $\gamma$  signal, which in turn is used to make the particle- $\gamma$  coincidence.

The collection of data is done by the MAR<sub>a</sub>BQU [55, 56] DAQ system [33]. It is split in two parts, as presented in Figure 3.8, one front-end part based on the Multi Branch System (MBS) [57] and one back-end part based on the ROOT framework [58]. The front-end takes care of data readout, event building and

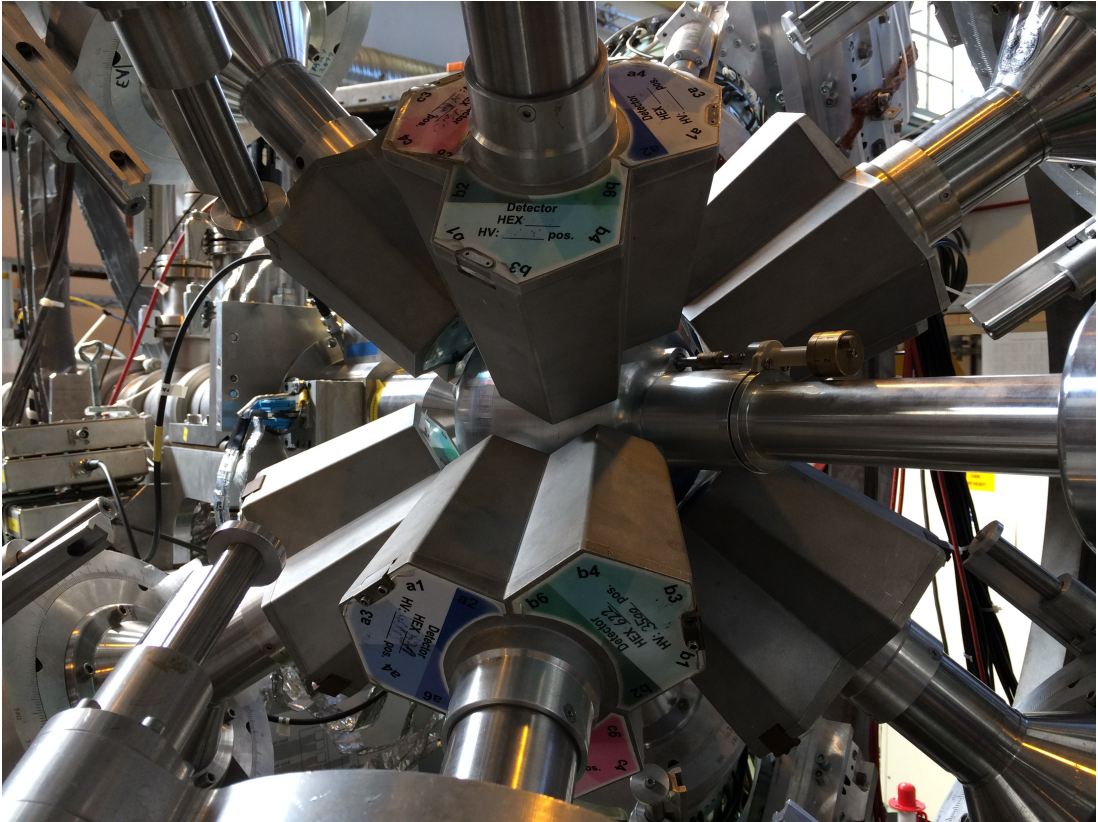


**Figure 3.6:** Close up picture of the Miniball spectrometer. The Miniball target chamber is in the middle, surrounded by the triple-cluster encapsulated  $\gamma$  crystals. The beam line goes through the target chamber.  
Photo by: Trond Wiggo Johansen.

data transportation, while the back-end takes care of the setup, run control, histogramming, data analysis and data storage.

The system can manage high counting rates without much dead time. For a detection system, the dead time is the time after a readout of events where the system is unable to record another event. The ADCs and TDCs can buffer up to 32 events at a time [33]. Essentially, the largest limitation to the DAQ system is pile-up, which is when the detection system starts processing another event before the previous event was finished. The events adds on top of each other, which leads to loss of information from both events.

During an experiment, the ROOT back end is mostly used to inspect the experiment live. As will be detailed in Chapter 4, the offline ROOT analysis is very time consuming, and is largely performed after the experiment. This is the main part of the thesis.

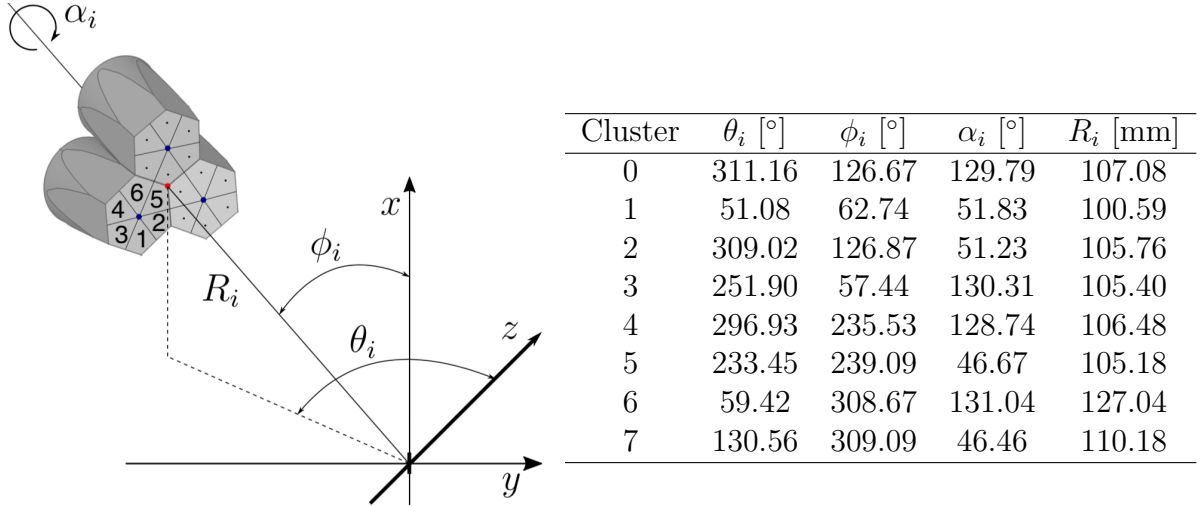


**Figure 3.7:** On the left is a sketch of the HPGe triple-cluster position, adapted from [53]. Each cluster is segmented into 6 parts. The core signal is marked by the blue dots in the middle of each of the three crystals, and the center of the triple-cluster is marked with a red dot. There are four parameters,  $\theta_i$ ,  $\phi_i$ ,  $\alpha_i$  and  $R_i$ , to determine the position of one triple-cluster. The angles,  $\theta_i$  and  $\phi_i$ , are defined from a right-hand polar coordinate system, as displayed by the sketch.  $\alpha_i$  determines the clockwise rotation around the center of the triple-cluster as seen from the target position.  $R_i$  is the distance from the middle of the target chamber to the center of one triple-cluster. In the sketch, the secondary target is positioned in origo and the beam direction goes along the  $z$ -axis [53, 54]. On the right side is a table which contains the HPGe triple-cluster parameters for the present experiment, where  $i$  denotes the cluster number used in the Miniball setup. The geometry is used for the Doppler correction, which is discussed in Section 4.3.9.

## 3.4 Time structure

In Figure 3.9, a schematic of the ISOLDE time structure is displayed. The Miniball data acquisition occurs during two time windows, the "on-beam" and "off-beam" windows. When REXEBIS releases the beam to the HIE-ISOLDE LINAC, a signal to generate the on-beam window is sent. This window, called the "slow extraction mode" was  $800 \mu\text{s}$ , but in 2011 it was extended to 1 ms, as the beam extraction method was improved. All the data are read out after the on-beam window. During a readout, the DAQ becomes dead for a little while, so the next window is triggered when the DAQ is operable again. The off-beam window starts  $60 \mu\text{s}$  after the end of a readout of the on-beam window. This allows the ADCs and TDCs time to start again. The time structure of ISOLDE makes it possible to record data again in the off-beam window, before the next beam bunch is sent from REXEBIS. In the off-beam window, which has the same duration of

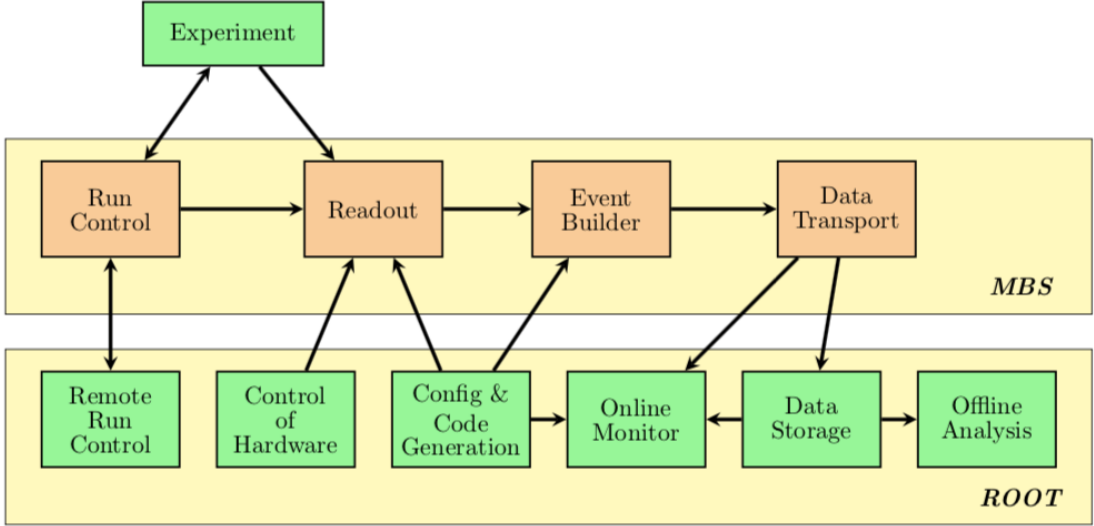


**Figure 3.8:** MAR<sub>a</sub>BQ<sub>U</sub> tasks, adapted from [55].

time as the on-beam window, data recordings of the background is conducted. After the off-beam window closes, a readout of the records is triggered. It is then possible to subtract the off-beam window from the on-beam, obtaining only the beam contribution. The next on-beam window is triggered when the DAQ is operable again. The DAQ system records the signals from each detector segment, which is individually time-stamped. With these records, a full reconstruction of the real events and coincidences are possible [59].

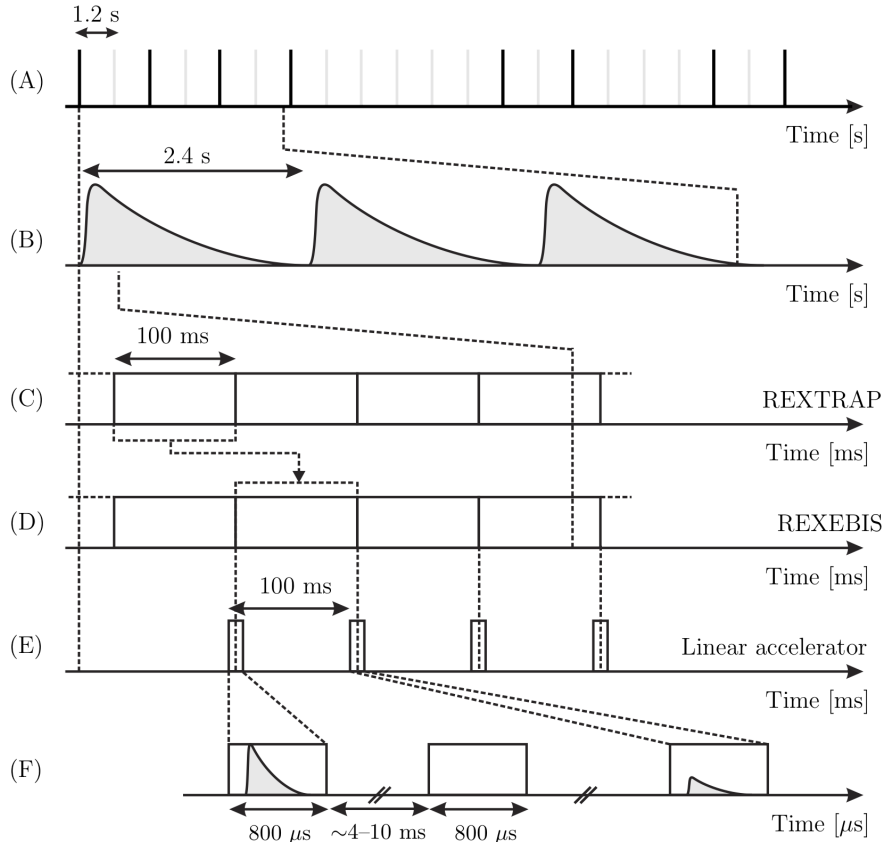


**Figure 3.9:** Schematic of the ISOLDE time structure, from [60]. Figure courtesy of J. van de Walle [61]. (A) The supercycle of proton beam bunches with a width of  $\approx 100 \mu\text{s}$  from the PSB separated by  $1.2 \text{ s}$ . The black vertical lines show an allocation of the bunches which the ISOLDE production target receives, while the others are distributed to other experiments. (B) The release profile of radionuclides from the production target, which is heavily modulated by the PSB cycle. (C+D) REXTRAP and REXEBIS beam bunches, synchronized with (E) the radio frequency (RF) window of the HIE-ISOLDE LINAC. (F) The "on-beam" and "off-beam" time window of  $800 \mu\text{s}$  using the Miniball setup.



# Chapter 4

## Data analysis

*"Not everything that can be counted counts, and not everything that counts can be counted."*

– William Bruce Cameron

In this chapter, the general methods of the calibration and data analysis will be outlined. In addition, the various programs and scripts applied in the detector calibration and data analysis will be introduced. Scripts developed in the present thesis work for the fitting procedures were inspired by scripts written by Ville Virtanen<sup>1</sup> and Dr. Liam Gaffney<sup>2</sup>. The codes have been further developed and heavily re-written in the current work. Presently, the code has only a minor resemblance to the original code. The remaining Python and bash scripts are written and developed by the author. All of the scripts written in C/C++ are dependent on the ROOT 6 framework [58], a C/C++ data analysis framework developed and maintained at CERN.

Information about the computer setup and environment used in this thesis can be found in [Appendix B](#). In the appendix there is also a section containing the relative path of programs, scripts and files. All scripts and programs developed in this work are available in the authors GitHub repository [\[10\]](#).

### 4.1 Data handling

The goal of the data analysis is to obtain Doppler-corrected  $\gamma$ -spectra with various conditions on particles and angles, in order to analyze the Coulomb excitation of  $^{140}\text{Sm}$ . Before the required information can be extracted from the experimental data, all of the particle and  $\gamma$ -ray detectors have to be calibrated. However, the calibration cannot be performed without proper data handling first.

---

<sup>1</sup>Ville Virtanen is a student from University of Jyväskylä.

<sup>2</sup>Dr. Liam Gaffney is a research fellow at ISOLDE, affiliated with Miniball.

As described in [Section 3.3](#), all of the information corresponding to the experiment are handled by the data acquisition system and stored in large data files. Generally speaking, the raw data files from Miniball experiments are formatted in so-called "list mode", where every new line contains the identification, energy and time of one single event<sup>3</sup>. All of the experimental data is stored in `.med`-files, also known as Miniball Event Data, with a standard file naming convention. For example, `140Sm_208Pb_pos6_xyz.med` is the file name for the current experiment. Here  $x$ ,  $y$  and  $z$  are numbers between 0 and 9 which together gives the run number of the data acquisition. The expression `140Sm_208Pb` refers to the beam and secondary target, and `pos6` means that the target wheel uses position 6 for the secondary target, see [Figure 3.4](#). A general rule of the data acquisition is to split the data over several run files to limit the file size, and the probability of corrupt files or data loss.

For Miniball experimental data, the preferred sorting and analysis code is *MiniballCoulexSort* [62]. The code has been developed by several contributors from the Miniball collaboration over the years. Unfortunately, both the procedure and the code is lacking documentation, making it quite time demanding to learn how to run the code and to understand how it works. A goal of this thesis is to document and make the procedure more transparent. Currently is *MiniballCoulexSort* under constant development at CERN-ISOLDE under the management of Dr. Liam Gaffney. The main steps of how to download, install<sup>4</sup> and use *MiniballCoulexSort* is outlined in the `README.md` file in the GitHub repository of Miniball [62]. *MiniballCoulexSort* is written in C/C++ and depends on the ROOT framework.

To get from the raw data to the Doppler-corrected  $\gamma$ -spectra, the data analysis code is divided into a three step procedure which can be summarized by the following subroutines:

1. `MedToRoot` converts the raw data files to ROOT format. This is discussed in [Section 4.2](#).
2. `TreeBuilder` performs the event building by
  - calibrating detectors and applying channel thresholds for the ADCs
  - using particle- $\gamma$  coincidences (correlations), i.e. the code figures out which  $\gamma$  belongs to which particle
  - storing everything in a tree structure for easy access

This is discussed in [Section 4.3.2](#).

---

<sup>3</sup>In truth, the format contains more information, identifying where the particle and  $\gamma$ -ray hit the detectors.

<sup>4</sup>If the `make` step fails, try doing a `make clean` and then `make`. The program might think that it has already been built.

3. CLXAna applies the gates on the particles and performs the Doppler correction. This is discussed in [Section 4.3.7](#).

### 4.1.1 Counting and naming convention for particle detector calibration

When analyzing data using the *MiniballCoulexSort* code, the user have to be aware of the numbering of the CD. The numbering of the CD rings and strips are different in the various programs and scripts. Histograms sorted by `TreeBuilder`, discussed in [Section 4.3.2](#), starts counting from 0 (outermost ring) to 15 (innermost ring) as showed in [Figure 3.5](#). `AQ4Sort`, discussed in [Section 4.3.3](#), starts from 1 (outermost ring) to 16 (innermost ring), shifted by 1 unit compared to the `TreeBuilder` numbering. The simulation program `kinsim3`, discussed in [Section 4.3.1](#), counts from 1 (innermost ring) to 16 (outermost ring), the opposite of `AQ4Sort`. For calibrated spectra, `TreeBuilder` shows the energy in MeV, while `AQ4Sort` shows the energy in keV. To avoid further confusion, this thesis will apply the numbering system of `kinsim3` for the front side of the CD. For the back side of the CD is `TreeBuilder` sorting from 0 to 11 in clockwise direction with respect to the beam direction, while `AQ4Sort` sorts from 1 to 12. This thesis will apply the numbering system of `AQ4Sort` for the back side of the CD. [Table E.2](#) shows the chosen way of counting and the histogram naming from `TreeBuilder` and `AQ4Sort`.

## 4.2 Data conversion

In order to analyze the data with the ROOT framework, the data files have to be converted from the *.med* format produced by MARaBQU into the *.root* format by using the `MedToRoot` program. To effectively convert all of the data files in one run, a bash script called `M2R.sh` was written. It takes in a user defined number of files and converts all the files in one go by using `MedToRoot`. `M2R.sh` takes the element name as command line argument<sup>5</sup> and if no command line arguments are given, the script will print out an usage description. An example of the terminal use including the output for the *140Sm\_208Pb\_pos6\_0xy.med*-file with *xyz = 008* is as follows:

```
$ cd ~/GitHub/MasterThesis/Scripts/sorting
$ ./M2R.sh Sm
opening file ../../Raw_data/Sm/140Sm_208Pb_pos6_008.med ...
EventBuffer::EventBuffer(GlobalSettings *)
Processing event number      0
```

---

<sup>5</sup>`M2R.sh` was intentionally developed to convert *.med*-files from different experiments, so it is fairly simple to expand the script to sort other data sets.

```

Start trigger #14

Processing event number 130000
Stop trigger #15

Unpacked 132802 events:
wrong dgf hit pattern: 0 ( 0.0 %)
wrong adc headers: 0 ( 0.0 %)
# of overflows in adc channels: 599712 (451.6 %)
# of underflows in adc channels: 0 ( 0.0 %)
pattern unit mismatches: 0 ( 0.0 %)

Number of ebis pulses: 66351
Number of t1 pulses: 2211
Number of supercycle pulses: 429
committed 1 243 951 987 bytes to tree tr, 'Tree for on
beam data of Coulex setup@Miniball'
and 15 338 250 bytes to tree bg, 'Tree for on
beam background data of Coulex setup@Miniball',
and 237 454 436 bytes to tree tr, 'Tree for off
beam data of Coulex setup@Miniball',
wrote 97 189 bytes to file ../../Raw_data/Sm
/140Sm_208Pb_pos6_008_OnBeam.root => compressed by a
factor of 12799.3
, 18 362 bytes to file ../../Raw_data/Sm
/140Sm_208Pb_pos6_008_OnBeamBackground.root => compressed
by a factor of 835.3
, 67 934 bytes to file ../../Raw_data/Sm
/140Sm_208Pb_pos6_008_OffBeam.root => compressed by a
factor of 3495.4
and 22 167 bytes to file ../../Raw_data/Sm
/140Sm_208Pb_pos6_008_Scaler.root => compressed by a
factor of 2769.1

```

For each file converted with `MedToRoot`, the program creates four files with the naming convention

- `140Sm_208Pb_pos6_xyz_OnBeam.root`
- `140Sm_208Pb_pos6_xyz_OnBeamBackground.root`
- `140Sm_208Pb_pos6_xyz_OffBeam.root`
- `140Sm_208Pb_pos6_xyz_Scaler.root`

where the file of interest is the first one. The `OnBeam.root`-files are used in the sorting and event building with `TreeBuilder` and/or `AQ4Sort`.

The "on-beam" and "off-beam" files refers to the time structure explained in [Section 3.4](#) which is connected with the beam production explained in [Section 3.2.1](#). The ions are trapped and transferred to the REXEBIS where they

are charge-bred. REXEBIS releases the ions periodically into the HIE-ISOLDE LINAC where they are accelerated. This defines a time structure of the beam and therefore, the events contains a flag from REXEBIS. If the REXEBIS flag is "off", then the event is inserted into the *OffBeam.root*-file. Flag "on" means, in principle, that beam is on, and a more narrow time window with respect to the REXEBIS pulse can be specified. If the flag is "on" and the event is inside the time window, the event is added to the *OnBeam.root*-file. Otherwise, if the REXEBIS flag is "on", but the time stamp is outside the window, the event gets sorted into the *OnBeamBackground.root*-file. The *Scaler.root*-file are for monitoring the count rates in the individual detectors.

### 4.3 Detector calibration

Every detector channel, including its electronics<sup>6</sup> is slightly different from the other channels. It is therefore necessary to calibrate each detector channel in both energy and time. Calibration of the detectors minimize the measurement uncertainty by making sure the detectors are consistent with each other. If the detectors are not properly calibrated, adding spectra from different detectors may cause unwanted effects. For example, the true full energy peak may appear wider if one of the spectra in the sum is shifted in energy compared to the other spectra. By determining the centroids of peaks in every spectrum, and comparing these with theoretical values obtained by simulating the kinematics of the reaction and energy loss, linear calibration coefficients of the detectors can be obtained. In this context, the centroid<sup>7</sup> of the energy peaks refer to the channel of maximum height in the histogram.

Both the particle and  $\gamma$  detectors applied in this experiment are semiconductor detectors. The basic principle of operation is that incoming ionizing radiation<sup>8</sup> creates electron-hole pairs in the semi-conducting material which are then collected by an electric field. The number of electron-hole pairs are assumed to be proportional to the energy of the incoming radiation to the semiconductor [63]. By applying this assumption we obtain a linear correlation between the energy  $E$  of the particle (or  $\gamma$ -ray) and the channel number  $n$  of the ADC (or DGF)

$$E = g \cdot n + a \quad (4.1)$$

where  $a$  is the offset in keV and  $g$  is the gain in keV/ $n$ . The gain  $g$  and the offset  $a$  are the coefficients needed to perform the calibration. From Equation (4.1),

<sup>6</sup>Electronics like pre-amplifiers, ADCs, etc.

<sup>7</sup>Normally, the centroid is only the maximum if the peak is symmetric.

<sup>8</sup>For the CD, the ionizing radiation is the beam or target particles scattered from the reaction, while the ionizing radiation for the HPGe detectors is the high-energy photons ( $\gamma$ ) from de-excitation of the nuclei.

the offset  $a$  can easily be expressed as

$$a = E - g \cdot n \quad (4.2)$$

To find the gain  $g$ , at least two measuring points are needed

$$g = \frac{E_2 - E_1}{n_2 - n_1} \quad (4.3)$$

where the peak energies,  $E$ , are obtained from a simulation of the Coulomb excitation experiment and the channel numbers,  $n$ , are obtained from the raw data of the experiment. To improve the precision of the calibration coefficients, it is desirable to use several data points to obtain  $g$  and  $a$  by a linear regression.

Detectors degrade over time by the high energy impact of particles or  $\gamma$ 's, which implies that the calibration coefficients vary with time. By including more than two centroids, it is possible to check for non-linearities or instabilities in time.

### 4.3.1 Kinematic simulation

To calibrate the data, we need to calculate the expected energy of the centroids of the peaks in the energy spectrum. This was done by simulating the experiment using the program `kinsim3` [64] written by Dr. Liam Gaffney. The purpose of the program is to obtain the kinematics of a Coulomb excitation experiment that utilizes the CD. The simulations calculate the theoretical predictions of the energy distribution of the peaks for each ring in the CD. `kinsim3` returns simulated spectra for the LAB and CM frame, in addition to every annular strip of the CD. The simulated strip spectra of the CD are fitted, their energy centroids are collected and applied in the calibration as explained in [Appendix F](#).

[Appendix F](#) shows the simulated energy for each ring of the CD, in addition to the fitted peaks of each ring. In the fitting of the simulated (synthetic) data from `kinsim3`, a Gaussian function with linear background was applied

$$g(x) = c + sx + Ae^{-\frac{1}{2}\left(\frac{x-\mu}{\sigma}\right)^2} \quad (4.4)$$

where  $x$  is the energy centroid,  $c$  is the background constant,  $s$  is the background slope,  $A$  is the amplitude (Gauss constant),  $\mu$  is the mean (expected energy value) and  $\sigma$  is the standard deviation (Gauss width). [Table 4.1](#) shows the angles of the center of each CD ring in the LAB frame. A general kinematics simulation in the LAB frame and the experimental particle spectra is shown in [Figure 4.8](#).

`kinsim3` takes into account the energy loss in the dead layer of the detector, which is energy and angle dependent. In addition, the simulation considers cross sections for the COULEX reaction. The COULEX probability increases with the

**Table 4.1:** The angles of the center of each CD ring in the LAB frame, with a distance from the target to the CD of 27 mm. Ring 1 is the innermost ring and ring 16 is the outermost ring. The centroid energies originates from a simulation with `kinsim3`.  $E_t$  is the energy of the secondary target particle ( $^{208}\text{Pb}$ ) and  $E_b$  is the energy of the beam particle ( $^{140}\text{Sm}$ ).

Ring number	Center of CD ring		$E_t$ [MeV]	$E_b$ [MeV]
	Distance from beam line [mm]	Angle [°]		
1	10	20.3	484.86	539.89
2	12	24.0	457.53	520.55
3	14	27.4	428.87	499.72
4	16	30.7	398.95	478.33
5	18	33.7	369.54	456.71
6	20	36.5	340.64	435.42
7	22	39.2	313.65	414.84
8	24	41.6	287.31	395.31
9	26	43.9	262.77	376.35
10	28	46.0	240.36	358.75
11	30	48.0	219.53	342.40
12	32	49.8	198.95	326.87
13	34	51.5	182.41	312.31
14	36	53.1	164.55	299.11
15	38	54.6	151.51	286.78
16	40	56.0	139.62	273.80

CM angle.

`kinsim3` was run with the following commands in the terminal to do the simulation

```
$ cd ~/GitHub/Miniball/kinsim
$ root
root [0] .L kinsim3.cc++
root [1] kinsim3(62, 82, 140, 208, 1.4, 4.65, 0.02, 1.0, 0.6,
27, false, 1e6, "../SRIM")
... <showing output from the program>
```

A detailed explanation of the input parameters of `kinsim3` is in Appendix F. In the `kinsim3` run, the energy spread was assumed to be very small. In principle, the excitation energy is expected to be 0.53 MeV for the excitation to the  $2^+$  state. The excitation probability is not known beforehand, unless some rough assumptions are made. Assuming a chance of multi-step excitation at larger angles, an average excitation energy of 1 MeV is quite reasonable. The resolution and the number of events were run with their default values. In this simulation

the angular distribution was flat (uniform), meaning that the Rutherford cross section was not included. Therefore, the relative intensity between the projectile and target peaks are not identical to the experiment. Nonetheless, the simulated energies are realistic enough to be applied in the calibration.

For stopping powers is `kinsim3` applying SRIM-2013 [65] generated files relevant to the reaction with some random spread. SRIM is an abbreviation for Stopping and Range of Ions in Matter, a Monte Carlo code that simulates the interaction of ions with matter. It uses an empirical model, based on systematic measurements. Both electronic and nuclear stopping are modeled, i.e. the interaction of the ions with the electrons in the material and collisions with nuclei are simulated.

### 4.3.2 Online calibration of the particle detector

When a campaign is run at ISOLDE, the staff configures a settings-file and continuously updates it according to new changes in the system setup. In addition the staff makes a calibration file containing the calibration coefficients for the CD and the Miniball  $\gamma$  detector array. For the calibration of the CD, a cocktail beam composed of different isotopes is accelerated into a specific target. An advantage of the cocktail beam is that all peaks are obtained under the same conditions using a thin target, so the peaks are narrower and easier to fit. For the calibration of the  $\gamma$  detectors, usually two  $\gamma$  sources are placed in the target position. The data from these runs are used to create the so-called online calibration file. It contains the calibration coefficients for the ADCs and DGFs in addition to the Miniball geometry. This calibration file is adjusted for each experiment after the campaign period. In this way it is easy to sort and analyze the data during the experiments, to check if the experiment is going well, and to obtain preliminary Doppler-corrected  $\gamma$ -spectra. For IS558, the present experiment, the settings-file *MBSettings2017\_CLX\_IS558.dat* and the calibration file *IS558-online.cal* was created.

Often, the online calibration is quite acceptable and the possible improvement of performing an additional user calibration is minor. In order to examine the online calibration, the histograms of the CD and the  $\gamma$  detectors have to be generated by the `TreeBuilder` code. In this step, information about the timing between particles and  $\gamma$ 's are included, sorting correlated particles and  $\gamma$ -rays into events. Several command line flag options are available for the `TreeBuilder` subroutine. The `-cdpad` flag option must be applied in order to create particle events. If the option is ignored, no particle events are built since there are no particles to correlate with the  $\gamma$ -rays.

For the CD detector, `TreeBuilder` sorts each quadrant for itself. In the front (back) each annular (radial) strip can be viewed as a whole. Therefore, it is not possible to examine each individual pixel of the detector. See [Section 4.3.3](#) for a

detailed discussion of the individual CD pixels.

[Figure 4.3](#) shows the back vs. front energy for one quadrant of the CD for both the online and the user calibration described in the next subsection. An indication of a good calibration is when all detectors lie on a linear diagonal line ( $y = x$ ), implying that the front side and the back side of the CD has detected the same energy. From [Figure 4.3](#), we see that not all detectors lie on the diagonal line, indicating that some of the strips have incorrect calibration coefficients.

### 4.3.3 User calibration of the particle detector

To improve the calibration coefficients, it is possible to redo the calibration and apply energy channel peaks from the current experiment, i.e. perform an user calibration. This is an extensive task due to the large number of detector segments. The total amount of annular strips to calibrate on the front side of the CD is 64, since there is 4 quadrants with 16 rings. On the back side, there is effectively 48 radial strips, 4 quadrants with 12 strips. To fully calibrate the CD, we need all the centroids of the peaks from both sides, 128 centroids (64 annular strips  $\cdot$  2 peaks/stripe) on the front side and 1536 centroids (48 radial strips  $\cdot$  2 peaks/stripe  $\cdot$  16 rings) on the back side. This gives a total of 1664 centroids to extract, which is not a task one would like to do manually. However, it is possible to do a less precise calibration by only applying two peaks in each annular strip, and two peaks in each radial strip, making it in total 224 centroids to extract. Either way, the calibration coefficients of every ADC channel for the CD are obtained by performing a linear regression of the extracted centroids.

Calibrating the back strips of the CD is the same as the front. However, the radial strips cover a large range of scattering angles (the whole radius of the CD). Because the particle energy depends strongly on the scattering angle, the spectra for the radial strips are washed out and show no clear energy (channel) peaks as displayed by [Figure 4.4b](#). For the energy calibration of the sectors on the back it is necessary to sort particle coincidence spectra between front rings and back sectors, i.e. spectra for each pixel of the detector. Since these spectra are only needed for calibration, a separate code named `AQ4Sort` is used to produce them. In addition to the `TreeBuilder` code, the `AQ4Sort` code is found in the Miniball GitHub repository [62]. There exist no documentation or *README* file explaining how to run the `AQ4Sort` subroutine. It can be operated in a similar way to the `TreeBuilder` code, but it does not take any command line flag options. Compared to `TreeBuilder`, `AQ4Sort` sorts the histograms in a different way. By using `AQ4Sort`, every single front strip and back strip combination, i.e. every pixel of the CD, can be viewed. Therefore, it is possible to gate on a peak in the annular (front) ring and align it with a peak in the corresponding radial (back) strip, thus calibrating the particle detector. For the radial strips, it is preferable to at least extract centroids for low, mid and high energies to cover the angular

range of the strip. For example gating on ring 1, 8 and 16.

As mentioned in [Section 4.3](#), minimum two data points are required to obtain the calibration coefficients of [Equation \(4.2\)](#) and [Equation \(4.3\)](#). On the front side of the CD, there are effectively only two measuring points per angle interval. On the back side of the CD there are two peaks per gated annular strip that can be fitted, so per back strip a maximum of 32 measuring points. By utilizing a built in ROOT fitting function, Gaussian or other, the centroids of the peaks for both Sm and Pb can be extracted. On the front side of the CD, [Equation \(4.2\)](#) and [Equation \(4.3\)](#) can be used to calculate the calibration coefficients:

$$g_p = \frac{E_{\text{Sm}} - E_{\text{Pb}}}{n_{\text{Sm}} - n_{\text{Pb}}} \quad a = E_\rho - g_p \cdot n_\rho \quad (4.5)$$

where the  $g_p$  is the gain for the particle,  $a$  is the offset,  $n$  is the channel number and  $\rho$  can be either Sm or Pb. For more than two centroids per strip, as the back side of the CD have, a linear regression method is used to find the best fit of the calibration coefficients. The linear regression method is using least squares of a 1st degree polynomial [66] to fit a line that re-produces the centroid points as best as possible, where the slope corresponds to the gain and the constant term corresponds to the offset.

An ambitious goal of the calibration of the current data set was to make a program that could automatically fit the centroid of the desired energy peaks by means of the ROOT framework. As will be explained in the current section, the task faced several difficulties, and in the end required a great deal of manual labor from the user.

In order to streamline the calibration process a bash script called `Q4S.sh` was written. `Q4S.sh` uses either `TreeBuilder` or `AQ4Sort` to sort large numbers of data files in one go. The `OnBeam.root`-files are loaded into `TreeBuilder` via `Q4S.sh` with the commands

```
$ cd ~/GitHub/MasterThesis/Scripts/sorting
$ ./Q4S.sh Sm user TB
—— TreeBuilder ——
input file(s):
... <shows a list of all input files>
output file: Sm_user-TreeBuilder-2019-06-20.root
calibration file: ../../Miniball-config/IS558-user.cal
WeightPR: 0.75
Particle distribution:
Q0 fired: 12243817
Q1 fired: 12277727
Q2 fired: 11479362
Q3 fired: 10936096
Finished.
```

In the output, there is a line reading WeightPR: 0.75. This parameter is needed when calibrating the  $\gamma$  detectors explained in [Section 4.3.7](#).

[Figure 4.1](#) shows a flowchart of the programs, scripts and files used in the user calibration. The strategy to perform the calibration of the CD is to combine the simulated data from `kinsim3.cc` and the experimental data sorted with `AQ4Sort` in order to obtain the calibration coefficients. `kinsim3` delivers the energy centroids of [Equation \(4.5\)](#), while `AQ4Sort` delivers the channel numbers. These two data sets are then analyzed using ROOT through different functions in the `ParticlePlot.cpp` script. Information about the range of the peaks and guesses of the centroids of  $^{208}\text{Pb}$  and  $^{140}\text{Sm}$  is written into input files applied by `ParticleFit.cpp`. Here, the automatic fitting collects the centroids of both data sets and write them into output files which is used as input by `particle-calibration.py`. This Python script plots the centroids and uses the linear regression method to extract the gain and offset values. The values are written out into separate output files which are used as input in `ADC-generator.py`. This Python script writes the calibration coefficients to the terminal, and from there they are copied and pasted into the calibration file `IS5558-user.cal`. The calibration coefficients given to the calibration file follow the naming convention of `TreeBuilder` in [Table E.2](#). This new calibration file is then used to sort the data once more with `Q4S.sh`, but using `TreeBuilder` this time. To visualize plots after a new calibration, either ROOT or `ParticlePlot.cpp` is used. The gray boxes in [Figure 4.1](#) related to the  $\gamma$ -calibration are discussed in [Section 4.3.7](#).

Several issues arose as the method of the automatic fitting was developed. The biggest complication was discovered when the method was tested on the radial strips of the CD. In essence, the discrepancy between peak shapes are too large to calibrate the radial strips with a simple script. The fitting function can behave very strange given a too small or too big range. Another problem is the complex shape of the peaks. [Figure 4.2a](#) displays a strip that the automatic fitting handles well, while [Figure 4.2b](#) shows an example of a strip that is challenging to fit. In [Figure 4.2a](#), it is fairly easy to determine the centroids of the particle peaks. The shape of the  $^{208}\text{Pb}$  peak in [Figure 4.2b](#) is very irregular and it is difficult to determine the centroid of the peak because of the overlapping contaminant at lower energies. In most cases the peak shapes are not Gaussian. A ROOT built in function of a 4th degree polynomial was tested to fit the complex peak shapes. The predefined ROOT function

$$f(x) = p_0 + p_1 \cdot x + p_2 \cdot x^2 + p_3 \cdot x^3 + p_4 \cdot x^4 \quad (4.6)$$

fits the values of the parameters automatically, given a initial guess by the user. Unfortunately, the 4th degree polynomial did not describe the peak shapes well either. To implement a proper automatic fitting program, one would have to find a function with a negatively-skewed distribution, where most of the data values are concentrated on the right side of the distribution graph.

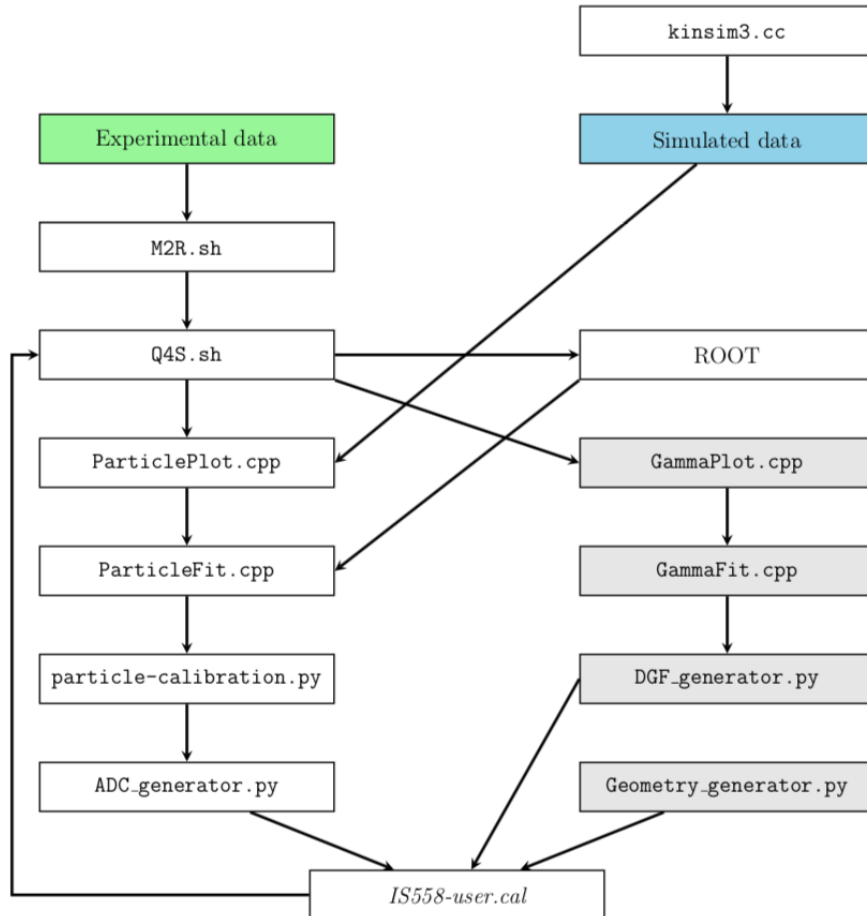


**Figure 4.1:** Flowchart of the programs, scripts and files applied in the user calibration. The relative paths of these programs and scripts are shown in [Table B.2](#).

In logarithmic (log)  $y$ -scale, the data appears to be more Gaussian distributed, while the contrary is not the case in the linear  $y$ -scale. The automatic fitting worked better when a log  $y$ -scale was applied. Unfortunately, as it turned out, the precision of the fit performed in log  $y$ -scale was not satisfactory. One should be careful to inspect the quality of the fit on a linear scale, as it is more difficult to see deviations on a logarithmic scale.

On lower energies, there are problems to properly extract the centroids. To overcome this challenge, additional data obtained during experiment IS553 conducted immediately before the present experiment was applied in the detector calibration. Unfortunately, the attempt including the data from experiment IS553 to improve the calibration was unsuccessful. The quality of the data can be estimated by looking at how well the data lie on the diagonal line when plotting front against back energy. When energy peaks from IS553 was included in the user

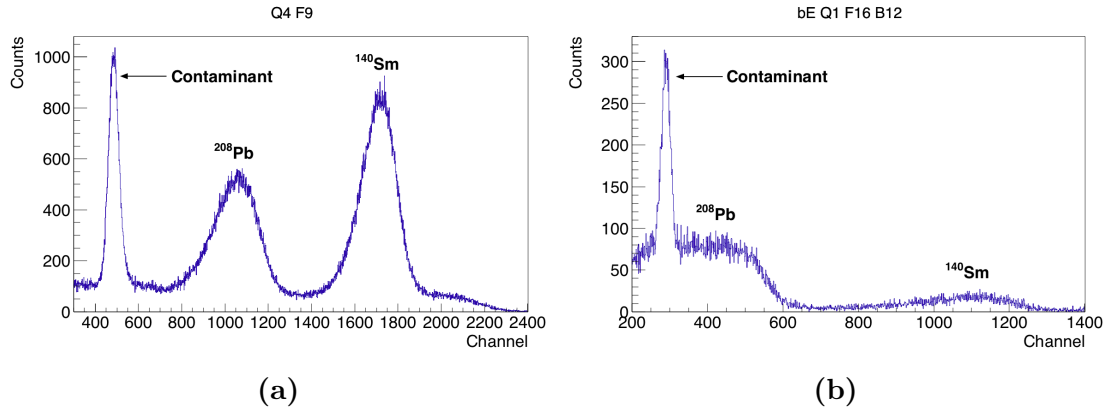


**Figure 4.2:** (a) Front strip number 9 in quadrant 4. (b) Back strip 12, gated on ring 16 (outermost ring) in quadrant 1. See the text for more information.

calibration of the current experiment, the calibration appeared to look worse. Firstly, the diagonal line in the front vs. back energy spectra was not as defined as the online calibration in [Figure 4.3a](#). Secondly, the off-diagonal events seemed to increase, implying that there was an increase in the mismatch of front and back events.

Given the numerous complications of the log scale, the shape of the peaks and the range of the fit, the automatic fitting procedure was discarded altogether. Although plentiful of time was used to develop scripts for the auto-fitting method, we decided to apply the online calibration in the end. As we will see in [Section 4.3.10](#), the main issue of the online calibration was in fact the calibration coefficients of the innermost ring. What will later be described as the user calibration file is essentially the online calibration file without the innermost ring.

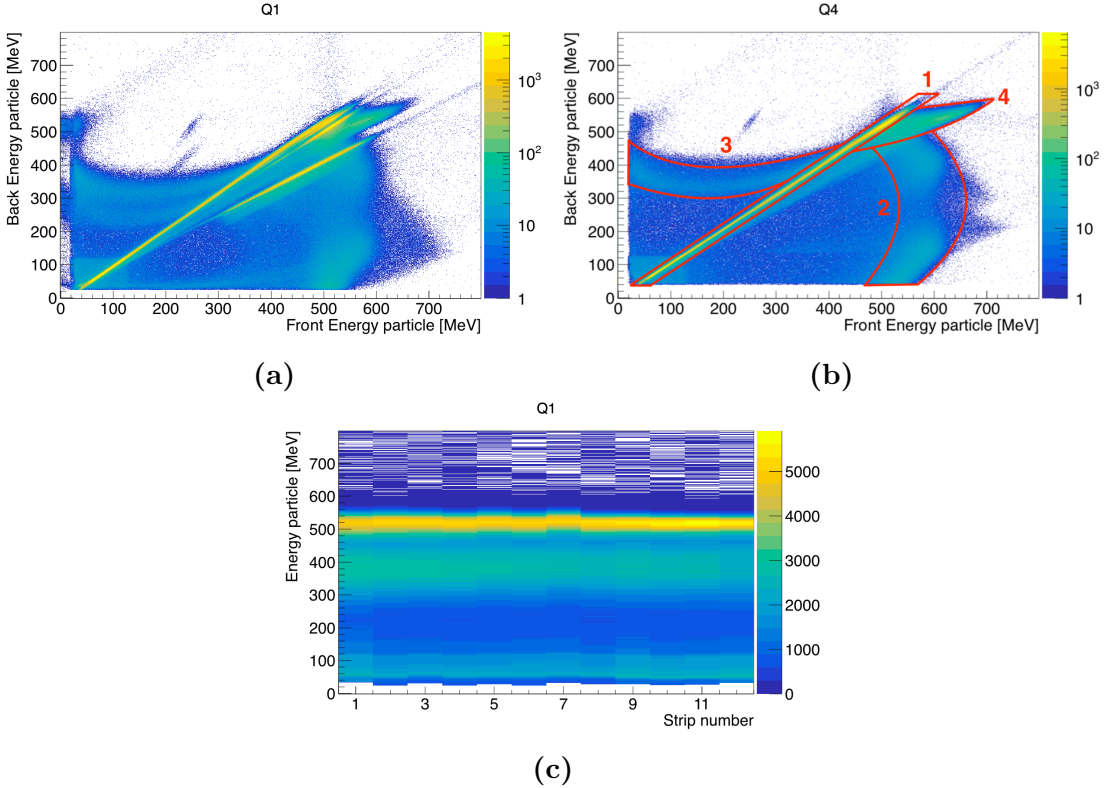


**Figure 4.3:** Back energy vs. front energy for one quadrant of the CD in (a+b). (a) Quadrant 1 using the online calibration. (b) Quadrant 4 using the user calibration. The marked regions are explained in Section 4.3.4 and are similar to figures 39 and 40 in [53]. (c) Quadrant 1 of the back side of the CD using the user calibration. A number of the radial strips have incorrect gains, as they don't lie on the straight line. See the text for more information.

#### 4.3.4 The double peak structure

In several strips of quadrant 1 and 4, we observe a double-peak structure of  $^{140}\text{Sm}$  similar to the peaks displayed in Figure 4.4a. To explain this we have to look at the two-dimensional (2D) spectrum in Figure 4.3b, which can be divided into four parts [53]:

- Region 1: The measured energy at the front and back side of the CD are equal, which indicates that they are linearly correlated.
- Region 2: In these events the detected energy is lower at the back side, while at the front side the energy is artificially increased. One explanation of this is if the energy is detected in one strip on the front side, but is shared between two neighboring strips on the back side. The reduced energy on the back side only occurs when the impact position is close to or inside the dead layer between two strips. The current from the two neighboring

strips can possibly induce an artificially higher energy to the front side of the CD. A similar phenomenon has been observed in segmented HPGe detectors discussed in detail in [67–71]. Another explanation is that there are some charge trapping and charge recombination of the particle-hole pairs. This causes a Pulse-Height Defect (PHD) in the detector signal, which is discussed in detail in [72, 73].

The second Sm-peak at higher energies in Figure 4.4a comes from the projection of the 2D spectrum from Figure 4.3b onto the x-axis.

- Region 3: This area has a similar, but different pattern to region 2. The detected energy is lower at the front side, while it is higher at the back side of the CD. Here, the reduced energy on the front side is likely to originate from charge sharing between neighboring annular strips if the incoming particle hits close to or inside the dead layer. On the back side, the strips are coupled to a positive voltage which protects against the induction of an artificially higher energy by the front side charge sharing. These phenomena are discussed in detail in [74, 75].
- Region 4: This structure originates from the same effects as region 2. These events occur because of the paired up radial strips on the back side of the CD. Because of the connection of two neighboring strips, the charge is split among them and added up to the total charge.

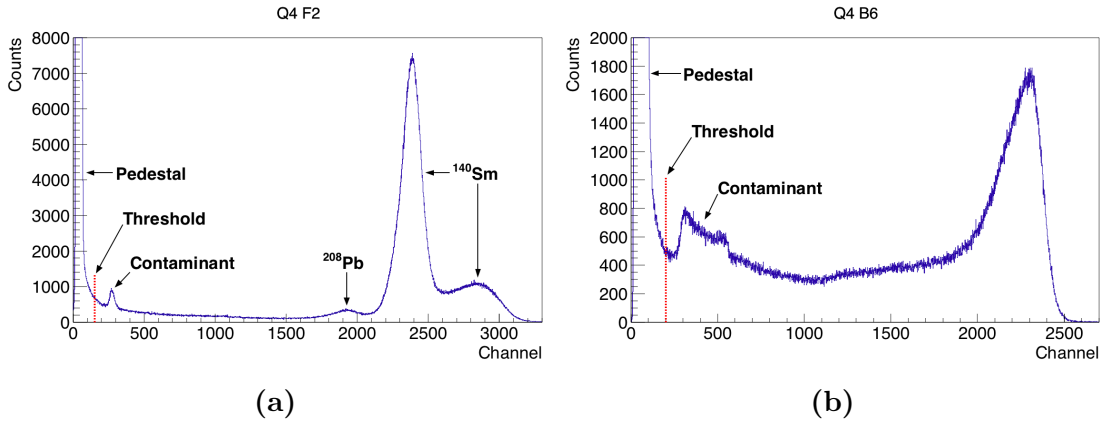


**Figure 4.4:** (a) Front strip number 2 in quadrant 4. At higher energies, there is a double-peak structure of  $^{140}\text{Sm}$ . The second peak of  $^{140}\text{Sm}$  can be explained by region 2 from Figure 4.3b. (b) Back strip number 6 in quadrant 4. See the text for more information.

### 4.3.5 CD threshold

In the CD, the continuum of events at low energy comes from charge sharing between the strips. [Figure 4.4](#) shows the big peak of the charge sharing on the front and back side of the CD. This peak is called the "pedestal". For the very heavy ions, the total amount of charge deposited gets split between neighboring strips of the CD. There is a single common gate for each ADC, containing channels from one CD quadrant. Therefore, when there is an event in one strip of the CD, all channels are read out, but the channels without a real event read a non-zero energy. These are the events in the pedestal. *MiniballCoulexSort* perform a few tricks to try to recover the correct energy and position of the particles. The energy and position of the particles depends on counting the number of strips that fire.

A software threshold is applied to cut away the pedestal. For each ADC channel, the threshold can, and should be set. If no threshold is given in the calibration file, the default threshold is set to channel 100. One should define the threshold for each ADC channel to be above the pedestal peak. If the threshold is set too low, pedestal events are included in the sorting routine, potentially causing harmful issues. If the threshold is too high, several charge-sharing events will be leading to false particle energy. After a correct calibration and threshold is applied, the pedestal will be calibrated out of the physical energy range, meaning it is cut away in the spectra.

The goal is to not include the pedestal, and not to cut away too many continuum events. [Figure 4.4a](#) and [Figure 4.4b](#) shows the software threshold set in the calibration file on the front and back side for one strip on each side. To verify that the implemented threshold is correct, it is very useful to check the so-called "debug" histogram from *TreeBuilder* displayed in [Figure 4.5a](#) and the detected particle events in [Figure 4.8a](#). [Figure 4.5a](#) is a histogram of how many strips of the CD fired per particle. It counts how many particles have lead to  $x$  strips fired on the front side and  $y$  strips fired on the back side. The table in [Figure 4.5b](#) explains the different debug IDs, i.e. lists the  $x$ -axis of [Figure 4.5a](#). The goal of the threshold is to have a lot more counts in CD debug ID 0 compared to ID 3. If we have too many debug ID = 3, then the threshold is too low. If we have a large continuum/background in [Figure 4.8a](#), the thresholds are too high. This way, it is possible to test different values for the threshold and choose the best suited value. The code yields debug ID 20 when no particle can be found, i.e. there is no energy registered in either the front or the back strips. This can only happen when the front energy is below the software threshold set by the user in the calibration file and the back energy is either in a broken strip, or below the software threshold. Charge sharing and noise events will in general also occur below the threshold. Therefore, it is expected that debug ID 20 always have a significant number of counts.

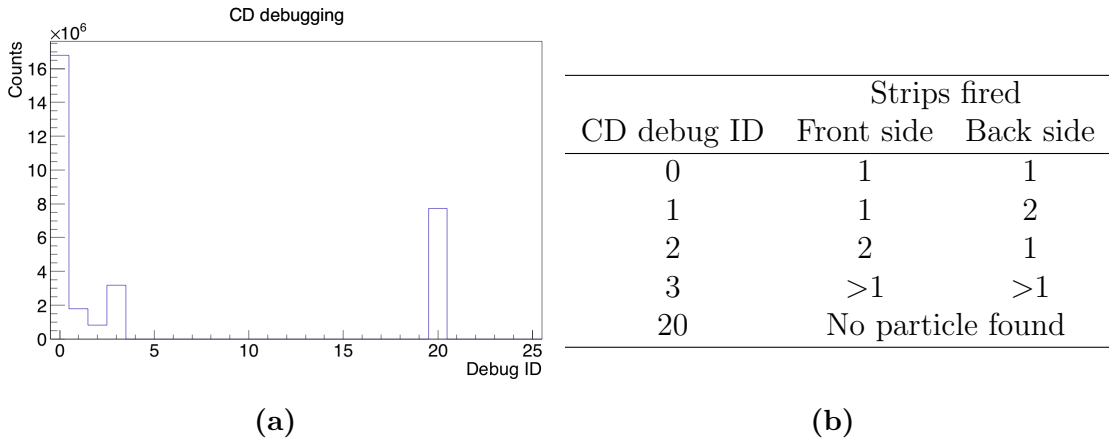


**Figure 4.5:** (a) A histogram of the CD debugging after a user threshold is set. The IDs on the  $x$ -axis are explained by the table in (b). The IDs show the number of strips fired at the front and back side of the CD.

#### 4.3.6 Time calibration

The purpose of the time calibration is to align the time spectra so that a time gate can be set. In this way it is possible to correlate particles and  $\gamma$ -rays. `TreeBuilder` generates time offset histograms. The histograms displays the time difference between a detected particle and  $\gamma$  with 25 ns ticks<sup>9</sup>. Using the `ParticlePlot.cpp` script, the ADC time offset spectra can be extracted by the following commands

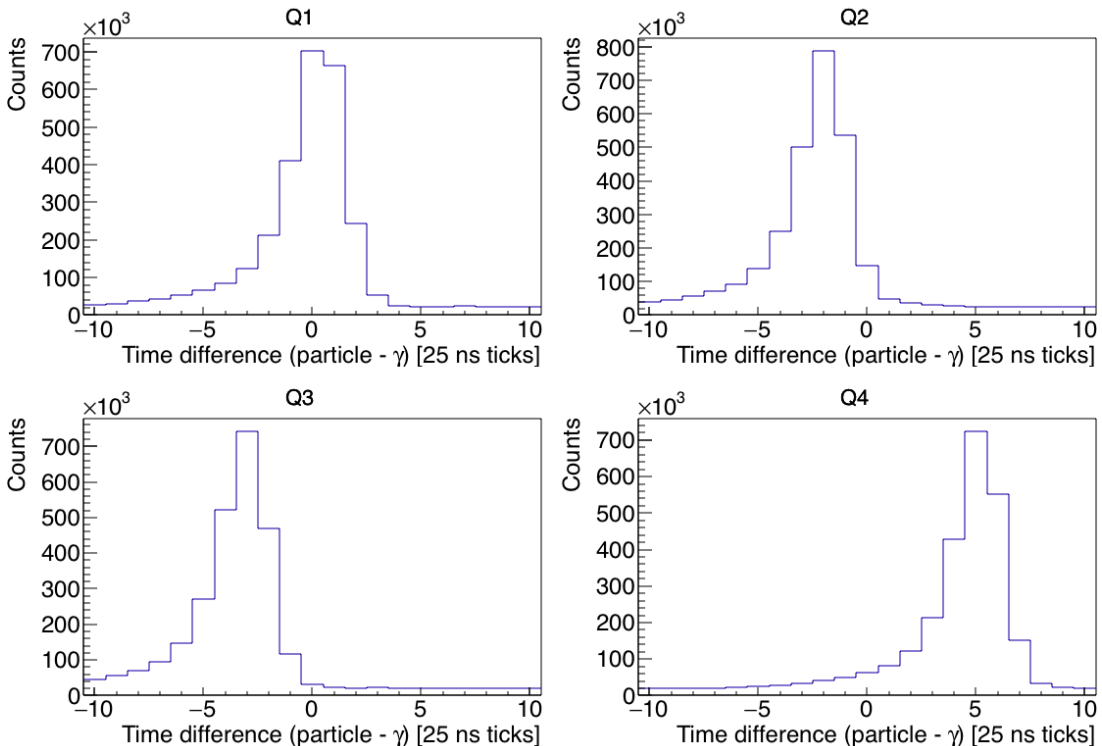
```
$ cd ~/GitHub/MasterThesis/Scripts/plotting
$ root
root [0] .L ParticlePlot.cpp++
root [1] check_ADC_time_offsets("setup.Sm.txt")
```

Figure 4.6 displays the time offsets of all the quadrants of the CD. Here, the time offset values are defined as the  $x$ -value of the maximum peak height. The peak values, i.e. the time offsets, may change depending on the amount of data sorted. Therefore, it is wise to double check the time offsets when more data is added to the `.root`-file. After the peak values have been collected, they should be written into the calibration file together with the updated threshold. Then, the `Q4S.sh` script with `TreeBuilder` should be re-run to implement the changes in the calibration file. The time offsets utilized in this experiment was the following

---

<sup>9</sup>In computers, the system time represents the passage of time. The system time is measured as counting the number of ticks since a starting date. Clock ticks generally refer to the system clock, which runs at a certain frequency, typically in Ghz. This means that there are billions of clock ticks (or cycles) per second. 25 ns ticks refers to one tick per 25 ns, meaning the ADC has a system clock or a CPU running at 40 Mhz.

```
# ADC time offsets (ticks)
adc_0.TimeOffset: 0
adc_1.TimeOffset: -2
adc_2.TimeOffset: -3
adc_3.TimeOffset: 5
```



**Figure 4.6:** ADC time offsets for the four quadrants of the CD. See the text for more information.

### 4.3.7 Calibration of the $\gamma$ detectors

During the setup of the experiment, a hardware and software calibration of the gamma detectors was performed by the ISOLDE staff, as stated in [Section 4.3.2](#). The gains and offsets of each DGF were provided in such a way that the online analysis is more straightforward. In addition, it is easier to monitor the data on-line. However, the  $\gamma$  detectors have non-linear properties, and the offsets and gains may drift over time, calling for a proper calibration. Therefore, a calibration run using  $^{133}\text{Ba}$  and  $^{152}\text{Eu}$  was performed at the end of the experiment. The  $^{133}\text{Ba}$  and  $^{152}\text{Eu}$  sources were placed in the target position simultaneously, back to back. With the data set from the source run, it is possible to verify the quality of the online calibration, and if needed, perform a second calibration. In addition, the

data from the calibration run can be used to determine the relative efficiency of the Miniball spectrometer.

To investigate the gamma calibration, all of the 144 gamma detector segments from the source run was plotted on top of each other, as displayed in [Figure 4.7](#). The alignment of the segments is excellent, i.e. there is no need to improve the gamma calibration. Even if the resolution had been improved by 0.1 keV by applying the source data, once the Doppler broadening gets into play, it makes no difference. Therefore, the online calibration was applied in the present thesis work, similar to the particle calibration.

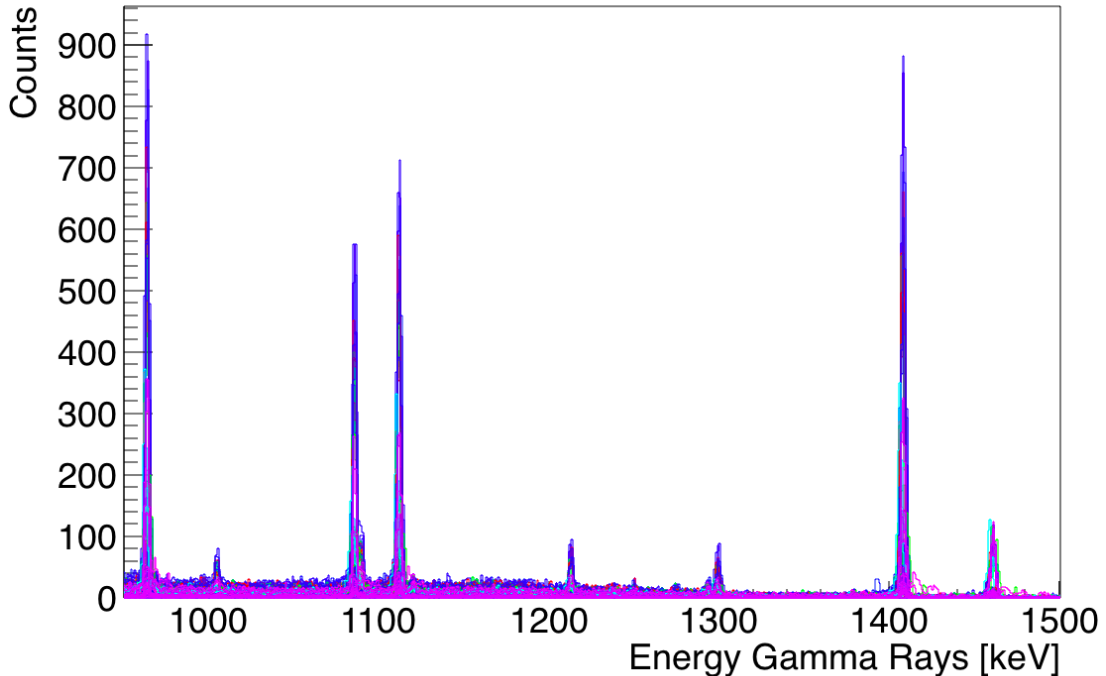


**Figure 4.7:** Comparison of all 144  $\gamma$  detector segments from the source run with  $^{133}\text{Ba}$  and  $^{152}\text{Eu}$ . Each of the 8 clusters are displayed with a different color.

The original thesis project included the calibration of the  $\gamma$  detectors by means of an automatic fitting procedure. For reasons explained in [Section 4.3.3](#), the fitting procedure was abandoned. Nonetheless, the expected program flow including the automatic fitting will be outlined in the following.

In the calibration run, there are many  $\gamma$  lines for both Eu and Ba. Therefore, many data points can be applied in the calibration. The fit can either be linear or quadratic, depending on the detector specification. The online calibration is designed in such a way that the calibration of the  $\gamma$  detectors is quite acceptable

in a certain energy range. Detectors are usually not linear, but a linear approximation is often a good fit for the energy range we choose calibration points from. If a more precise calibration is desired, we can choose a quadratic fit. A simple linear calibration, with only two centroids can be performed similarly to the particle detector calibration. From [Equation \(4.2\)](#) and [Equation \(4.3\)](#) we have

$$g_\gamma = \frac{E_{\text{Eu}} - E_{\text{Ba}}}{n_{\text{Eu}} - n_{\text{Ba}}} \quad a = E_\Gamma - g_\gamma \cdot n_\Gamma \quad (4.7)$$

where  $\Gamma$  can be peaks from either Eu or Ba.

The gray boxes in [Figure 4.1](#) emphasizes the program flow of the  $\gamma$  detector calibration. The idea is to use the `Q4S.sh` script to sort the experimental data with `TreeBuilder`. Then, the  $\gamma$  histograms are analyzed by means of ROOT using the `GammaPlot.cpp` script. Histograms used for  $\gamma$  detector calibration sorted by `TreeBuilder` use the naming convention `E_gam_seg_c_d_s`, where  $c \in [0, 7]$  is the cluster number,  $d \in [0, 2]$  is the detector number and  $s \in [0, 6]$  is the segment number. The core signal is  $s = 0$  as displayed in [Figure 3.7](#).

To perform the fitting, `GammaFit.cpp` would require the energy centroids as input. This script was never written, but the general idea is similar to the particle calibration. Currently, the Python scripts `DGF_generator.py` and `Geometry_generator.py` reproduces the calibration coefficients and geometry parameters from the online calibration. These scripts need to be modified if a second, improved calibration is performed. The final output of the  $\gamma$  calibration would then have been pasted into the calibration file `IS558-user.cal`. After the calibration coefficients and the geometry parameters are added to the calibration file, the `TreeBuilder` program have to be re-run, utilizing the updated calibration file.

### 4.3.8 $\gamma$ sorting

After the completion of the calibration file, the next step is to run `CLXAna`. `CLXAna` sorts the  $\gamma$  spectra, makes a kinematic reconstruction to get the angle of the particles, and applies the Doppler correction in order to get the Doppler-corrected  $\gamma$ -spectra to analyze the Coulomb excitation of  $^{140}\text{Sm}$ . The theory of the Doppler correction is explained in [Section 4.3.9](#).

There are three methods of sorting the events from Miniball in `CLXAna`; singles, add-back and reject. When applying the singles method, every  $\gamma$ -ray entering a detector is counted as an event. There are no assumptions of Compton scattering in this kind of sorting. This implies that some of the events counted as true events are in fact scattered  $\gamma$ 's corresponding to a different energy.

The timing resolution cannot distinguish true  $\gamma$ - $\gamma$  events from Compton scattering events. When utilizing the add-back method, events occurring in neighboring detectors in the same cluster within a 100 ns time window are added together

as a single event. The energies of the events that occurred in the separate segments are summed, and the segment with the highest energy is assumed to be the position of the incident  $\gamma$ -ray. An advantage of the add-back method is that the full energy of a single  $\gamma$ -ray, which has undergone a Compton scattering process, can be reconstructed to increase the efficiency. A disadvantage of the method is the uncertainty in the assumptions of the addition of several events into a single event. The add-back method can cause an increase in the intensity of  $\gamma$ -ray sum peaks. When utilizing the add-back method, in some cases two individual  $\gamma$ -rays are added together, making the sum peak energy higher. Thus no correction is performed when separate  $\gamma$ -rays are added together in the detector [33, 60].

When applying the reject method for the sorting, all events occurring in neighboring detectors in the same cluster within a 100 ns time window is excluded as an event. The total statistics will therefore be smaller when the reject method is applied. If the amount of total statistics is large, it is possible, or perhaps even an advantage to apply the reject method, as it will give a higher probability of getting the true full energy peaks of the detected  $\gamma$ -rays.

**CLXAna** has to be run twice in order to complete the sorting correctly. In the first run, every input parameter except the graphical cuts have to be provided. [Figure 4.8a](#) shows the cuts of the beam and target for the detected particle events. These graphical cuts are used in the Doppler correction of the  $\gamma$ -rays. [Appendix C](#) goes through the details of how the graphical cuts are obtained. When the graphical cut file is made, the second run of **CLXAna** can be completed. In order to not copy and paste all commands into the command line, a script named **Coulex.sh** was made to sort the data with **CLXAna**. It uses the configuration file *config-IS558.dat* and the graphical cut file *outputfile.root*. In addition, it takes one command line flag, specifying the sorting method:

```
'-s' (singles)
'-a' (addback)
'-r' (reject)
```

If no command line flag is given, the singles method is used by default. An example of running the script and the output given by **CLXAna** is shown below

```
$ ./Coulex.sh -s
____ Coulex: singles ____
Input parameters:
Zb = 62
Ab = 140
Zt = 82
At = 208
Eb = 4650 keV/u
Ex = 531 keV
thick = 1.4 mg/cm2
depth = 0.7 mg/cm2
```

```

cddist = 27 mm
cdoffset = 242.6 degrees
deadlayer = 0.0007 mm
contaminant = -1 mg/cm2
spededist = 23.6 mm
bg_frac = -0.75
srim = /Users/trondwj/GitHub/MasterThesis/SRIM
cutfile = ../../Sorted_data/outputfile.root:Bcut:Tcut
Begin g_clx loop.
Info in <TCanvas::Print>: pdf file /Users/trondwj/GitHub/
    MasterThesis/SRIM/140Sm_208Pb.pdf has been created
Info in <TCanvas::Print>: pdf file /Users/trondwj/GitHub/
    MasterThesis/SRIM/208Pb_208Pb.pdf has been created
Info in <TCanvas::Print>: pdf file /Users/trondwj/GitHub/
    MasterThesis/SRIM/140Sm_Si.pdf has been created
Info in <TCanvas::Print>: pdf file /Users/trondwj/GitHub/
    MasterThesis/SRIM/208Pb_Si.pdf has been created
Initialising histograms...
Looping over events...
Warning in <TClass::Init>: no dictionary for class trevts is
    available
1-particle events = 89020258%
Finished.

```

A detailed explanation of the input parameters is provided in [Appendix C](#).

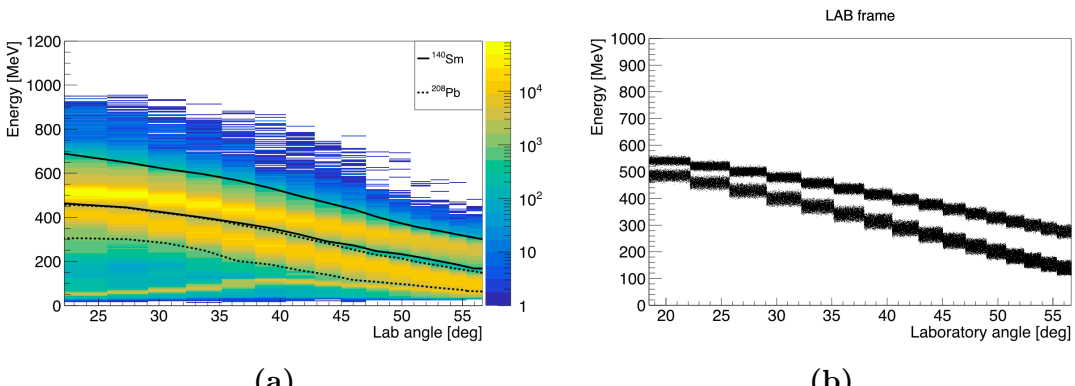


**Figure 4.8:** Detected and simulated particle events of <sup>140</sup>Sm on <sup>208</sup>Pb at 4.65 MeV/u in the LAB frame. Smaller angles corresponds to the inner rings and larger angles to the outer rings. **(a)** The data enclosed by the solid upper and dotted lower lines are the detected particle events of Sm and Pb, respectively. At smaller angles it is difficult to separate the lower solid line from the upper dotted line, but this is visible at larger angles. Underneath and outside the Pb area, the contaminant is displayed in yellow. **(b)** The simulated kinematics, where the upper curve corresponds to Sm events and the lower curve corresponds to Pb events.

### 4.3.9 Doppler correction

The scattered beam particles travel with a significant velocity. When the particles de-excite, they emit  $\gamma$ -rays which can be observed to have large Doppler shifts. To get the correct  $\gamma$  energies, a Doppler correction must be performed. As explained in the previous section, this correction is performed by the `CLXAna` code.

In order to perform the Doppler correction, the angles of the interaction points in the Miniball frame of reference has to be known. [Figure 3.7](#) shows a sketch of the Miniball cluster geometry and the associated table gives the angles and distance of the different clusters. The parameters  $\theta$ ,  $\phi$  and  $R$  describes the position of the central axis of the detector clusters, while  $\alpha$  describes the orientation about the axis of the cluster. All these parameters are required to calculate the position of the segments or the position of a point determined by the pulse-shape analysis, and have to be added to the calibration file. The interaction point is determined either from the segment with the largest energy or using a pulse-shape analysis. These geometrical calculations are built into `MiniballCoulexSort`.

Because of the significant velocity of the scattered particles, the emitted  $\gamma$ -rays from the particle de-excitation has a Doppler shifted  $\gamma$  energy given by

$$E_\gamma = \frac{E'_\gamma}{\gamma(1 - \beta \cos \theta)} \quad (4.8)$$

where  $E_\gamma$  is the  $\gamma$  energy detected in the LAB frame,  $E'_\gamma$  is the  $\gamma$  energy in the nucleus' frame of reference. The Lorentz factor is given by  $\gamma = 1/\sqrt{1 - \beta^2}$ , where  $\beta = \frac{v}{c}$ ,  $v$  is the nucleus' velocity and  $c$  is the speed of light.  $\theta$  is the angle of the emitted  $\gamma$ -ray with respect to the nucleus' direction of motion. Since both the CD and the HPGe array are segmented, the emission angle  $\theta$  of the  $\gamma$ -ray can be calculated by

$$\cos \theta = \sin \theta_p \sin \theta_\gamma \cos(\phi_p - \phi_\gamma) + \cos \theta_p \cos \theta_\gamma \quad (4.9)$$

where  $(\theta_p, \phi_p)$  and  $(\theta_\gamma, \phi_\gamma)$  are the detection angles of the particle and  $\gamma$ -ray, respectively,  $(\theta_p, \theta_\gamma)$  are the angles with respect to the beam axis and  $(\phi_p, \phi_\gamma)$  are the azimuthal angles [33, 76]. The Doppler correction factor is found by combining [Equation \(4.8\)](#) and [Equation \(4.9\)](#) into

$$\frac{E'_\gamma}{E_\gamma} = \gamma(1 - \beta(\sin \theta_p \sin \theta_\gamma \cos(\phi_p - \phi_\gamma) + \cos \theta_p \cos \theta_\gamma)) \quad (4.10)$$

In [Figure 4.9](#), the detector core ID vs. Doppler corrected  $\gamma$ -ray energy is displayed. The straight horizontal lines indicate that the Doppler correction is excellent. For every core ID, the full energy peak is visible at equivalent energy. If

any systematic deviations existed in the particle calibration, they would be visible as irregularities in [Figure 4.9](#) due to the dependence of the particle velocity and angle. It can be noticed that core ID 15 has fewer counts compared to the other IDs and ID 20 is excluded, see the next section.

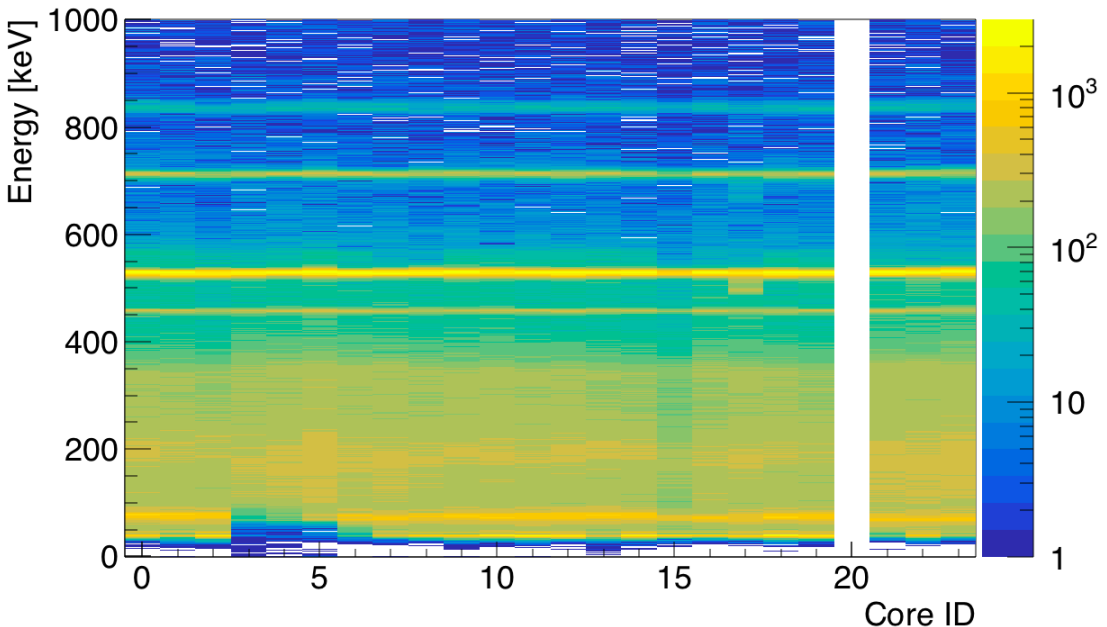


**Figure 4.9:** The core ID vs. Doppler corrected  $\gamma$ -ray energy obtained by running CLXAna. Core ID 20 is removed, see [Section 4.3.10](#).

### 4.3.10 Broken detector segments

Si detectors are known to obtain deficiencies when they are old due to the bombardment of the particles from several experiments. In fact, the CD was scheduled to be replaced after our experiment. As a result of the kinematics of the setup, the innermost ring of the CD is the most vulnerable as it receives the highest energy impact. As presented in [Figure 4.10a](#), it is not possible to separate the beam and target peaks of ring number 1. For this reason, all counts obtained in ring number 1 was removed entirely from the data set. This was very unfortunate since the innermost ring collected the most statistics.

As [Figure 4.3b](#) shows, the calibration of the CD was improved by removing the innermost ring. The most visible lines in [Figure 4.3a](#) that did not fit the diagonal  $y = x$  vanished in [Figure 4.3b](#), implying the problem was in fact caused by the coefficients of ring 1.

On the back side of the CD, one pixel had an abnormal behavior compared to the other back strips in the same quadrant. Presented in [Figure 4.10b](#), radial strip 1 (B1) gated on annular strip 16 in quadrant 4 showed a lot more counts than all of the other strips of the outermost ring combined, notably around channel 800. Additionally, the shape of B1 is deviating significantly from the other strips. However, compared to all the other pixels in general, the number of counts of pixel F16B1 is low, as it is in the outermost region of the CD.

In addition, there were several other incidents where B1 presented an irregular behavior, though not as striking as the case discussed above. It is not possible to exclude only one pixel from the data set. Given the satisfactory calibration displayed in [Figure 4.3b](#) we decided to keep strip B1 in the data set.

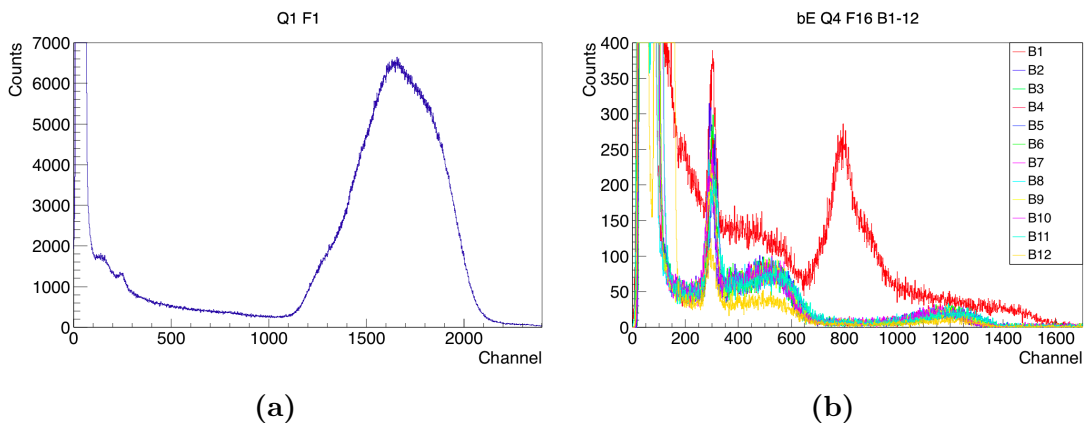


**Figure 4.10:** Broken detector strips in the CD. (a) Ring 1 of quadrant 1. It is impossible to separate the peaks of  $^{208}\text{Pb}$  and  $^{140}\text{Sm}$ . (b) CD back strip 1 gated on front ring 16 (outermost ring) of quadrant 4. B1 displays a small peak around channel 800, while none of the other strips indicate any structure in this region.

From earlier experiments, the ISOLDE staff had observed a few broken detector segments of the  $\gamma$  detector. In [Figure 4.9](#), core ID 20 was removed due to a broken segment. In addition, Core ID 15 displays fewer counts than the neighboring detectors. This is due to a crosstalk issue involving a dead segment in detector 18A (cluster 5, core 0, segment 1 and 2). Crosstalk is the phenomenon where a signal transmitted from one channel creates an undesired effect in another channel. Due to the known crosstalk issue of core ID 15, the CLXAna code have been adapted to reject problematic events, naturally leading to fewer counts in core ID 15.

In order to exclude a detector segment, the gain and offset is simply set to -1, or the gain is set to 0 and the offset to -1. It causes the energy calibration to become negative, and the faulty detector segment falls out of the scope. As explained above, this was only done for ring 1 of the CD.



# Chapter 5

## Experimental results and discussion

*"In physics, you don't have to go around making trouble for yourself – nature does it for you."*

– Frank Wilczek

In the present experiment (IS558), a beam of  $^{140}\text{Sm}$  ions were accelerated into a  $^{208}\text{Pb}$  target at 4.65 MeV/u. Given the direction and energy (velocity) of the scattered particle and the direction of the  $\gamma$ -ray, a Doppler correction was performed under the assumption that the  $\gamma$ -ray was emitted from the projectile. In Figure 5.1a, the total  $\gamma$ -ray spectrum corresponding to the CM scattering angles between  $36.6^\circ$  and  $136.0^\circ$ , Doppler corrected for the projectile, is displayed. The two data sorting methods, singles and add-back, are emphasized by the blue and red colors, respectively. When the add-back method is utilized, the efficiency for high-energy  $\gamma$ -rays is enhanced, i.e. the clarity of the peaks are improved.

The black arrows, except the first one, in Figure 5.1a corresponds to the  $\gamma$  transitions in  $^{140}\text{Sm}$ , while the green arrows corresponds to the sum of  $\gamma$  transitions in a cascade. In the current experiment, excited states up to the  $8^+$  state at 2970 keV were populated. The constituents of the ground state band, the  $\gamma$  transitions of  $8_1^+ \rightarrow 6_1^+$  (888 keV),  $6_1^+ \rightarrow 4_1^+$  (836 keV),  $4_1^+ \rightarrow 2_1^+$  (715 keV) and  $2_1^+ \rightarrow 0_1^+$  (531 keV), are observed in Figure 5.1a. At very low energy, indicated by the first black arrow below the Compton continuum, a peak of  $^{208}\text{Pb}$  x-rays is visible. When the beam passes through the target, there is a possibility of removing electrons, which produces x-rays when the electron holes are filled.

As a comparison, the total  $\gamma$ -ray singles spectrum from the IS495 experiment at ISOLDE in 2012, is displayed in Figure 5.1b. In the IS495 experiment, a beam of  $^{140}\text{Sm}$  ions were accelerated into a  $^{94}\text{Mo}$  target at 2.85 MeV/u. Three excited states of  $^{140}\text{Sm}$  were populated, the first (531 keV) and second (990 keV) excited  $2^+$  states, in addition to the first  $4^+$  (1246 keV) state.

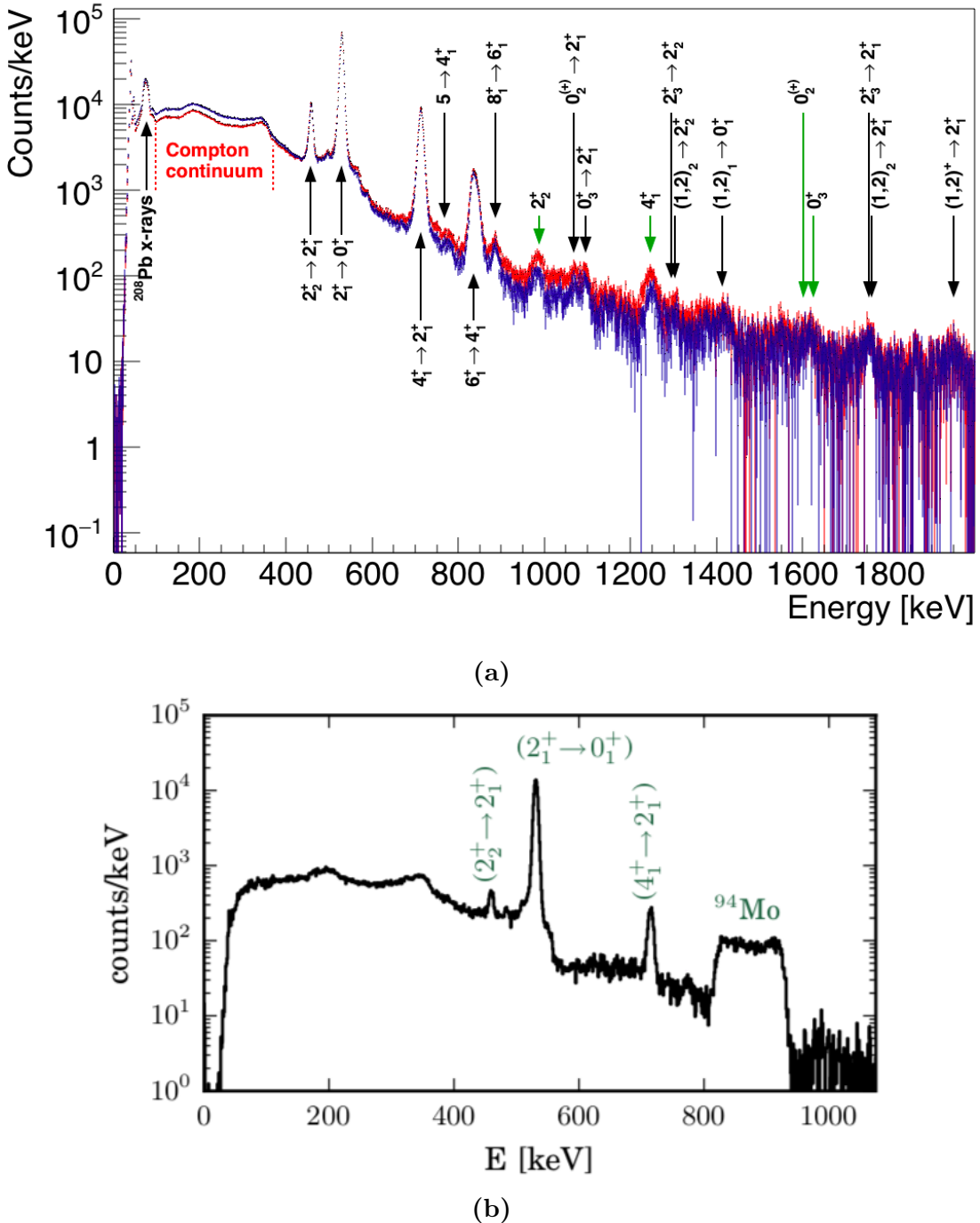


**Figure 5.1:** Background subtracted  $\gamma$  spectrum, Doppler corrected according to the velocity of the scattered projectile (the beam). **(a)**  $^{140}\text{Sm}$  on  $^{208}\text{Pb}$  at 4.65 MeV/u from the COULEX experiment analyzed in the present work, performed in 2017. The blue (red)  $\gamma$  spectrum corresponds to sorting with singles (add-back) in CLXAna. **(b)**  $^{140}\text{Sm}$  on  $^{94}\text{Mo}$  at 2.85 MeV/u from the COULEX experiment performed in 2012 at CERN-ISOLDE [13]. See the text for more information.

The number of peaks in [Figure 5.1a](#) is larger than the number of peaks in [Figure 5.1b](#). For the present experiment, the higher  $Z$  of the  $^{208}\text{Pb}$  target and the higher beam energy contribute to a higher excitation probability of  $^{140}\text{Sm}$ , as explained in [Chapter 1](#). Therefore, a higher excitation energy and a higher spin states are reached in the present work, compared to the previous experiment (IS495). The probability of a multi-step excitation is increased by the experimental conditions in the present work. The increased probability of a multi-step excitation can be observed from the relative intensity of two-step transitions. For instance, the relative intensity of the 460 keV ( $2_2^+ \rightarrow 2_1^+$ ) peak to the 531 keV ( $2_1^+ \rightarrow 0_1^+$ ) peak, in [Figure 5.1a](#) is larger than the relative intensity of the corresponding peaks in [Figure 5.1b](#). Similarly, the relative intensity of the 715 keV ( $4_1^+ \rightarrow 2_1^+$ ) peak to the 531 keV ( $2_1^+ \rightarrow 0_1^+$ ) peak is larger in the IS558 experiment, compared to the IS495 experiment.

All the known  $\gamma$  transitions up to the  $8^+$  state at 2970 keV in  $^{140}\text{Sm}$  are listed in [Table 5.1](#). The far right column in [Table 5.1](#) indicates which  $\gamma$  transitions are visible in [Figure 5.1a](#). Many of the known transitions, but not all, are visible in [Figure 5.1a](#), and there are various reasons for this. First, if the energy of a  $\gamma$  transition is below 400 keV, it will be swallowed by the Compton continuum. Second, the excitation probability for a number of the states are low, and thereby the states are not populated in the present experiment. Third, there might be states with a low transition intensity leading to very few counts in the spectrum, especially at high  $\gamma$ -ray energy. The level scheme of  $^{140}\text{Sm}$  in [Figure 5.2](#) displays all the  $\gamma$  transitions listed in [Table 5.1](#).

The green arrows in [Figure 5.1a](#) corresponds to energy states in [Figure 5.2](#). The energy of the green arrows is a combination of two  $\gamma$  transitions, i.e. the sum of the transition energies. For the very strong transitions, there is a certain chance that two  $\gamma$ -rays hit the same detector within the narrow time window. Consequently, we observe a peak at the energy corresponding to the sum of the two  $\gamma$ -ray energies. This effect is enhanced when the add-back method is utilized, because in this case it is sufficient that two  $\gamma$ -rays hit the same cluster, as opposed to the same crystal, to end up in the sum peak.

The 990 keV and 1599 keV states in  $^{140}\text{Sm}$  transition down to the  $2_1^+$  state with a  $\gamma$ -ray energy of 460 keV and 1068 keV, respectively. The spin and parity of the 990 keV state was originally assumed to be  $0^+$ , and  $2^+$  for the 1599 keV state [77]. An experiment conducted at the Heavy Ion Laboratory (HIL) at the University of Warsaw corrected the spin values of the 990 keV and 1599 keV states in  $^{140}\text{Sm}$  to be  $2^+$  and  $0^{(+)}$ , respectively [78, 79]. Because E2 and M3 transitions have the same angular distributions, the HIL experiment could not determine the parity. Magnetic excitations are strongly suppressed in Coulomb excitation experiments, it is extremely unlikely to populate a  $0^-$  state from a  $2^+$  state. The fact that the  $0_2^{(+)}$  state was populated in the present experiment, already reveal that the parity of the state must be positive, i.e.  $\pi = +$ , which

implies that the spin and parity of the 1599 keV state is  $I^\pi = 0_2^+$ .

**Table 5.1:** Known  $\gamma$  transitions in  $^{140}\text{Sm}$  based on [13, 80].  $E$  refers to the energy,  $J^\pi$  is the spin and parity and  $\sigma\lambda$  is the multipolarity.  $I_\gamma$  is the relative  $\gamma$  intensity for transitions depopulating a given state, where the strongest transition is normalized to intensity 100. The column "Visible in  $\gamma$  spectrum" describes if it is possible to see the transition in Figure 5.1a.

Initial level			$\gamma$ transition			Final level			Visible in
E [keV]	$J^\pi$	$T_{1/2}$	$E_\gamma$ [keV]	$I_\gamma$	$\sigma\lambda$	E [keV]	$J^\pi$	$\gamma$ spectrum	
0.0	$0^+$	14.82 m							
530.68	$2^+$	6.10 ps	530.7	100	$E2$	0.0	$0^+$	Yes	
990.37	$2^+$	7.7 ps	459.9	100	$E2(+M1)$	530.68	$2^+$	Yes	
1245.83	$4^+$	1.00 ps	715.0	100	$E2$	530.68	$2^+$	Yes	
1420.31	(1, 2)		1420.3	100		0.0	$0^+$	Yes	
1598.79	$0^{(+)}$		352.4	3.6		1245.83	$4^+$	No	
			608.6	17.3		990.37	$2^+$	No	
			1068.0	100	$E2$	530.68	$2^+$	Yes	
1628.39	$0^+$		1097.7	100		530.68	$2^+$	Yes	
1932.89	(0, 1, 2)		1402.2	100		530.68	$2^+$	No	
2014.7	5		768.8	100		1245.83	$4^+$	Yes	
2081.91	$6^+$		836.1	100		1245.83	$4^+$	Yes	
2283.89	$2^+$		685.1	47		1598.79	$0^+$	No	
			1293.6	63		990.37	$2^+$	Yes	
			1752.8	100		530.68	$2^+$	Yes	
			2283.9	26		0.0	$0^+$	No	
			1299.4	75		990.37	$2^+$	Yes	
2289.64	(1, 2)		1758.7	100		530.68	$2^+$	Yes	
			2289.1	50		0.0	$0^+$	No	
			311.7	100		2014.7	5	No	
2482.06	(1, 2) <sup>+</sup>		882.7	10		1598.79	$0^+$	No	
			1491.3	100		990.37	$2^+$	No	
			1952.0	67		530.68	$2^+$	Yes	
2595.6	(0, 1, 2)		2064.9	100		530.68	$2^+$	No	
2959.3	(6, 7, 8)		632.9	100		2326.4	7	No	
2969.5	$8^+$		887.6	100		2081.91	$6^+$	Yes	

A typical indication for shape coexistence is  $0^+$  states at low energy. In  $^{140}\text{Sm}$ , there is an indication of two  $0^+$  states around 1.6 MeV. The  $0_2^+$  (1599 keV) and  $0_3^+$  (1628 keV) states can tell us about the shape of the nucleus, in addition to if there is any shape coexistence in  $^{140}\text{Sm}$ . One objective of this experiment is to clarify the structure of these  $0^+$  states.

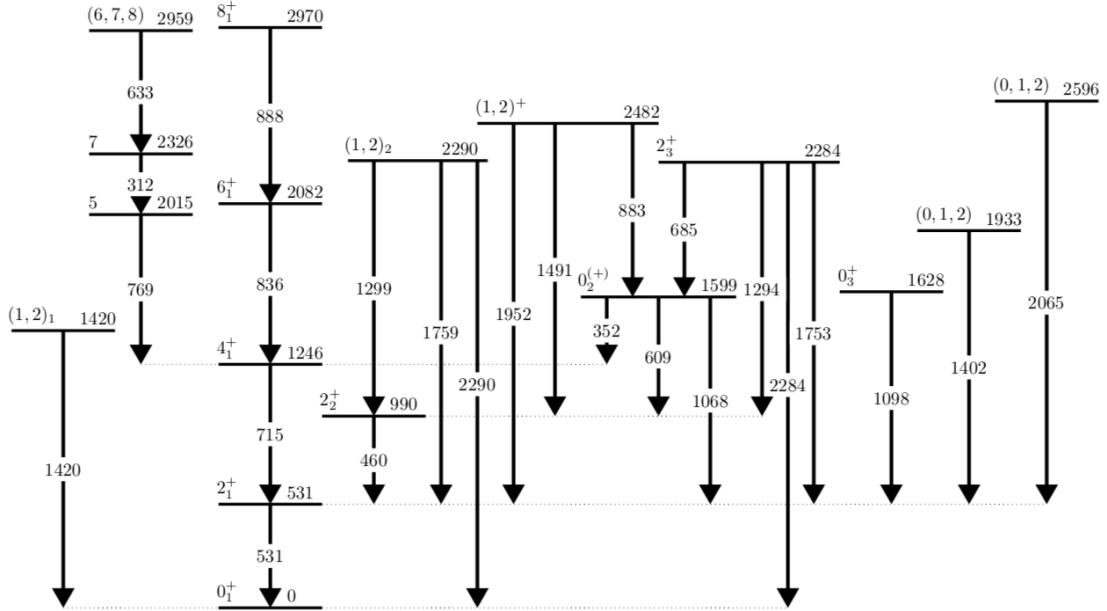


**Figure 5.2:** Level scheme for  $^{140}\text{Sm}$  based on the previous knowledge from [13, 80]. The energies for the levels and transitions are in keV and are rounded to the nearest integer. See the text for more information.

The peak of the 1420 keV ( $(1, 2)_1 \rightarrow 0_1^+$ ) transition is quite broad. This peak might contain the 1402 keV ( $(0, 1, 2) \rightarrow 2_1^+$ ) transition from 1933 keV, at the left side of the rightmost transition in Figure 5.2. Further, the peak at the energy of 1952 keV is similarly broad, and may contain the sum-peak of the 1933 keV level as well.

In addition to the transitions visible in the  $\gamma$  spectrum in Figure 5.1a, a transition from an unknown  $3^+$  state is expected. This unknown state should predominantly decay into the  $2_2^+$  state [79, 81]. The  $3^+$  state is proposed to be a member of the  $\gamma$ -vibrational band, which is expected to be built on the  $2_2^+$  state. Theory predicts that the  $3^+$  state should lie around 1944 keV. In the spectrum of Figure 5.1a, there is no obvious candidate for a transition from the proposed  $3^+$  state. However, the width of the  $6_1^+ \rightarrow 4_1^+$  transition at 836 keV is slightly wider than the other transitions.  $\gamma$ - $\gamma$  coincidences can be used to investigate if the peak at 836 keV is composed of more than one transition. Figure 5.3 presents a coincidence spectra of gates on the left and right flank of the 836 keV peak. When gating on the left flank of the peak, the spectrum shows coincidences with the transitions of the ground-state band, as expected for a coincidence spectrum with the  $6_1^+ \rightarrow 4_1^+$  transition. When gating on the right-hand flank of the peak, however, clear coincidences with the 460 keV ( $2_2^+ \rightarrow 2_1^+$ ) transition appear. These coincidence relationships are confirmed when gating on the 715 keV ( $4_1^+ \rightarrow 2_1^+$ ) and the 460 keV ( $2_2^+ \rightarrow 2_1^+$ ) transitions, respectively. The coincidence spectra

show two peaks that are clearly shifted in energy, with the  $6_1^+ \rightarrow 4_1^+$  transition at the known energy of 836 keV, and a new, previously unobserved transition at 844 keV. The new transition places the candidate for the  $3^+$  state at 1834 keV, 110 keV below the predicted theoretical energy. We cannot expect to observe a transition down to the ground state from 1834 keV, since it would have been a M3 transition, i.e. the transition is very improbable due to the high magnetic multipolarity.

The intensity of the new 844 keV transition is relatively strong, which makes the transition an excellent candidate for the predicted  $3_1^+ \rightarrow 2_2^+$  transition, and a possible member of the  $\gamma$ -vibrational band. If verified, the new state will, without doubt, help clarify the role of triaxiality in  $^{140}\text{Sm}$ .

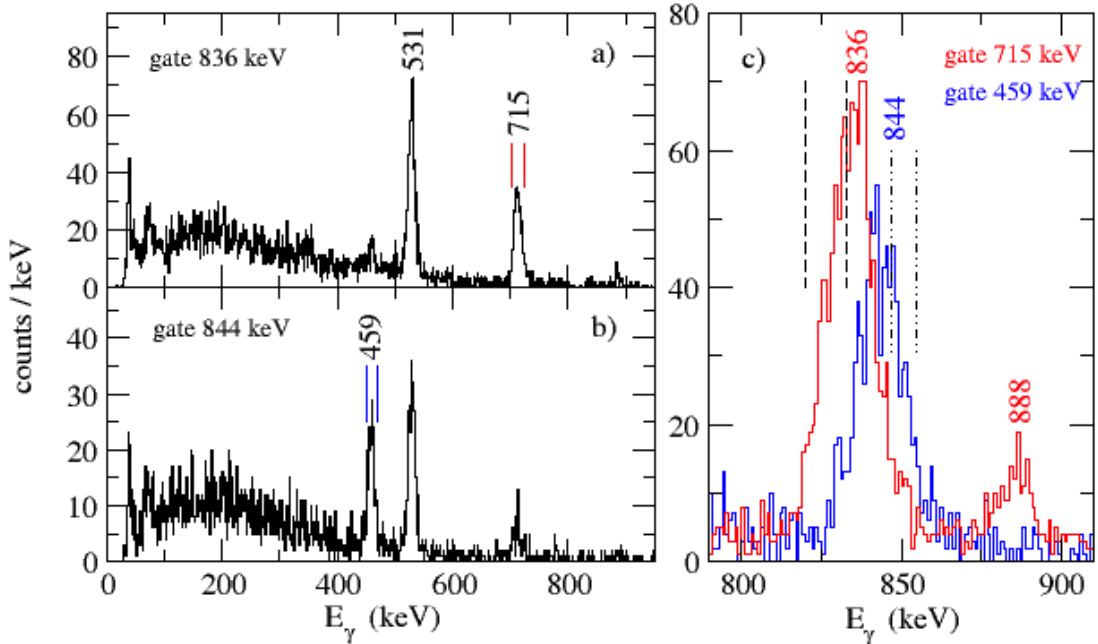


**Figure 5.3:** (a) A gate on the left flank of the broad peak at 836 keV, showing coincidences with the 715 keV ( $4_1^+ \rightarrow 2_1^+$ ) and 531 keV ( $2_1^+ \rightarrow 0_1^+$ ) transitions. (b) Gate on the right flank of the 836 keV peak, showing coincidences with the 460 keV ( $2_2^+ \rightarrow 2_1^+$ ) and 531 keV ( $2_1^+ \rightarrow 0_1^+$ ) transitions. (c) In red, a gate on the 715 keV ( $4_1^+ \rightarrow 2_1^+$ ) transition, showing the 836 keV ( $6_1^+ \rightarrow 4_1^+$ ) and 888 keV ( $8_1^+ \rightarrow 6_1^+$ ) transitions. In blue, a gate on the 460 keV ( $2_2^+ \rightarrow 2_1^+$ ) transition, showing a new transition at 844 keV, presumably from the  $3^+$  state belonging to the  $\gamma$ -vibrational band.

A low-lying  $2_2^+$  state, as the 990 keV state in  $^{140}\text{Sm}$ , is a sign of triaxiality which can either be static or dynamic [81]. From the energy of the  $2_2^+$  state and the  $B(E2; 2_2^+ \rightarrow 2_1^+)$  value it is not possible to determine if the triaxial deformation is static or dynamic, but information related to the newly observed  $3_1^+$  state can help the decision.

The peak at 1860 keV in [Figure 5.1a](#), may prove to be a new state or transition. None of the  $\gamma$  cascades in [Figure 5.2](#) add up to this energy level or transition energy. Therefore, it is difficult to conclude on which state the peak at 1860 keV decays to.  $\gamma$ - $\gamma$  coincidences in future work must be utilized to determine where this transition originates from.

[Figure 5.4](#) displays the  $\gamma$ - $\gamma$  matrix, Doppler corrected according to  $^{140}\text{Sm}$ . The diagonal lines below 600 keV, originates from the Compton continuum. Here, we observe clearly defined vertical and horizontal lines corresponding to the constituents of the ground state band of  $^{140}\text{Sm}$ . Summarized, we recognize the energies of the ground state band at 531 keV, 715 keV, 836 keV and 888 keV. The line at 888 keV is quite thin, while the line at 836 keV is quite broad. In a more detailed analysis, the  $\gamma$ - $\gamma$  matrix can be utilized to search for new transitions to extend the level scheme of  $^{140}\text{Sm}$ .

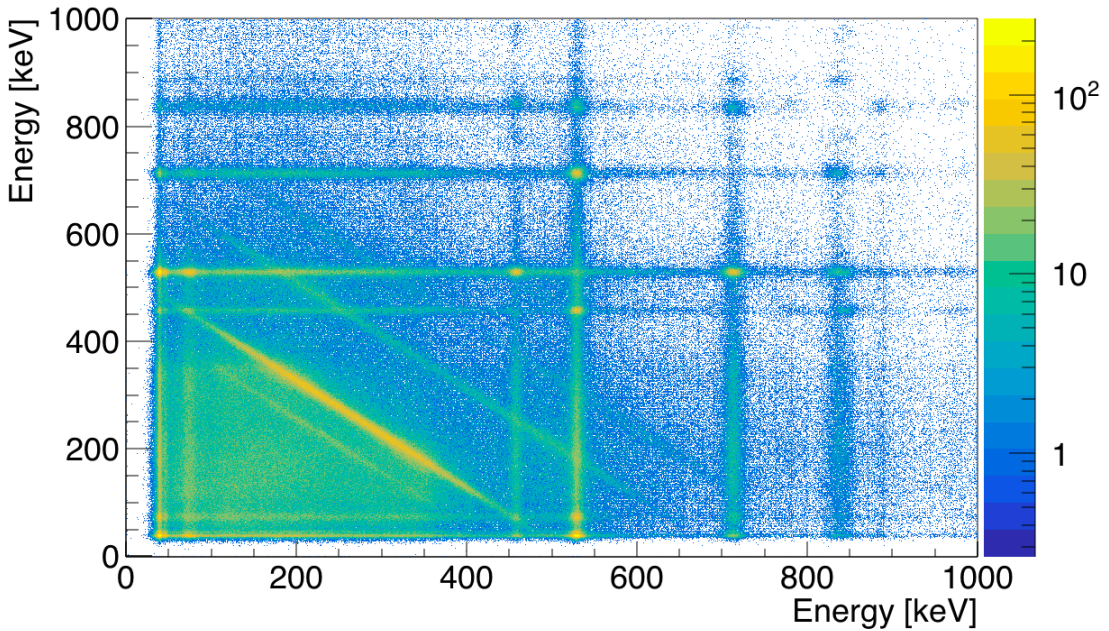


**Figure 5.4:**  $\gamma$ - $\gamma$  matrix, Doppler corrected for  $^{140}\text{Sm}$ . See the text for more information.

The CD has 16 rings, and consequently it covers 16 angular ranges in the laboratory system. In the IS495 experiment at ISOLDE in 2012, three excited states of  $^{140}\text{Sm}$  were populated, the first (531 keV) and second (990 keV) excited  $2^+$  states, in addition to the first  $4^+$  (1246 keV) state. At that time, the CD covered angles from  $49.7^\circ$  to  $146^\circ$  in the CM frame for the particles. The  $\gamma$ -ray intensities for the three states was measured from 5 separate ranges of CM scattering angles, Doppler corrected for the  $^{140}\text{Sm}$  projectiles. These intensities

were used to obtain the reduced transition probabilities, i.e. the  $B(E2)$  values of the states [78, 81, 82].

From the present experiment at ISOLDE, IS558 in 2017, excited states up to  $8^+$  were populated. When considering the detection of particles, the CD covers an angular range from  $36.6^\circ$  to  $136.0^\circ$  in the CM system, which can be divided into 23 independent angular ranges as given in [Table 3.2](#). [Figure 5.5](#) displays  $\gamma$ -ray spectra for 6 different ranges of CM scattering angles to illustrate the dependence of the excitation probabilities on the scattering angle. The spectra clearly demonstrate that multi-step excitations are more probable at large scattering angles, when the distance of closest approach is smaller, and the strength of the electromagnetic interaction is stronger. The 23 separate angle ranges displayed in [Figure 5.5](#) will provide plenty of new data points compared to the former 5 separate angle ranges. By further analyzing the 23 CM angle ranges, the precision of the previous measurements of the three  $B(E2)$  values will certainly be improved, and in addition several unknown  $B(E2)$  values will be obtained.

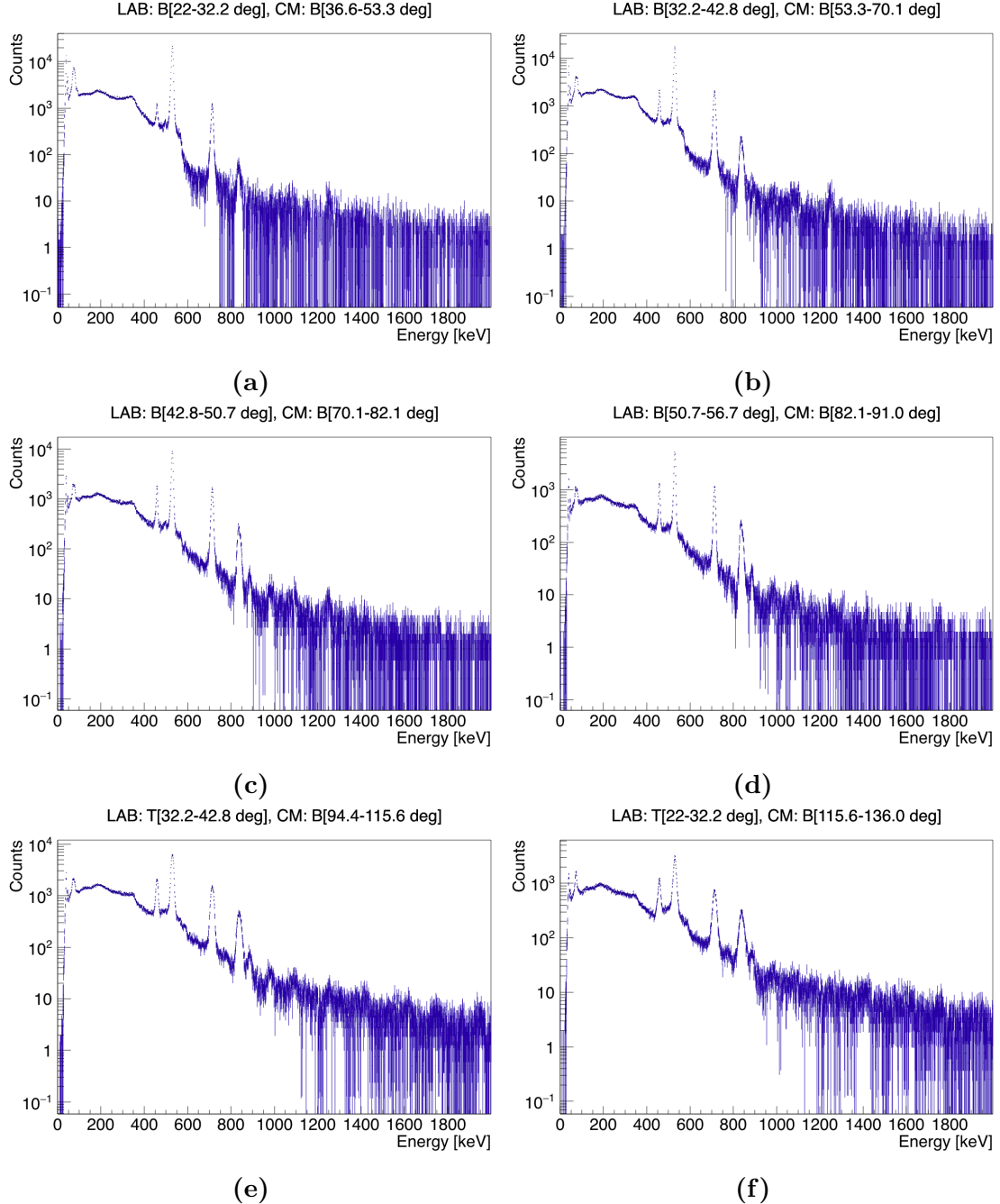


**Figure 5.5:** (a)-(d) shows when the beam particle hits the CD with the LAB angle as specified in the plot title, while (e)-(f) shows when the target hits the CD with the LAB angle as specified in the plot title. T is for target and B is for beam. Combined they cover the angle range  $\theta'_b \in [36.6^\circ, 136.0^\circ]$  of the beam in the CM frame.



# Chapter 6

## Summary and outlook

*"Nothing happens until something moves."*

– Albert Einstein

In this thesis, data from the Coulomb excitation experiment, IS558, at CERN-ISOLDE was analyzed. A beam of  $^{140}\text{Sm}$  ions was accelerated into a target of  $^{208}\text{Pb}$  at 4.65 MeV/u. ISOLDE developed software was utilized to simulate the Coulomb excitation process, producing the energy input for the calibration. The raw data from the experiment was sorted and used to calibrate the particle and  $\gamma$ -ray detectors.

The calibration process was performed in close collaboration with Dr. Liam Gaffney, the main developer of the *MiniballCoulexSort* code. To an extent, the present work beta-tested the development of the *MiniballCoulexSort* code. The quality of the (online) calibration was investigated and found very satisfactory. Then, the obtained calibration files were applied in the remaining sorting and data analysis. Several detector segments, namely, the innermost ring of the particle detector and a few segments of the  $\gamma$  detector array, were damaged and therefore excluded from the data set. At last, a fully calibrated data set was produced.

The **CLXAna** code performed a kinematic reconstruction and applied a Doppler correction to the  $\gamma$ -ray spectra. The resolution of the spectra is good, which demonstrates the quality of the calibration. A great number of known states up to, and including the  $8^+$  state was populated, in addition to two previously unknown  $\gamma$  transitions. A new transition at approximately 844 keV is assumed to be the "missing"  $3^+$  member of the  $\gamma$ -vibrational band built on the  $2_2^+$  state. This new  $3^+ \rightarrow 2_2^+$  transition, if verified, will certainly clarify the role of triaxial deformation in  $^{140}\text{Sm}$ . This is an important result that will help to better understand the structure of  $^{140}\text{Sm}$ . The new state will be a central aspect of the publication that is going to be written about the experiment. In addition, we observed a new transition with the  $\gamma$ -ray energy of approximately 1860 keV. None

of the known  $\gamma$  cascades in the level scheme add up to this energy, and there are no known transitions, unaccounted for, with the energy of approximately 1860 keV. From the  $\gamma$ -spectrum, there are no known candidates for which the 1860 keV transition may decay to. Coincidence analysis have to be performed to determine where the 1860 keV transition originates from. In the forthcoming work, the produced  $\gamma\gamma$  matrix can be investigated to verify the new transitions, and search for new transitions, extending the level scheme of  $^{140}\text{Sm}$ . As a last step of the present analysis, a set of singles spectra as a function of scattering angle was produced. These spectra are essential for the future analysis, to obtain the Coulomb excitation cross sections.

There are many possible improvements of the present data analysis. First, an improved, second user calibration of the particle detector may be performed. The shapes of the peaks have to be taken into account to improve the fitting. In the present work, we found that an automatic fitting of the peaks to determine the peak centroids inflicted many issues. For this reason, we propose that a future second calibration should be performed manually for each strip on the front and back side of the CD. In addition, the calibration might benefit form a review of the kinematic simulation. Second, in the present work, the beam was assumed to be very pure. In the further analysis, the possibility of beam contaminants should be investigated.

An efficiency calibration was not performed in the present work. This may be achieved by using the  $^{133}\text{Ba}$  and  $^{152}\text{Eu}$  source data. With the produced  $\gamma$  spectra and the efficiency calibration from the source data, it is possible to extract the intensities for the transitions for all 23 CM scattering angles. Each spectrum for the 23 different angular ranges will provide an independent set of  $\gamma$ -ray intensities for the various transitions.

In the next step of the Coulomb excitation analysis, a set of electromagnetic matrix elements will be fitted to the  $\gamma$ -ray intensities in a chi-square ( $\chi^2$ ) procedure. The known transition probabilities from the previous experiment (IS495) and known branching ratios can be used to constrain the fit. Since the present experiment (IS558) provides many more data points compared to the number of free parameters, the experiment will provide both transitional and diagonal matrix elements with good precision. The final step is to compare the  $B(E2)$  values and quadrupole moments with theoretical calculations, similar to what was done in [81].

It will be exciting to see from the two low-lying  $0^+$  states, i.e. the  $0_2^+$  and the  $0_3^+$ , what the shape of  $^{140}\text{Sm}$  is, and if there is any shape coexistence. In addition, and even more exciting, if the "missing" member of the  $\gamma$ -vibrational band, i.e. the  $3_1^+$  is identified, and how it affects the nuclear deformation in  $^{140}\text{Sm}$ .

# Appendices



## **Appendix A**

### **Acronyms and abbreviations**

---

ADC	Analog to Digital Converter
bash	Bourne-Again SHell
CERN	European Council for Nuclear Research (in French: Conseil Européen pour la Recherche Nucléaire)
CD	Compact Disc (also see DSSSD)
CM frame	Center of Mass frame
COULEX	COULomb EXcitation
DAQ	Data AcQuisition
DGF	Digital Gamma Finder
DSSSD	Double Sided Silicon Strip Detector (also known as CD)
EBIS	Electron Beam Ion Source
EM	ElectroMagnetic
GPS	General Purpose Separator
HIE-ISOLDE	High Intensity and Energy upgrade at ISOLDE
HIL	Heavy Ion Laboratory
HPGe	High Purity Germanium
HRS	High Resolution Separator
ISOL	Isotope Separator On Line
ISOLDE	ISOL DEvice
LAB frame	LABoRatory frame
LINAC	LINear ACcelerator
MAR <sub>a</sub> BQU	MBS And ROOT Based Online/Offline Utility
MBS	Multi Branch System
MED	MBS Event Data (also known as Miniball Event Data)
PES	Potential Energy Surface
PHD	Pulse-Height Defect
PSB	Proton Synchrotron Booster
RF	Radio Frequency
REX	Radioactive beam EXperiment
REXEgis	Radioactive beam EXperiment Electron Beam Ion Source
REXTRAP	Radioactive beam EXperiment TRAP
REX-ISOLDE	Radioactive beam EXperiment at ISOLDE
RIB	Radioactive Ion Beam
RILIS	Resonance Ionization Laser Ion Source
SRIM	Stopping and Range of Ions in Matter
TDC	Time to Digital Converter

---

# Appendix B

## Computer setup and environment

The *MiniballCoulexSort* code does not require extensive computing power to run. [Table B.1](#) shows the computer, and its specifications, applied in the sorting and data analysis. In total, the experimental raw data takes up about 60 GB of the disk (SSD). Therefore, the biggest limitation of the computer setup was the SSD<sup>1</sup>. When the sorting and event-building programs were run, the SSD space of the computer rapidly vanished.

**Table B.1:** The personal computer utilized in the sorting and data analysis.

Model	MacBook Air (13-inch, 2017)
OS	macOS High Sierra (Version 10.13.6)
Processor	1.8 GHz (Intel Core i5, dual core, 4 threads) Max turbo frequency: 2.90 Ghz
Memory	8 GB (1600 MHz DDR3)
SSD	128 GB

The relative path of *MiniballCoulexSort*, `kinsim3` and the ROOT framework on the computer was

```
~/GitHub/Miniball/MiniballCoulexSort  
~/GitHub/Miniball/kinsim  
~/GitHub(ROOT-framework/build
```

[Table B.2](#) shows the relative path of programs, scripts and files applied in this thesis. The settingsfile *MBSettings2017\_CLX\_IS558.dat*, and the calibration files *IS558-online.cal* and *IS558-user.cal* relevant to the current experiment

---

<sup>1</sup>The SSD (solid-state drive) is the internal storage device in the computer.

can be found in the directory specified in the table. The settings and calibration files are applied directly with *MiniballCoulexSort*, with the default path *~/GitHub/Miniball/MiniballCoulexSort/config*. The file *setup\_Sm.txt* is listed in the table twice, since there exists two files with identical names, one required for the plotting, and one for the fitting procedure.

**Table B.3** displays the run time for the event building with essentially all data files included.

**Table B.2:** Relative path of programs, scripts and files.

Relative path	Programs / scripts / files
<i>~/GitHub/Miniball/kinsim</i>	<i>kinsim3.cc</i>
<i>~/GitHub/Miniball/MiniballCoulexSort/MedToRoot</i>	<i>MedToRoot</i>
<i>~/GitHub/Miniball/MiniballCoulexSort/TreeBuilder</i>	<i>TreeBuilder</i>
<i>~/GitHub/Miniball/MiniballCoulexSort/CLXAna</i>	<i>AQ4Sort</i>
<i>~/GitHub/MasterThesis/Miniball-config</i>	<i>CLXAna</i>
	<i>MBSettings2017_CLX_IS558.dat</i>
	<i>IS558-online.cal</i>
	<i>IS558-user.cal</i>
	<i>config-IS558.dat</i>
<i>~/GitHub/MasterThesis/SRIM</i>	SRIM files
<i>~/GitHub/MasterThesis/Scripts/sorting</i>	<i>M2R.sh</i>
	<i>Q4S.sh</i>
	<i>Coulex.sh</i>
<i>~/GitHub/MasterThesis/Scripts/plotting</i>	<i>ParticlePlot.cpp</i>
	<i>GammaPlot.cpp</i>
	<i>setup_Sm.txt</i>
	<i>setup_Coulex.txt</i>
<i>~/GitHub/MasterThesis/Scripts/calibration</i>	<i>particle-calibration.py</i>
<i>~/GitHub/MasterThesis/Scripts/fitting</i>	<i>ParticleFit.cpp</i>
	<i>GammaFit.cpp</i>
	<i>setup_Sm.txt</i>
<i>~/GitHub/MasterThesis/Scripts/generators</i>	<i>ADC_generator.py</i>
	<i>DGF_generator.py</i>
	<i>Geometry_generator.py</i>
<i>~/GitHub(ROOT-framework/build</i>	<i>ROOT</i>
<i>~/GitHub(ROOT-framework/build/bin</i>	<i>hadd</i>

**Table B.3:** Run time for building event trees, timed with the built in command line script `time`.

Executable	Run time [min]
TreeBuilder	~ 45
AQ4Sort	~ 130



# Appendix C

## MiniballCoulexSort and ROOT

### C.1 Connecting MiniballCoulexSort with ROOT

*MiniballCoulexSort* requires access to the libraries of ROOT. The codes share their libraries by means of a dynamic loader, more information can be found in [83]. A *.rootrc* file have to be constructed and saved in the home folder of the computer. Roughly, the *.rootrc* file have to contain one line similar to the following

```
Unix .*. Root .DynamicPath:      .:</Users/trondwj/GitHub(ROOT-
framework/build/lib>:/Users/trondwj/GitHub/Miniball/
MiniballCoulexSort/lib :
```

The first part tells the system to use the dynamic loader of ROOT to connect the following paths. In the present computer setup, the lib folder of the ROOT install was

```
/Users/trondwj/GitHub/ROOT-framework/build/lib
```

and the lib folder of the *MiniballCoulexSort* was

```
/Users/trondwj/GitHub/Miniball/MiniballCoulexSort/lib
```

These paths are totally individual, entirely system dependent, it is unlikely that the location on another computer is identical. Therefore, these paths must be changed to fit your system.

After the construction of the file, the terminal have to be restarted, or the following command can be run in the terminal

```
$ source ~/.rootrc
```

## C.2 Running ROOT and MiniballCoulexSort from anywhere in the terminal

To run ROOT or the different scripts of *MiniballCoulexSort* anywhere in the terminal, you have to edit your *.bash\_profile*<sup>1</sup> file. In *.bash\_profile* the following commands were used

```
# Run ROOT from anywhere
export ROOTSYS=$HOME/GitHub(ROOT-framework/build
export PATH=$ROOTSYS/lib:$PATH
export PATH=$ROOTSYS/bin:$PATH
export DYLD_LIBRARY_PATH=$ROOTSYS/lib:$DYLD_LIBRARY_PATH

# Run MiniballCoulexSort from anywhere
export DYLD_LIBRARY_PATH=$HOME/GitHub/Miniball/
MiniballCoulexSort/lib:$DYLD_LIBRARY_PATH
export PATH=$HOME/GitHub/Miniball/MiniballCoulexSort/lib:$PATH
export PATH=$HOME/GitHub/Miniball/MiniballCoulexSort/bin:$PATH
```

The DYLD\_LIBRARY\_PATH is only relevant for Mac users. On other systems, use LD\_LIBRARY\_PATH instead. The paths of the *lib* and *bin* folders of both ROOT and *MiniballCoulexSort*, in addition to the *build* folder of your ROOT install needs to be inserted in *.bash\_profile*.

## C.3 CLXAna

### C.3.1 Input parameters

All input parameters for **CLXAna** are stated in the GitHub repository of *Miniball-CoulexSort*, but they are not explained in detail. From private communications with Dr. Liam Gaffney, the purpose of several input parameters have been clarified. In the following, a minimal working example of the **CLXAna** usage is listed

```
$ CLXAna -c <configuration filename> -cut <cut filename>
```

Here, ”-c” and ”-cut” are the so-called flags, followed by the file names of the configuration and the cut file, respectively. The run flags and their purpose may be summarized as:

- c The configuration file, if applied, must contain all of the input parameters, except the ”-cut” explained by the following flag.

---

<sup>1</sup> *.bash\_profile* on MacOS, *.bashrc* on Linux.

**-cut** The cut file must be stored in the `.root` format and contain the graphical cuts of the graphical cuts of the kinematics obtained from the particle histogram named "part" of the output file<sup>2</sup> of CLXAna.

**-Ex** To perform the Doppler correction of a specific state. Provide the excitation energy of the state in keV.

**-depth** The depth of the interaction in the target in mg/cm<sup>2</sup>. Usually assumed to be half of the target thickness. By applying this flag, it is possible to test different thickness values and assess if the Doppler correction was improved.

**-cdoffset** The rotation of the CD detector, i.e., the angle offset, with a default value of 242.6°. It is possible to optimize the angle, but the resulting value will most likely be close to the default angle.

**-deadlayer** The thickness of the Si dead layer in mm, with a default value of 0.0007 mm.

**-spededit** Not relevant for this experiment.

**-bg\_frac** This value depends on the time windows defined in TreeBuilder, which means it should be -0.75 for the current version. The number can be verified by taking the ratios of the  $\beta$ -decay background peaks in the prompt gammas ("p") and random gammas ("r") spectra in the output file of CLXAna. This is related to the time window with respect to REXEBIS. A window is defined for prompt in-beam events, and those outside of the window are sorted into the background spectra. Now, a weighted fraction of the background spectrum can be subtracted from the prompt spectrum, to get rid of uncorrelated background, such as  $\beta$ -decay that is in random coincidence with particles. The subtraction fraction required depends on the width of the time window.

In Section 4.3.3, the output of `Q4S.sh` using TreeBuilder was listed. The parameter

```
WeightPR: 0.75
```

is related to the "-bg\_frac" flag of CLXAna. The provided output value is positive, while the corresponding negative value have to be given as input, i.e., "-bg\_frac <-WeightPR>".

---

<sup>2</sup>The input of CLXAna is, in fact, dependent on one of its own output histograms. CLXAna makes a kinematic reconstruction to obtain the angle of the particles, and the "part" histogram can only be obtained with the kinematic reconstruction.

### C.3.2 Graphical cuts

In this thesis, the input parameters applied in the **CLXAna** code are found in the *config-IS558.dat* file. The first time **CLXAna** is run, every input parameter except **-cut** needs to be provided. A plot of energy vs. LAB angle named "part" is required in order to create the cut file. The "part" plot is found inside the *.root*-file sorted by **CLXAna**, since **CLXAna** makes a kinematic reconstruction to obtain the angle of the particles, which can only be done in the last part of the sorting. For this reason, it is only possible to look at particles against strips in *.root* files sorted by **TreeBuilder**.

Inside the *.root*-file sorted by **TreeBuilder**, another plot named "part" exist, but it contains energy vs. annular strip. To make the cut file, the "part" plot from the output file of **CLXAna** have to be opened<sup>3</sup>. From this plot, graphical cuts around the beam and target particle events have to be extracted separately. After making the cuts, right click and choose "SetName" to save the values of the cuts as "Bcut" and "Tcut"<sup>4</sup> for the beam and target, respectively. Then right click and choose "SaveAs", giving the name of a *.root*-file of your choice for each cut. Make sure to provide the *.root* extension. In this thesis, the files were saved as *Bcut.root* and *Tcut.root*, respectively. Then, the two files can be added together using a ROOT program called **hadd**, which can be run by the following commands

```
hadd outputfile.root input_file_1.root input_file_2.root
```

As described in [Section 4.3.7](#), **CLXAna** have to be run a second time with the "-cut" flag after the graphical cuts have been obtained. For the second run, the cut file is provided by the line

```
outputfile.root:Bcut:Tcut
```

where *:Bcut:Tcut* are the names of the cuts chosen in the step described above.

---

<sup>3</sup>It is advised to use log scale on the *z*-axis of "part" by utilizing the draw option "colz".

<sup>4</sup>These names can be chosen freely by the user, but must match the names provided as input when **CLXAna** is run the second time with the "-cut" flag.

# Appendix D

## Two-particle elastic collision

### D.1 Laboratory (LAB) frame of reference

The angles of the two-particle collision in the laboratory frame from [Figure 2.5](#) is calculated in the current section. In the following, a general approach is applied to simplify the notation. From [Figure 2.5](#) we can express the velocities as

$$\begin{aligned}\mathbf{u} &= \mathbf{u}_1 = u\hat{\mathbf{x}} \\ \mathbf{u}_2 &= 0 \\ \mathbf{v}_b &= \mathbf{v}_1 = v_1(\cos\theta\hat{\mathbf{x}} + \sin\theta\hat{\mathbf{y}}) \\ \mathbf{v}_t &= \mathbf{v}_2 = v_2(\cos\varphi\hat{\mathbf{x}} - \sin\varphi\hat{\mathbf{y}})\end{aligned}\tag{D.1}$$

where  $\mathbf{u}_1$  and  $\mathbf{v}_1$  is the initial and final velocity of the projectile, respectively, and  $\mathbf{u}_2$  and  $\mathbf{v}_2$  is the initial and final velocity of the target, respectively. With this notation, the mass of the projectile is  $m_b = m_1$ , and  $m_t = m_2$  is the mass of the target. The angles  $\theta_b = \theta$  and  $\theta_t = \varphi$  are the projectile and target angle, respectively. We also introduce a ratio of the projectile mass to the target mass,  $\alpha = m_1/m_2$ . Conservation of momentum gives

$$m_1\mathbf{u}_1 = m_1\mathbf{v}_1 + m_2\mathbf{v}_2$$

which in  $x$ -direction can be expressed as

$$\begin{aligned}m_1u &= m_1v_1 \cos\theta + m_2v_2 \cos\varphi \\ m_1(u - v_1 \cos\theta) &= m_2v_2 \cos\varphi \\ \frac{m_1}{m_2}(u - v_1 \cos\theta) &= v_2 \cos\varphi \\ \alpha(u - v_1 \cos\theta) &= v_2 \cos\varphi\end{aligned}\tag{D.2}$$

and in  $y$ -direction can be expressed as

$$\begin{aligned} 0 &= m_1 v_1 \sin \theta - m_2 v_2 \sin \varphi \\ m_1 v_1 \sin \theta &= m_2 v_2 \sin \varphi \\ \frac{m_1}{m_2} v_1 \sin \theta &= v_2 \sin \varphi \\ \alpha v_1 \sin \theta &= v_2 \sin \varphi \end{aligned} \quad (\text{D.3})$$

Conservation of energy gives

$$\begin{aligned} \frac{1}{2} m_1 \mathbf{u}_1^2 &= \frac{1}{2} m_1 \mathbf{v}_1^2 + \frac{1}{2} m_2 \mathbf{v}_2^2 \\ \frac{1}{2} m_1 (u^2 - v_1^2) &= \frac{1}{2} m_2 v_2^2 \\ \frac{m_1}{m_2} (u^2 - v_1^2) &= v_2^2 \\ \alpha (u^2 - v_1^2) &= v_2^2 \end{aligned} \quad (\text{D.4})$$

We now have three equations, [Equation \(D.2\)](#) - [Equation \(D.4\)](#), with four unknown quantities ( $v_1, \theta, v_2, \varphi$ ). Using the target angle  $\varphi$  as an independent variable, we can find expressions for the other three variables. Squaring [Equation \(D.2\)](#)

$$\begin{aligned} \alpha^2 (u - v_1 \cos \theta)^2 &= v_2^2 \cos^2 \varphi \\ \alpha^2 (u^2 - 2uv_1 \cos \theta + v_1^2 \cos^2 \theta) &= v_2^2 \cos^2 \varphi \end{aligned}$$

and [Equation \(D.3\)](#)

$$\alpha^2 v_1^2 \sin^2 \theta = v_2^2 \sin^2 \varphi$$

and adding them together gives

$$\begin{aligned} \alpha^2 (u^2 - 2uv_1 \cos \theta + v_1^2 \cos^2 \theta + v_1^2 \sin^2 \theta) &= v_2^2 (\cos^2 \varphi + \sin^2 \varphi) \\ \alpha^2 (u^2 - 2uv_1 \cos \theta + v_1^2) &= v_2^2 \\ \alpha^2 u^2 - 2\alpha^2 uv_1 \cos \theta + \alpha^2 v_1^2 &= v_2^2 \\ \alpha^2 v_1^2 &= -\alpha^2 u^2 + 2\alpha^2 uv_1 \cos \theta + v_2^2 \\ \alpha^2 v_1^2 &= -\alpha^2 u^2 + 2\alpha u(\alpha v_1 \cos \theta) + v_2^2 \end{aligned} \quad (\text{D.5})$$

From [Equation \(D.2\)](#) we have

$$\begin{aligned} \alpha(u - v_1 \cos \theta) &= v_2 \cos \varphi \\ \alpha u - \alpha v_1 \cos \theta &= v_2 \cos \varphi \\ \alpha v_1 \cos \theta &= \alpha u - v_2 \cos \varphi \end{aligned} \quad (\text{D.6})$$

Substituting for [Equation \(D.6\)](#) into [Equation \(D.5\)](#) we get

$$\begin{aligned}\alpha^2 v_1^2 &= -\alpha^2 u^2 + 2\alpha u(\alpha u - v_2 \cos \varphi) + v_2^2 \\ \alpha^2 v_1^2 &= -\alpha^2 u^2 + 2\alpha^2 u^2 - 2\alpha u v_2 \cos \varphi + v_2^2 \\ \alpha^2 v_1^2 &= \alpha^2 u^2 - 2\alpha u v_2 \cos \varphi + v_2^2\end{aligned}\tag{D.7}$$

Using [Equation \(D.4\)](#) we get

$$\begin{aligned}\left(\frac{\alpha}{\alpha}\right) \alpha(u^2 - v_1^2) &= v_2^2 \\ \alpha^2(u^2 - v_1^2) &= \alpha v_2^2 \\ \alpha^2 u^2 - \alpha^2 v_1^2 &= \alpha v_2^2 \\ \alpha^2 v_1^2 &= \alpha^2 u^2 - \alpha v_2^2\end{aligned}\tag{D.8}$$

Combining [Equation \(D.7\)](#) and [Equation \(D.8\)](#) gives

$$\begin{aligned}\alpha^2 u^2 - 2\alpha u v_2 \cos \varphi + v_2^2 &= \alpha^2 u^2 - \alpha v_2^2 \\ v_2^2 + \alpha v_2^2 &= 2\alpha u v_2 \cos \varphi \\ v_2^2(1 + \alpha) &= 2\alpha u v_2 \cos \varphi \\ v_2 &= 2 \left( \frac{\alpha}{1 + \alpha} \right) u \cos \varphi\end{aligned}\tag{D.9}$$

Substituting [Equation \(D.9\)](#) into [Equation \(D.8\)](#) we get

$$\begin{aligned}\alpha^2 v_1^2 &= \alpha^2 u^2 - \alpha \left( 2 \left( \frac{\alpha}{1 + \alpha} \right) u \cos \varphi \right)^2 \\ v_1^2 &= u^2 - \frac{1}{\alpha} \left( 4 \left( \frac{\alpha^2}{(1 + \alpha)^2} \right) u^2 \cos^2 \varphi \right) \\ v_1^2 &= u^2 \left( 1 - 4 \left( \frac{\alpha}{(1 + \alpha)^2} \right) \cos^2 \varphi \right) \\ v_1 &= u \sqrt{1 - 4 \frac{\alpha}{M} \cos^2 \varphi}\end{aligned}\tag{D.10}$$

where  $\alpha/M = \alpha/(1 + \alpha)^2$ . The ratio of [Equation \(D.3\)](#) and [Equation \(D.6\)](#) gives

$$\begin{aligned}\frac{\alpha v_1 \sin \theta}{\alpha v_1 \cos \theta} &= \frac{v_2 \sin \varphi}{\alpha u - v_2 \cos \varphi} \\ \tan \theta &= \frac{v_2 \sin \varphi}{\alpha u - v_2 \cos \varphi}\end{aligned}\tag{D.11}$$

Inserting [Equation \(D.9\)](#) into [Equation \(D.11\)](#) gives

$$\begin{aligned}
 \tan \theta &= \frac{\left(2\left(\frac{\alpha}{1+\alpha}\right) u \cos \varphi\right) \sin \varphi}{\alpha u - \left(2\left(\frac{\alpha}{1+\alpha}\right) u \cos \varphi\right) \cos \varphi} \\
 \tan \theta &= \frac{\alpha u \left(\frac{1}{1+\alpha}\right) 2 \sin \varphi \cos \varphi}{\alpha u \left(1 - 2\left(\frac{1}{1+\alpha}\right) \cos^2 \varphi\right)} \\
 \tan \theta &= \frac{\sin 2\varphi}{\left(1 + \alpha\right) \left(1 - 2\left(\frac{1}{1+\alpha}\right) \cos^2 \varphi\right)} \\
 \tan \theta &= \frac{\sin 2\varphi}{1 + \alpha - 2 \cos^2 \varphi} \\
 \tan \theta &= \frac{\sin 2\varphi}{\alpha - (2 \cos^2 \varphi - 1)} \\
 \tan \theta &= \frac{\sin 2\varphi}{\alpha - \cos 2\varphi} \\
 \theta &= \arctan \left( \frac{\sin 2\varphi}{\alpha - \cos 2\varphi} \right)
 \end{aligned} \tag{D.12}$$

Substituting back the variable names from the LAB frame in [Figure 2.5](#) into [Equation \(D.12\)](#) gives

$$\theta_b = \arctan \left( \frac{\sin 2\theta_t}{\alpha - \cos 2\theta_t} \right) \tag{D.13}$$

which is applied in [Table 3.2](#) in [Chapter 3](#).

## D.2 Center of mass (CM) frame of reference

Using the same notation as in [Section D.1](#), the velocities in the CM frame (see [Figure 2.5](#)) can be expressed as

$$\begin{aligned}
 \mathbf{u}'_1 &= u'_1 \hat{\mathbf{x}} \\
 \mathbf{u}'_2 &= u'_2 \hat{\mathbf{x}} \\
 \mathbf{v}'_b &= \mathbf{v}'_1 = v'_1 (\cos \theta' \hat{\mathbf{x}} + \sin \theta' \hat{\mathbf{y}}) \\
 \mathbf{v}'_t &= \mathbf{v}'_2 = v'_2 (-\cos \theta' \hat{\mathbf{x}} - \sin \theta' \hat{\mathbf{y}}) = -v'_2 (\cos \theta' \hat{\mathbf{x}} + \sin \theta' \hat{\mathbf{y}})
 \end{aligned} \tag{D.14}$$

where  $\mathbf{u}'_1$  and  $\mathbf{v}'_1$  is the initial and final velocity of the projectile, respectively, and  $\mathbf{u}'_2$  and  $\mathbf{v}'_2$  is the initial and final velocity of the target, respectively. As in the LAB frame,  $m_b = m_1$  and  $m_t = m_2$ , while the angle  $\theta'_b = \theta'$  is the projectile angle. In the center of mass (CM) frame of reference, the position of the center

of mass is given by

$$\mathbf{R} = \frac{m_1 \mathbf{r}_1 + m_2 \mathbf{r}_2}{m_1 + m_2} \quad (\text{D.15})$$

and the velocity is

$$\mathbf{V} = \frac{d\mathbf{R}}{dt} = \frac{d}{dt} \left( \frac{m_1 \mathbf{r}_1 + m_2 \mathbf{r}_2}{m_1 + m_2} \right) = \frac{m_1 \mathbf{u}'_1 + m_2 \mathbf{u}'_2}{m_1 + m_2} \quad (\text{D.16})$$

At the origin of the CM frame,  $\mathbf{R} = 0$ , which implies  $\mathbf{V} = 0$ . The total momentum before the collision is

$$\begin{aligned} m_1 \mathbf{u}'_1 + m_2 \mathbf{u}'_2 &= 0 \\ m_2 \mathbf{u}'_2 &= -m_1 \mathbf{u}'_1 \\ \mathbf{u}'_2 &= -\frac{m_1}{m_2} \mathbf{u}'_1 \\ \mathbf{u}'_2 &= -\alpha \mathbf{u}'_1 \end{aligned} \quad (\text{D.17})$$

and after the collision it is

$$\begin{aligned} m_1 \mathbf{v}'_1 + m_2 \mathbf{v}'_2 &= 0 \\ m_2 \mathbf{v}'_2 &= -m_1 \mathbf{v}'_1 \\ \mathbf{v}'_2 &= -\frac{m_1}{m_2} \mathbf{v}'_1 \\ \mathbf{v}'_2 &= -\alpha \mathbf{v}'_1 \\ -v'_2(\cos \theta' \hat{\mathbf{x}} + \sin \theta' \hat{\mathbf{y}}) &= -\alpha v'_1(\cos \theta' \hat{\mathbf{x}} + \sin \theta' \hat{\mathbf{y}}) \\ v'_2 &= \alpha v'_1 \end{aligned} \quad (\text{D.18})$$

Conservation of energy gives

$$\begin{aligned} \frac{1}{2} m_1 u'^2_1 + \frac{1}{2} m_2 u'^2_2 &= \frac{1}{2} m_1 v'^2_1 + \frac{1}{2} m_2 v'^2_2 \\ m_1 u'^2_1 + m_2 u'^2_2 &= m_1 v'^2_1 + m_2 v'^2_2 \end{aligned} \quad (\text{D.19})$$

Substituting [Equation \(D.17\)](#) and [Equation \(D.18\)](#) into [Equation \(D.19\)](#) gives

$$\begin{aligned} m_1 u'^2_1 + m_2 (-\alpha u'_1)^2 &= m_1 v'^2_1 + m_2 (\alpha v'_1)^2 \\ m_1 u'^2_1 + \alpha^2 m_2 u'^2_1 &= m_1 v'^2_1 + \alpha^2 m_2 v'^2_1 \\ (m_1 + \alpha^2 m_2) u'^2_1 &= (m_1 + \alpha^2 m_2) v'^2_1 \\ u'^2_1 &= v'^2_1 \\ u'_1 &= v'_1 \end{aligned} \quad (\text{D.20})$$

Substituting [Equation \(D.20\)](#) into [Equation \(D.17\)](#) gives

$$u'_2 = -\alpha v'_1 \quad (\text{D.21})$$

which is used in [Section D.3](#).

### D.3 Connection between the LAB frame and the CM frame

Galilean transformations describes the relationship between the LAB frame and the CM frame

$$\begin{aligned} x' &= x - vt & v'_x &= v_x - V_{cm} \\ y' &= y & v'_y &= v_y \\ z' &= z & v'_z &= v_z \\ t' &= t \end{aligned}$$

where  $(x, y, z)$  is the Cartesian coordinates and  $V_{cm}$  is the velocity of the CM frame. The time in the CM frame and LAB frame is  $t'$  and  $t$ , respectively. Applying the same notation as in [Section D.1](#) and [Section D.2](#). In the LAB frame of [Figure 2.5](#), conservation of momentum is given by

$$m_1 \mathbf{u}_1 + m_2 \mathbf{u}_2 = m_1 \mathbf{v}_1 + m_2 \mathbf{v}_2 = (m_1 + m_2) \mathbf{V} \quad (\text{D.22})$$

which can be written as

$$\begin{aligned} m_1 \mathbf{u}_1 + m_2 \mathbf{u}_2 &= (m_1 + m_2) \mathbf{V} \\ \mathbf{V} &= \frac{m_1 \mathbf{u}_1 + m_2 \mathbf{u}_2}{m_1 + m_2} & \mathbf{u}_2 &= 0 \\ \mathbf{V} &= \frac{m_1}{m_1 + m_2} \mathbf{u}_1 \\ \mathbf{V} &= \frac{\alpha}{1 + \alpha} u \hat{\mathbf{x}} \\ V &= \frac{\alpha}{1 + \alpha} u \end{aligned} \quad (\text{D.23})$$

Using Galilean transformations, the connection between  $\mathbf{v}'_1$  and  $\mathbf{v}_1$  is expressed as

$$\begin{aligned}\mathbf{v}'_1 &= \mathbf{v}_1 - \mathbf{V} \\ \mathbf{v}_1 &= \mathbf{v}'_1 + \mathbf{V}\end{aligned}\quad (\text{D.24})$$

which in  $x$ -direction gives

$$v_1 \cos \theta = v'_1 \cos \theta' + V \quad (\text{D.25})$$

and in  $y$ -direction gives

$$v_1 \sin \theta = v'_1 \sin \theta' \quad (\text{D.26})$$

The ratio of [Equation \(D.26\)](#) and [Equation \(D.25\)](#) gives

$$\begin{aligned}\frac{v_1 \sin \theta}{v_1 \cos \theta} &= \frac{v'_1 \sin \theta'}{v'_1 \cos \theta' + V} \\ \tan \theta &= \frac{\sin \theta'}{\cos \theta' + \frac{V}{v'_1}} \\ \tan \theta &= \frac{\sin \theta'}{\frac{V}{v'_1} + \cos \theta'}\end{aligned}\quad (\text{D.27})$$

We need to reformulate the velocity ratio. Substitution from [Equation \(D.20\)](#) gives

$$\frac{V}{v'_1} = \frac{V}{u'_1} \quad (\text{D.28})$$

Applying the Galilean transformation and [Equation \(D.23\)](#) we have that

$$\begin{aligned}\mathbf{u}'_1 &= \mathbf{u}_1 - \mathbf{V} \\ u'_1 &= u_1 - V \\ u'_1 &= u - \frac{\alpha}{1+\alpha} u \\ u'_1 &= u \left(1 - \frac{\alpha}{1+\alpha}\right) \\ u'_1 &= u \left(\frac{1+\alpha-\alpha}{1+\alpha}\right) \\ u'_1 &= \frac{1}{1+\alpha} u\end{aligned}\quad (\text{D.29})$$

Substituting [Equation \(D.23\)](#) and [Equation \(D.29\)](#) into [Equation \(D.28\)](#) gives

$$\frac{V}{u'_1} = \frac{\frac{\alpha}{1+\alpha}u}{\frac{1}{1+\alpha}u} = \alpha \quad (\text{D.30})$$

Substituting [Equation \(D.30\)](#) into [Equation \(D.27\)](#) gives

$$\begin{aligned} \tan \theta &= \frac{\sin \theta'}{\alpha + \cos \theta'} \\ \theta &= \arctan \left( \frac{\sin \theta'}{\alpha + \cos \theta'} \right) \end{aligned} \quad (\text{D.31})$$

Inserting the variable names from the CM frame of [Figure 2.5](#) into [Equation \(D.31\)](#) gives

$$\theta_b = \arctan \left( \frac{\sin \theta'_b}{\alpha + \cos \theta'_b} \right) \quad (\text{D.32})$$

The expression for the second scattering angle can be found in a similar manner. Using Galilean transformations, the connection between  $\mathbf{v}'_2$  and  $\mathbf{v}_2$  is expressed as

$$\begin{aligned} \mathbf{v}'_2 &= \mathbf{v}_2 - \mathbf{V} \\ \mathbf{v}_2 &= \mathbf{v}'_2 + \mathbf{V} \end{aligned} \quad (\text{D.33})$$

which in  $x$ -direction gives

$$\begin{aligned} v_2 \cos \varphi &= -v'_2 \cos \theta' + V \\ v_2 \cos \varphi &= V - v'_2 \cos \theta' \end{aligned} \quad (\text{D.34})$$

and in  $y$ -direction gives

$$v_2 \sin \varphi = v'_2 \sin \theta' \quad (\text{D.35})$$

The ratio of [Equation \(D.35\)](#) and [Equation \(D.34\)](#) gives

$$\begin{aligned} \frac{v_2 \sin \varphi}{v_2 \cos \varphi} &= \frac{v'_2 \sin \theta'}{V - v'_2 \cos \theta'} \\ \tan \varphi &= \frac{\sin \theta'}{\frac{V}{v'_2} - \cos \theta'} \end{aligned} \quad (\text{D.36})$$

To reformulate the velocity ratio, we substitute [Equation \(D.18\)](#) into [Equa-](#)

tion (D.20) giving

$$\frac{V}{v'_2} = \frac{V}{\alpha v'_1} = \frac{V}{\alpha u'_1} \quad (\text{D.37})$$

and inserting Equation (D.30) into Equation (D.37) gives

$$\frac{V}{v'_2} = \frac{V}{\alpha \frac{V}{\alpha}} = 1 \quad (\text{D.38})$$

and substituting Equation (D.38) into Equation (D.36) gives

$$\begin{aligned} \tan \varphi &= \frac{\sin \theta'}{1 - \cos \theta'} = \frac{1}{\frac{1-\cos \theta'}{\sin \theta'}} = \frac{1}{\tan \frac{\theta'}{2}} = \cot \frac{\theta'}{2} \\ \varphi &= \frac{1}{2}(\pi - \theta') \text{ [radians]} = \frac{1}{2}(180^\circ - \theta') \text{ [degrees]} \end{aligned} \quad (\text{D.39})$$

Inserting the variable names from Figure 2.5 into Equation (D.39) gives

$$\theta_t = \frac{1}{2}(\pi - \theta'_b) \text{ [radians]} = \frac{1}{2}(180^\circ - \theta'_b) \text{ [degrees]} \quad (\text{D.40})$$



## **Appendix E**

### **Signal cable wiring of the CD and naming of histograms**

**Table E.1:** Signal cable wiring of the CD into the ADCs for Coulomb excitation experiments. The first two columns show the range of the possible numbers of the ADC and the quadrants.

ADC range	Quadrant range	Channel number	Front strip [F] or back strip [B]
0 - 3	1 - 4	0	F
0 - 3	1 - 4	1	F
0 - 3	1 - 4	2	F
0 - 3	1 - 4	3	F
0 - 3	1 - 4	4	F
0 - 3	1 - 4	5	F
0 - 3	1 - 4	6	F
0 - 3	1 - 4	7	F
0 - 3	1 - 4	8	F
0 - 3	1 - 4	9	F
0 - 3	1 - 4	10	F
0 - 3	1 - 4	11	F
0 - 3	1 - 4	12	F
0 - 3	1 - 4	13	F
0 - 3	1 - 4	14	F
0 - 3	1 - 4	15	F
0 - 3	1 - 4	16	B
0 - 3	1 - 4	17	B
0 - 3	1 - 4	18	B
0 - 3	1 - 4	19	B
0 - 3	1 - 4	20	B
0 - 3	1 - 4	21	B
0 - 3	1 - 4	22	B
0 - 3	1 - 4	23	B
0 - 3	1 - 4	24	B
0 - 3	1 - 4	25	B
0 - 3	1 - 4	26	B
0 - 3	1 - 4	27	B
0 - 3		28	Empty
0 - 3		29	Empty
0 - 3		30	Empty
0 - 3	1 - 4	31	PAD
4		0	Ionization Chamber
4		1	Ionization Chamber

**Table E.2:** The naming and counting convention chosen for the CD with the corresponding naming of histograms from `TreeBuilder` and `AQ4Sort`.

Quadrant number	Chosen counting		Histograms	
	Front strip [F] or Back strip [B]		TreeBuilder	AQ4Sort
1	F 1		adc_0_15	fE_Q1_f16
1	F 2		adc_0_14	fE_Q1_f15
1	F 3		adc_0_13	fE_Q1_f14
:	:		:	:
1	F 15		adc_0_1	fE_Q1_f2
1	F 16		adc_0_0	fE_Q1_f1
1	B 1		adc_0_16	bE_Q1_b1
1	B 2		adc_0_17	bE_Q1_b2
1	B 3		adc_0_18	bE_Q1_b3
:	:		:	:
1	B 11		adc_0_26	bE_Q1_b11
1	B 12		adc_0_27	bE_Q1_b12
2	F 1		adc_1_15	fE_Q2_f16
:	:		:	:
2	F 16		adc_1_0	fE_Q2_f1
2	B 1		adc_1_16	bE_Q2_b1
:	:		:	:
2	B 12		adc_1_27	bE_Q2_b12
3	F 1		adc_2_15	fE_Q3_f16
:	:		:	:
3	F 16		adc_2_0	fE_Q3_f1
3	B 1		adc_2_16	bE_Q3_b1
:	:		:	:
3	B 12		adc_2_27	bE_Q3_b12
4	F 1		adc_3_15	fE_Q4_f16
:	:		:	:
4	F 16		adc_3_0	fE_Q4_f1
4	B 1		adc_3_16	bE_Q4_b1
:	:		:	:
4	B 12		adc_3_27	bE_Q4_b12



# Appendix F

## kinsim3

### F.1 The main function

The main function of `kinsim3` looks like the following

```
kinsim3(Zb, Zt, Ab, At, thick, Eb, dEb, Ex, res, cd_dist, flat  
, Nevts, srim_dir)
```

where  $Z_b$  and  $Z_t$  are the proton number of the beam and target, respectively.  $A_b$  and  $A_t$  is the mass number of the beam and target, respectively.  $thick$  is the target thickness in mg/cm<sup>2</sup>,  $E_b$  is the beam energy in MeV/u,  $dEb$  is the spread of the beam energy in MeV/u.  $Ex$  is the excitation energy in MeV,  $res$  is the detector resolution in percent,  $cd\_dist$  is the distance form the target to the CD in mm.  $flat$  is the choice of a uniform or angular distribution,  $Nevts$  is the number of particle events and `srim_dir` is the relative path of the SRIM directory. For the Si dead layer in `kinsim3`, the SRIM files must have units of MeV/mm.

To load `kinsim3` into ROOT, the `.L <filename>` command was used

```
$ cd ~/GitHub/Miniball/kinsim  
$ root  
root [0] .L kinsim3.cc++
```

Adding the '++' at the end, forces ROOT to compile the code. After the simulation program was run, the file was moved and renamed with the `mv` command.

### F.2 CD simulation

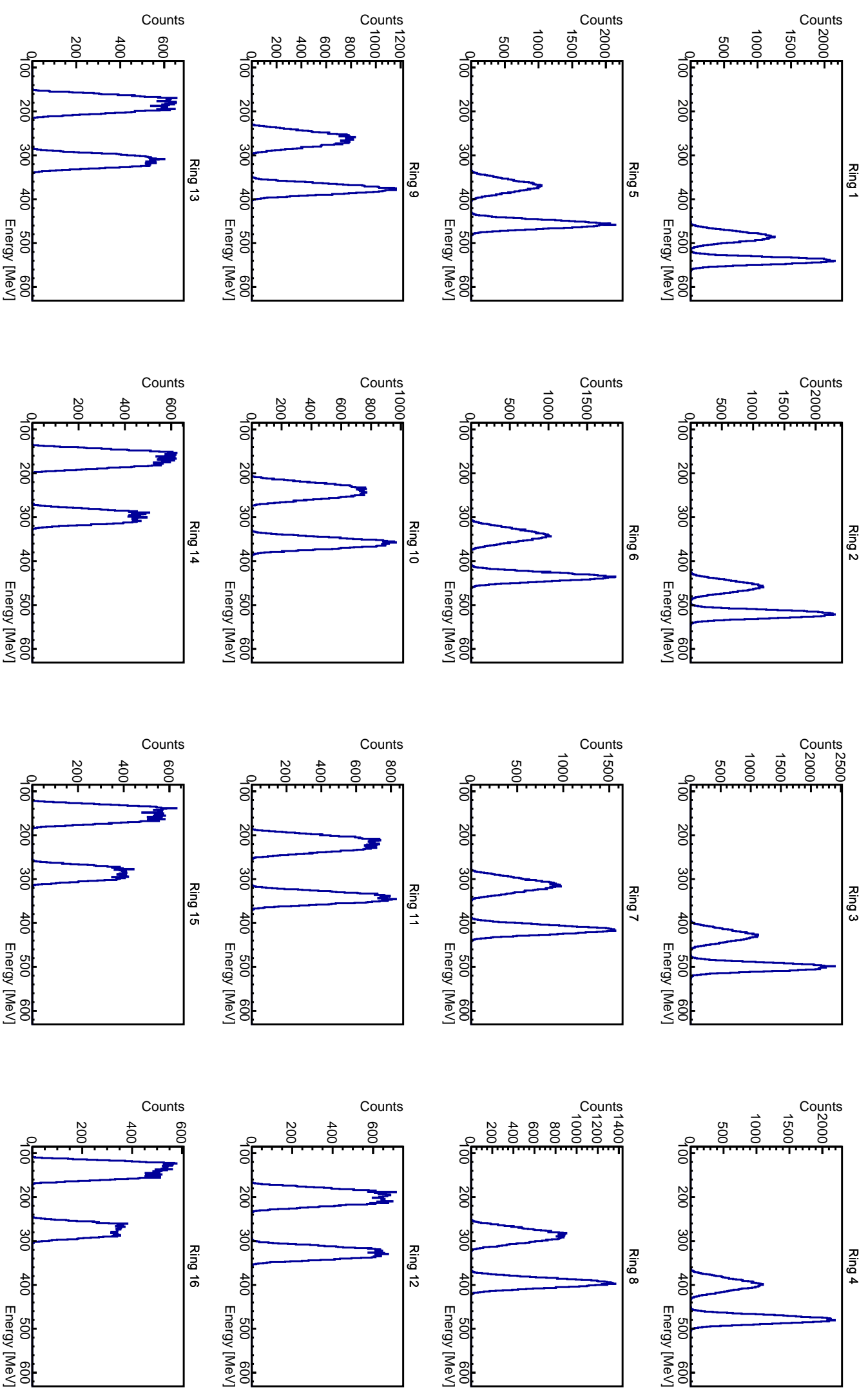
On the subsequent page, the CD simulation without the Rutherford cross section is presented for each ring. Ring 1 is the innermost ring and ring 16 is the outermost ring. The plots display simulated counts vs. energy, where the first

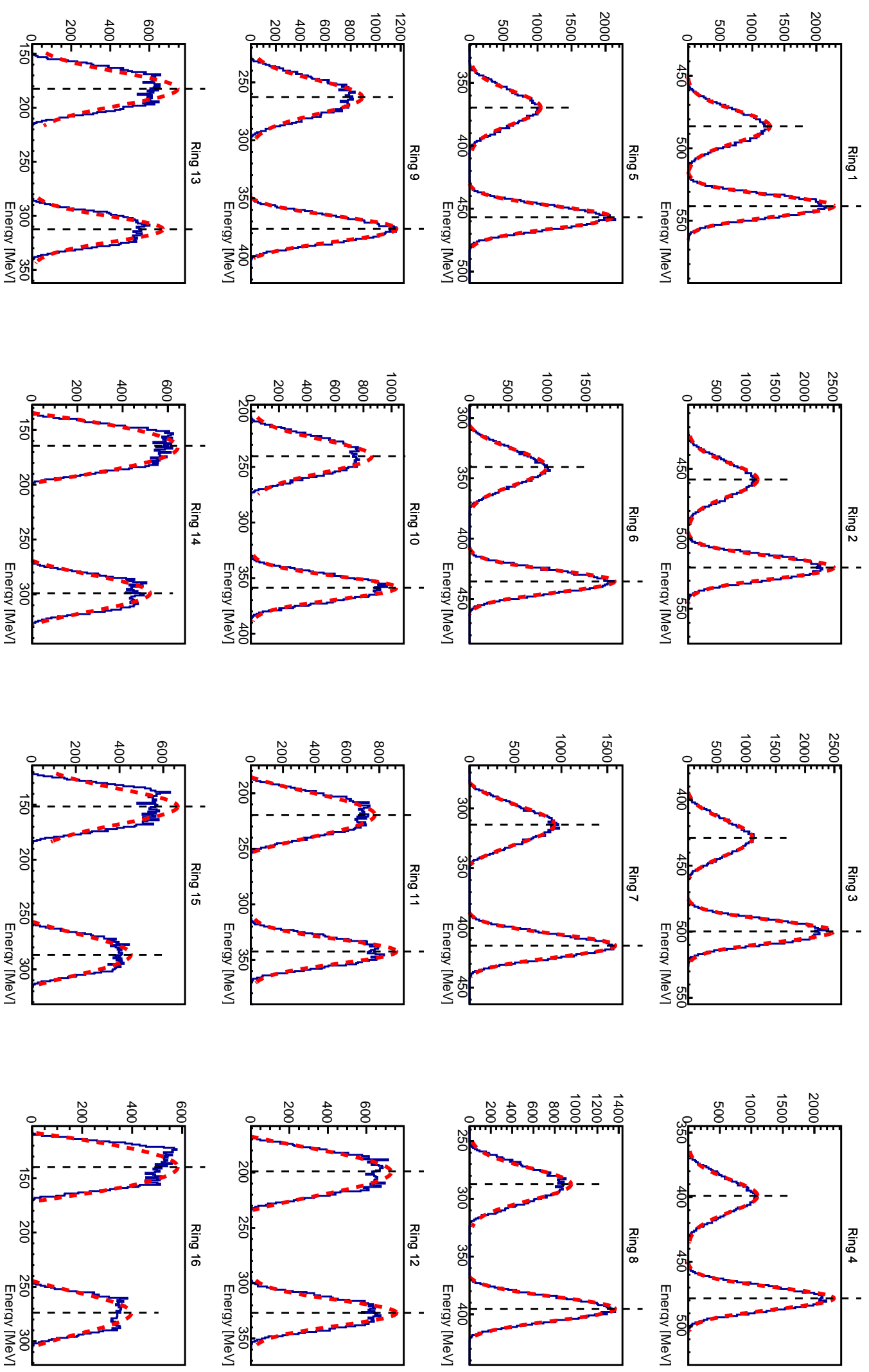
peak (at lower energy) is  $^{208}\text{Pb}$  and the second peak (at higher energy) is  $^{140}\text{Sm}$ . The plots were grabbed from the *.root*-file by the commands

```
$ cd ~/GitHub/MasterThesis/Scripts/plotting
$ root
root [0] .L ParticlePlot.cpp++
root [1] simulation_plot("setup_Sm.txt", 0)
... <showing output from script>
```

The page following the CD simulation displays the fitting of the CD simulation. The red dotted curves shows the fitting of the peaks, and the vertical black dotted lines indicate the centroids of the peaks. The fitting is performed by running the following commands

```
$ cd ~/GitHub/MasterThesis/Scripts/fitting
$ root
root [0] .L ParticleFit.cpp++
root [1] simulation_fit("setup_Sm.txt")
... <showing output from script>
```





## Appendix G

### Participants of the experiment

Table G.1

Name	Institution
Liam Gaffney	CERN
Nigel Warr	CERN
Efstathios Giannopoulos	University of Jyväskylä / CERN
Radostina Zidarova	University of Sofia / CERN
Kenzo John Abrahams	University of the Western Cape
Andreas Görden	University of Oslo
Trond Wiggo Johansen	University of Oslo
Victor Modamio Høybjør	University of Oslo
Sunniva Siem	University of Oslo
Fabio Zeiser	University of Oslo
Vetle Wegner Ingeberg	University of Oslo
Gry Merete Tveten	University of Oslo
Kseniia Rezynkina	University of Leuven
Peter Reiter	University of Köln
Joakim Cederkäll	Lund University
Amar Boukhari	CNRS/IN2P3/CSNSM Orsay
Andrei Andreyev	University of York





# Bibliography

- [1] K. Heyde. *Basic Ideas and Concepts in Nuclear Physics: An Introductory Approach*. IOP Publishing, 2nd edition, 1999. ISBN 0750305347.
- [2] S. G. Nilsson and I. Ragnarsson. *Shapes and Shells in Nuclear Structure*. Cambridge University Press, 2005. ISBN 9780521373777.
- [3] M. G. Mayer. The Shell Model. *Science, New Series*, 145(3636):999–1006, 1964. URL <https://www.jstor.org/stable/1714069>.
- [4] P. Cappellaro. 22.02 Introduction to Applied Nuclear Physics. Massachusetts Institute of Technology: MIT OpenCourseWare, <https://ocw.mit.edu>, Spring 2012. URL [https://ocw.mit.edu/courses/nuclear-engineering/22-02-introduction-to-applied-nuclear-physics-spring-2012/lecture-notes/MIT22\\_02S12\\_lec01.pdf](https://ocw.mit.edu/courses/nuclear-engineering/22-02-introduction-to-applied-nuclear-physics-spring-2012/lecture-notes/MIT22_02S12_lec01.pdf). Accessed: August 2019.
- [5] Three shapes in one nucleus: the elusive state in Sulfur 43 found. Michigan State University: National Superconducting Cyclotron Laboratory. URL <https://www.nscl.msu.edu/news/science/news-S43.html>. Accessed: August 2019.
- [6] R. F. Casten and N. V. Zamfir. Empirical realization of acritical point description in atomic nuclei. *Physical Review Letters*, 87(5):52503–1–52503–4, 2001. ISSN 10797114. doi: 10.1103/PhysRevLett.87.052503.
- [7] S. Hilaire and M. Girod. Large-scale mean-field calculations from proton to neutron drip lines using the D1S Gogny force. *European Physical Journal A*, 33(2):237–241, 2007. ISSN 14346001. doi: 10.1140/epja/i2007-10450-2.
- [8] Hartree-Fock-Bogoliubov results based on the Gogny force. The French Alternative Energies and Atomic Energy Commission (CEA). URL [http://www-phynu.cea.fr/science\\_en\\_ligne/carte\\_potentiels\\_microscopiques/carte\\_potentiel\\_nucleaire\\_eng.htm](http://www-phynu.cea.fr/science_en_ligne/carte_potentiels_microscopiques/carte_potentiel_nucleaire_eng.htm). Accessed: August 2019.
- [9] F. Iachello. Dynamic symmetries at the critical point. *Physical Review Letters*, 85(17):3580–3583, 2000. ISSN 00319007. doi: 10.1103/PhysRevLett.85.3580.

- [10] GitHub repository of the master thesis. URL <https://github.com/wiggoen/MasterThesis>.
- [11] K. S. Krane. *Introductory Nuclear Physics*. Wiley, 1987. ISBN 9780471805533. URL <https://www.wiley.com/en-us/Introductory+Nuclear+Physics%2C+3rd+Edition-p-9780471805533>.
- [12] P. Ring and P. Schuck. *The Nuclear Many-Body Problem*. Springer-Verlag Berlin Heidelberg, 1980. ISBN 3540098208.
- [13] M. Klintefjord. *Evolution of deformation and collectivity away from magic numbers*. PhD thesis, University of Oslo, May 2016. URL <http://urn.nb.no/URN:NBN:no-56121>.
- [14] D. L. Hill and J. A. Wheeler. Nuclear Constitution and the Interpretation of Fission Phenomena. *Physical Review*, 89(5):1102–1145, 1953.
- [15] K. Alder, A. Bohr, T. Huus, B. Mottelson, and A. Winther. Study of nuclear structure by electromagnetic excitation with accelerated ions. *Reviews of Modern Physics*, 28(4):432–542, 1956. ISSN 00346861. doi: 10.1103/RevModPhys.28.432.
- [16] K. Alder and A. Winther. *Electromagnetic excitation: Theory of Coulomb excitation with heavy ions*. North-Holland, 1975. ISBN 0-7204-0288-3.
- [17] C. A. Bertulani. Theory and Applications of Coulomb Excitation. 2009. URL <http://arxiv.org/abs/0908.4307>.
- [18] R. Bass. *Nuclear Reactions with Heavy Ions*. Springer-Verlag Berlin Heidelberg, 1st edition, 1980. ISBN 3-540-09611-6.
- [19] D. Cline, H. S. Gertzman, H. E. Gove, P. M. S. Lesser, and J. J. Schwartz. The static quadrupole moment of the first excited state of  $^{60}\text{Ni}$ . *Nuclear Physics A*, 133(2):445–464, 1969. doi: [https://doi.org/10.1016/0375-9474\(69\)90646-0](https://doi.org/10.1016/0375-9474(69)90646-0). URL <http://www.sciencedirect.com/science/article/pii/0375947469906460>.
- [20] O. T. Niedermaier. Low-Energy Coulomb Excitation of the Neutron-Rich Mg Isotopes  $^{30}\text{Mg}$  and  $^{32}\text{Mg}$ , July 2005. doi: 10.11588/heidok.00005647.
- [21] J.-V. Kratz and K. H. Lieser. *Nuclear and Radiochemistry: Fundamentals and Applications*. Wiley-VCH Verlag GmbH & Co. KGaA, 3rd revised edition, 2013. ISBN 9783527653331.
- [22] D. Cline. Nuclear Shapes Studied by Coulomb Excitation. *Annual Review of Nuclear and Particle Science*, 36(1):683–716, 1986. ISSN 00664243. doi: 10.1146/annurev.nucl.36.1.683.

- [23] J. S. Al-Khalili and E. Roeckl. *The Euroschool Lectures on Physics with Exotic Beams, Vol. II.* Springer Berlin Heidelberg, 2006. ISBN 978-3-540-33786-7. doi: 10.1007/b11743651.
- [24] K. LÖBNER, M. VETTER, and V. HÖNIG. Nuclear Intrinsic Quadrupole Moments and Deformation Parameters. *Atomic Data and Nuclear Data Tables*, 7(5):495–564, 1970. ISSN 0092640X. doi: 10.1016/s0092-640x(18)30059-7.
- [25] M. J. Borge and K. Riisager. HIE-ISOLDE, the project and the physics opportunities. *European Physical Journal A*, 52(11), 2016. ISSN 1434601X. doi: 10.1140/epja/i2016-16334-4.
- [26] The ISOLDE web page. URL <http://isolde.web.cern.ch>. Accessed: July 2019.
- [27] B. Jonson and K. Riisager. The ISOLDE facility. *Scholarpedia*, 5(7):9742, 2010. doi: 10.4249/scholarpedia.9742. Revision #90796.
- [28] H. Jarlett. HIE-ISOLDE: Nuclear physics gets further energy boost. URL <https://home.cern/news/news/experiments/hie-isolde-nuclear-physics-gets-further-energy-boost>. Accessed: August 2019.
- [29] C. Lefèvre. The CERN accelerator complex. Complexe des accélérateurs du CERN. Dec 2008. URL <https://cds.cern.ch/record/1260465>.
- [30] Nucleonica Newsletter, 2019. URL <https://www.nucleonica.com/wiki/images/c/cb/NucleonicaNewsletter2019.pdf>. Accessed: July 2019.
- [31] M. Lindroos. Review of the ISOL Method. Technical Report CERN-AB-2004-086, CERN, Geneva, Aug 2004. URL <https://cds.cern.ch/record/793447>. Revised version submitted on 2004-09-28 17:19:32.
- [32] D. Olsen. First generation ISOL radioactive ion beam facilities. pages 312–316, 2002. doi: 10.1109/pac.1995.504646.
- [33] N. Warr, J. Van de Walle, M. Albers, et al. The miniball spectrometer. *European Physical Journal A*, 49(3):1–32, 2013. ISSN 1434601X. doi: 10.1140/epja/i2013-13040-9.
- [34] R. Catherall, W. Andreazza, M. Breitenfeldt, et al. The ISOLDE facility. 2, 2017. ISSN 13616471. doi: 10.1088/1361-6471/aa7eba.
- [35] M. J. Borge. The ISOLDE facility: Recent highlights and the HIE-ISOLDE project. *Proceedings of Science*, 11005:1–8, 2013. ISSN 18248039.

- [36] The ISOLDE RILIS web page. URL <http://rilis.web.cern.ch>. Accessed: July 2019.
- [37] B. A. Marsh, B. Andel, A. N. Andreyev, et al. New developments of the in-source spectroscopy method at RILIS/ISOLDE. *Nuclear Instruments and Methods in Physics Research, Section B: Beam Interactions with Materials and Atoms*, 317(PART B):550–556, 2013. ISSN 0168583X. doi: 10.1016/j.nimb.2013.07.070. URL <http://dx.doi.org/10.1016/j.nimb.2013.07.070>.
- [38] V. Fedosseev, K. Chrysalidis, T. D. Goodacre, et al. Ion beam production and study of radioactive isotopes with the laser ion source at ISOLDE. *Journal of Physics G: Nuclear and Particle Physics*, 44(8):084006, 2017. ISSN 0954-3899. doi: 10.1088/1361-6471/aa78e0.
- [39] E. Kugler, D. Fiander, B. Johnson, et al. The new CERN-ISOLDE on-line mass-separator facility at the PS-Booster. *Nuclear Inst. and Methods in Physics Research, B*, 70(1-4):41–49, 1992. ISSN 0168583X. doi: 10.1016/0168-583X(92)95907-9.
- [40] P. Schmidt, F. Ames, G. Bollen, et al. Bunching and cooling of radioactive ions with REXTRAP. *Nuclear Physics A*, 701(1-4):550–556, 2002. ISSN 03759474. doi: 10.1016/S0375-9474(01)01642-6.
- [41] F. Ames, G. Bollen, P. Delahaye, et al. Cooling of radioactive ions with the Penning trap REXTRAP. *Nuclear Instruments and Methods in Physics Research, Section A: Accelerators, Spectrometers, Detectors and Associated Equipment*, 538(1-3):17–32, 2005. ISSN 01689002. doi: 10.1016/j.nima.2004.08.119.
- [42] B. H. Wolf, J. Cederkäll, O. Forstner, et al. First radioactive ions charge bred in REXEBIS at the REX-ISOLDE accelerator. *Nuclear Instruments and Methods in Physics Research, Section B: Beam Interactions with Materials and Atoms*, 204:428–432, 2003. ISSN 0168583X. doi: 10.1016/S0168-583X(02)02108-0.
- [43] Y. Kadi, Y. Blumenfeld, W. V. Delsolaro, et al. Post-accelerated beams at ISOLDE. *Journal of Physics G: Nuclear and Particle Physics*, 44(8), 2017. ISSN 13616471. doi: 10.1088/1361-6471/aa78ca.
- [44] The REX-ISOLDE web page. URL <http://rex-isolde.web.cern.ch>. Accessed: July 2019.
- [45] The HIE-ISOLDE web page. URL <http://hie-isolde-project.web.cern.ch>. Accessed: July 2019.

- [46] F. Wenander. EBIS as charge breeder for radioactive ion beam accelerators. *Nuclear Physics A*, 701(1-4):528–536, 2002. ISSN 03759474. doi: 10.1016/S0375-9474(01)01640-2.
- [47] F. Wenander. Charge breeding of radioactive ions with EBIS and EBIT. *Journal of Instrumentation*, 5(10), 2010. ISSN 17480221. doi: 10.1088/1748-0221/5/10/C10004.
- [48] N. Warr. *The Miniball double-sided silicon strip detector (CD)*, October 2015. URL <https://www.ikp.uni-koeln.de/~warr/doc/cd.pdf>. Accessed: April 2019.
- [49] A. N. Ostrowski, S. Cherubini, T. Davinson, et al. CD: A double sided silicon strip detector for radioactive nuclear beam experiments. *Nuclear Instruments and Methods in Physics Research, Section A: Accelerators, Spectrometers, Detectors and Associated Equipment*, 480(2-3):448–455, 2002. ISSN 01689002. doi: 10.1016/S0168-9002(01)00954-8.
- [50] O. B. Tarasov and D. Bazin. LISE++: Radioactive beam production with in-flight separators. *Nuclear Instruments and Methods in Physics Research Section B: Beam Interactions with Materials and Atoms*, 266(19):4657 – 4664, 2008. ISSN 0168-583X. doi: <https://doi.org/10.1016/j.nimb.2008.05.110>. URL <http://lise.nscl.msu.edu/lise.html>. Proceedings of the XVth International Conference on Electromagnetic Isotope Separators and Techniques Related to their Applications.
- [51] N. Warr. *The Miniball Cluster*, March 2005. URL [https://www.ikp.uni-koeln.de/~warr/doc/miniball\\_detectors.pdf](https://www.ikp.uni-koeln.de/~warr/doc/miniball_detectors.pdf). Accessed: July 2019.
- [52] P. A. Butler, J. Cederkall, and P. Reiter. Nuclear-structure studies of exotic nuclei with MINIBALL. *Journal of Physics G: Nuclear and Particle Physics*, 44(4), 2017. ISSN 1361-6471. doi: 10.1088/1361-6471/aa5c4e.
- [53] D. P. Rosiak. *Coulomb excitation of doubly-magic  $^{132}\text{Sn}$  at HIE-ISOLDE and development of escape-suppression shields for the MINIBALL spectrometer*. PhD thesis, University of Cologne, 2018. URL <https://kups.ub.uni-koeln.de/8469/>.
- [54] N. Warr. *Miniball Flexible Frame*, March 2015. URL <https://www.ikp.uni-koeln.de/~warr/doc/frame.pdf>. Accessed: July 2019.
- [55] R. Lutter, O. Schaile, K. Schöffel, et al. MARaBOOU-A MBS and ROOT based online/offline utility. *SANTA FE 1999 - 11th IEEE NPSS Real Time Conference, Conference Record, RT 1999*, (May):363–366, 1999. doi: 10.1109/RTCON.1999.842643.

- [56] MARaBOOU Data acquisition web page. URL <https://www-old.mll-muenchen.de/marabou/html/doc/>. Accessed: July 2019.
- [57] H. G. Essel and N. Kurz. The general purpose data acquisition system MBS. *SANTA FE 1999 - 11th IEEE NPSS Real Time Conference, Conference Record, RT 1999*, 41(2):475–478, 1999. doi: 10.1109/RTCON.1999.842672.
- [58] R. Brun and F. Rademakers. ROOT - An Object Oriented Data Analysis Framework. Proceedings AIHENP'96 Workshop, Lausanne, Sep. 1996, Nucl. Inst. & Meth. in Phys. Res. A 389 (1997) 81-86. URL <https://github.com/root-project/root>. doi: 10.5281/zenodo.2557526. Download: December 2018.
- [59] N. Warr. *Miniball electronics for 2015*, October 2015. URL [https://www.ikp.uni-koeln.de/~warr/doc/electronics\\_201507.pdf](https://www.ikp.uni-koeln.de/~warr/doc/electronics_201507.pdf). Accessed: August 2019.
- [60] L. P. Gaffney. Octupole collectivity in  $^{220}\text{Rn}$  and  $^{224}\text{Ra}$ , Sep 2012. URL <https://cds.cern.ch/record/1547569>. Presented 18 Dec 2012.
- [61] HIE-ISOLDE: Technical Design Report for the Energy Upgrade, edited by Y. Kadi, M. A. Fraser and A. Papageorgiou-Koufidou, CERN Yellow Reports: Monographs, Vol. 1/2018, CERN-2018-002-M (CERN, Geneva, 2018). <https://doi.org/10.23731/CYRM-2018-001>.
- [62] Analysis code for MINIBALL experiments at ISOLDE. URL <https://github.com/Miniball/MiniballCoulexSort>. doi: 10.5281/zenodo.2593370. Download: March 2019.
- [63] W. R. Leo. *Techniques for Nuclear and Particle Physics Experiments*. Springer, Berlin, Heidelberg, second revised edition, 1994. doi: 10.1007/978-3-642-57920-2.
- [64] L. P. Gaffney. Kinematics simulations for Coulomb-excitation experiments at Miniball. URL <https://github.com/lpgaff/kinsim>. Download: May 2018.
- [65] J. F. Ziegler, J. P. Biersack, and M. D. Ziegler. SRIM - The Stopping and Range of Ions in Matter, 2013. URL <http://www.srim.org>. Download: February 2018.
- [66] Numpy and Scipy Documentation. URL <https://docs.scipy.org/doc/numpy/reference/generated/numpy.polyfit.html>. Accessed: July 2019.
- [67] B. Bruyneel, P. Reiter, and G. Pascovici. Characterization of large volume HPGe detectors. Part I: Electron and hole mobility parameterization. *Nuclear Instruments and Methods in Physics Research, Section A: Accelerators, Spectrometers, Detectors and Associated Equipment*, 569(3):764–773, 2006. ISSN 01689002. doi: 10.1016/j.nima.2006.08.130.

- [68] B. Bruyneel, P. Reiter, and G. Pascovici. Characterization of large volume HPGe detectors. Part II: Experimental results. *Nuclear Instruments and Methods in Physics Research, Section A: Accelerators, Spectrometers, Detectors and Associated Equipment*, 569(3):774–789, 2006. ISSN 01689002. doi: 10.1016/j.nima.2006.08.129.
- [69] B. Bruyneel. *Characterization of Segmented Large Volume, High Purity Germanium Detectors*. PhD thesis, University of Cologne, 2006. URL <https://kups.ub.uni-koeln.de/1858/>.
- [70] M. Descovich, I. Y. Lee, P. N. Luke, et al. Effects of neutron damage on the performance of large volume segmented germanium detectors. *Nuclear Instruments and Methods in Physics Research, Section A: Accelerators, Spectrometers, Detectors and Associated Equipment*, 545(1-2):199–209, 2005. ISSN 01689002. doi: 10.1016/j.nima.2005.01.308.
- [71] I. Abt, L. Garbini, C. Gooch, et al. Alpha-event and surface characterisation in segmented true-coaxial HPGe detectors. *Nuclear Instruments and Methods in Physics Research, Section A: Accelerators, Spectrometers, Detectors and Associated Equipment*, 858(June 2017):80–89, 2017. ISSN 01689002. doi: 10.1016/j.nima.2017.03.057. URL <http://dx.doi.org/10.1016/j.nima.2017.03.057>.
- [72] G. L. Miller, W. M. Gibson, and P. F. Donovan. Semiconductor Particle Detectors. *Annual Review of Nuclear Science*, 12(1):189–220, 1962. ISSN 0066-4243. doi: 10.1146/annurev.ns.12.120162.001201.
- [73] B. Wilkins, M. Fluss, S. Kaufman, C. Gross, and E. Steinberg. Pulse-height defects for heavy ions in a silicon surface-barrier detector. *Nuclear Instruments and Methods*, 92:381–391, 1971. doi: [https://doi.org/10.1016/0029-554X\(71\)90414-9](https://doi.org/10.1016/0029-554X(71)90414-9).
- [74] L. Grassi, J. Forneris, D. Torresi, et al. Study of the inter-strip gap effects on the response of Double Sided Silicon Strip Detectors using proton micro-beams. *Nuclear Instruments and Methods in Physics Research, Section A: Accelerators, Spectrometers, Detectors and Associated Equipment*, 767:99–111, 2014. ISSN 01689002. doi: 10.1016/j.nima.2014.08.009.
- [75] G. Kramberger, V. Cindro, I. Mandi, M. Mikuž, and M. Zavrtanik. Effective trapping time of electrons and holes in different silicon materials irradiated with neutrons, protons and pions. *Nuclear Instruments and Methods in Physics Research, Section A: Accelerators, Spectrometers, Detectors and Associated Equipment*, 481(1-3):297–305, 2002. ISSN 01689002. doi: 10.1016/S0168-9002(01)01263-3.

- [76] P. Doornenbal. In-beam gamma-ray spectroscopy at the RIBF. *Progress of Theoretical and Experimental Physics*, 2012(1):1–18, 2012. ISSN 20503911. doi: 10.1093/ptep/pts076.
- [77] R. Firestone, J. Gilat, J. Nitschke, P. A. Wilmarth, and K. Vierinen. Decay studies of neutron deficient nuclei near the  $Z = 64$  subshell:  $^{142}\text{Dy}$ ,  $^{140,142}\text{Tb}$ ,  $^{140,142}\text{Gd}$ ,  $^{140,142}\text{Eu}$ ,  $^{142}\text{Sm}$ , and  $^{142}\text{Pm}$ . *Physical Review C*, 43(3):1066–1085, 1991.
- [78] M. Klintefjord, K. Hadyńska-Klęk, J. Samorajczyk, et al. Spectroscopy of low-lying states in  $^{140}\text{Sm}$ . *Acta Physica Polonica B*, 46(3):607–611, 2015. ISSN 0587-4254. doi: 10.5506/APhysPolB.46.607.
- [79] J. Samorajczyk, M. Klintefjord, C. Droste, et al. Revised spin values of the 991 keV and 1599 keV levels in  $^{140}\text{Sm}$ . *Physical Review C - Nuclear Physics*, 92(4):3–6, 2015. ISSN 1089490X. doi: 10.1103/PhysRevC.92.044322.
- [80] N. Nica. Adopted levels, gammas for  $^{140}\text{Sm}$ . *Nuclear Data Sheets*, 154, 2018. URL <https://www.nndc.bnl.gov/nudat2/getdataset.jsp?nucleus=140SM&unc=nds>. Cutoff date: 20-Nov-2018. Accessed: August 2019.
- [81] M. Klintefjord, K. Hadyńska-Klęk, A. Görgen, et al. Structure of low-lying states in  $^{140}\text{Sm}$  studied by Coulomb excitation. *Physical Review C*, 93(5):1–14, 2016. ISSN 24699993. doi: 10.1103/PhysRevC.93.054303.
- [82] F. L. Bello Garrote, A. Görgen, J. Mierzejewski, et al. Lifetime measurement for the  $2_1^+$  state in  $^{140}\text{Sm}$  and the onset of collectivity in neutron-deficient Sm isotopes. *Physical Review C - Nuclear Physics*, 92(2):1–8, 2015. ISSN 1089490X. doi: 10.1103/PhysRevC.92.024317.
- [83] R. Brun and F. Rademakers. ROOT - User's Guide, 2018. URL <https://root.cern.ch/root/html/doc/guides/users-guide/ROOTUsersGuide.html#file-system.rootrc>. Accessed: August 2019.